Applied Superconductivity:

Josephson Effect and Superconducting Electronics

Manuscript to the Lectures during WS 2003/2004, WS 2005/2006, WS 2006/2007, WS 2007/2008, WS 2008/2009, and WS 2009/2010

Prof. Dr. Rudolf Gross

and

Dr. Achim Marx

Walther-Meißner-Institut
Bayerische Akademie der Wissenschaften
and
Lehrstuhl für Technische Physik (E23)
Technische Universität München

Walther-Meißner-Strasse 8
D-85748 Garching
Rudolf.Gross@wmi.badw.de

Contents

List of Figures

List of Tables

Part II

Applications of the Josephson Effect

Since the prediction of the Josephson effect and the first experimental realization of pair tunneling in superconductor/insulator/superconductor (SIS) systems, the technology of superconducting electronics has made tremendous progress. Superconducting electronics based on the Josephson effect covers a large number of both analog and digital applications. The properties of Josephson tunnel junctions and their typical current-voltage characteristics (IVC) immediately suggest the following applications:

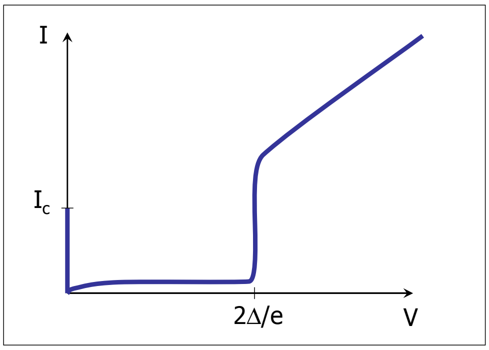

1. The maximum Josephson current depends on externally applied magnetic fields (see chapter 2), i.e. $I_s^m = I_s^m(B)$. The magnetic field dependence $I_s^m(B)$ is used in magnetic field sensors based on Superconducting Quantum Interference Devices (SQUIDs) as discussed in detail in chapter 4.

2. In an underdamped Josephson tunnel junction with $\beta_C \gg 1$ there is a bistable voltage state for $I < I_s^m$, namely the superconducting or ***zero voltage state*** and the ***voltage state*** with $V \sim V_g$. This bistability can be exploited in fast switching devices usable for digital circuits in Josephson computers (see chapter 5). The energy dissipation per switching process is expected to be very low.

3. The nonlinear dependence of the supercurrent on the phase difference across a Josephson junction leads to structures in the IVC with an applied ac-source (eg. Shapiro steps). The relation between the ac frequency and the voltage/current steps can be utilized in voltage controlled oscillators (VCO) and in defining a voltage standard (see chapter 6).

4. The nonlinear IVC can be used in different kinds of mixers (Josephson- and QP-mixer) for frequencies up to several THz. Furthermore, the coupling of the oscillating Josephson current to resonant modes of the junction can be exploited in microwave oscillators (see chapter 7).

5. The macroscopic quantum behavior of Josephson junction circuits allows to use single Josephson junctions and loops containing one or more Josephson junctions as effective quantum two-level systems for the realization of superconducting quantum bits (see chapter 9).

The most important applications of Josephson junctions in analog and digital devices and circuits are discussed in the following chapters.

Chapter 4

Superconducting Quantum Interference Devices

The discussion of the magnetic field dependence of the maximum Josephson current I_s^m as a function of the applied magnetic field in Chapter 2 already showed that there is a strong modulation of I_s^m with the applied field. Therefore, in principle a simple Josephson junction already can be used as a magnetic field sensor. However, for practical applications the sensitivity of such a device is not high enough to compete with other techniques. The magnetic field dependence of the maximum Josephson current was found to have the shape of the diffraction pattern of a slit. The first minimum of the diffraction pattern is obtained, when the applied field generates one flux quantum in the junction area. Therefore, the sensitivity of the device is roughly $I_s^m/\Phi_0 = I_s^m/B_0 t_B L$, where $t_B L$ is the junction area threaded by the magnetic field. We immediately see, that we should increase the area $t_B L$ in order to increase the sensitivity. Then, one flux quantum is generated already at a much smaller applied magnetic field.

The easiest way to increase the area threaded by the magnetic field is to use not only a single Josephson junction but a superconducting loop or cylinder containing one or more Josephson junctions. We will see that in this case the relevant area is determined by the cross-sectional area of the ring or cylinder and not the junction area. Devices consisting of a superconducting loop interrupted by one or more Josephson junctions are denoted as ***Superconducting Quantum Interference Devices*** (SQUIDs). Hence, SQUIDs combine two physical phenomena, namely ***flux quantization in superconducting loops*** and the ***Josephson effect***. Today SQUIDs are the most sensitive detectors for magnetic flux available. In essence, a SQUID is a flux to voltage converter providing a flux dependent output voltage with a period of one flux quantum. We will see that SQUIDs are very versatile. They can measure all physical quantities that can be converted into magnetic flux, for example magnetic field, magnetic field gradients, current, voltage, displacement, or magnetic susceptibility.

In this chapter we will discuss the underlying physics, the performance limits and some practical applications of SQUIDs. In doing so we will focus on two kinds of SQUIDs. The first, the so-called ***direct current or dc-SQUID***,[1] consists of two junctions connected in parallel on a superconducting loop. It is named dc-SQUID, since it operates with a steady bias current. The second, ***radio frequency or rf-SQUID***,[2,3] consists of a superconducting loop interrupted by a single junction. It operates with a radio-frequency flux bias. Historically, the dc-SQUID was used for magnetic measurements just after

[1] R.C. Jaklevic, J. Lambe, A.H. Silver, J.E. Mercereau, *Quantum Interference Effects in Josephson Tunneling*, Phys. Rev. Lett. **12**, 159 (1964).

[2] J.E. Zimmermann, P. Thiene, J.T. Harding, *Design and Operation of Stable rf-biased Superconducting Point-contact Quantum Devices*, J. Appl. Phys. **41**, 1572 (1970).

[3] J.E. Mercereau, *Superconducting Magnetometers*, Rev. Phys. Appl. **5**, 13 (1970).

the first observation of macroscopic quantum interference in superconductivity.[4,5] However, later in the late 1960s and early 1970s the rf-SQUID was preferred, mainly since it was easier to fabricate single junction interferometers using a simple point-contact. However, then in 1975 **J. Clarke** and co-workers showed that the energy sensitivity of dc-SQUIDs can be improved by using externally shunted junctions to values better than those of the rf-SQUID.[6] This made the use of dc-SQUIDs preferable in applications requiring optimum resolution. Despite the improvement of rf-SQUIDs, their energy sensitivity is still worse than that of dc-SQUID at 4 K. However, at 77 K both types of SQUIDs are comparable making rf-SQUIDs again attractive for SQUIDs based on the high temperature superconductors.

[4] J. Clarke, Phil. Mag. **13**, 115 (1966).
[5] R.L. Forgacs, A. Warnick, Rev. Sci. Instr. **18**, 214 (1967).
[6] J. Clarke, W.M. Goubau, M.B. Ketchen, Appl. Phys. Lett. **27**, 155 (1976); J. Low Temp. Phys. **25**, 99 (1976).

4.1 The dc-SQUID

4.1.1 The Zero Voltage State

Two superconducting Josephson junctions can be combined in parallel as shown in Fig. 4.1 to obtain a superconducting quantum interference device known as the ***direct current superconducting quantum interference device***. The two superconducting junctions, which we will consider as lumped elements, are connected in parallel and joined by a superconducting loop. The two junctions are assumed to have identical critical current I_c so that they are characterized by the current-phase relations $I_{s1} = I_c \sin\varphi_1$ and $I_{s2} = I_c \sin\varphi_2$. Applying Kirchhoff's law we obtain for the total current[7]

$$\begin{aligned} I_s &= I_{s1} + I_{s2} = I_c \sin\varphi_1 + I_c \sin\varphi_2 \\ &= 2I_c \cos\left(\frac{\varphi_1 - \varphi_2}{2}\right) \sin\left(\frac{\varphi_1 + \varphi_2}{2}\right) . \end{aligned} \tag{4.1.1}$$

The gauge-invariant phase differences φ_1 and φ_2 can be found by considering the line integral along the contour shown in Fig. 4.1. We have to demand that the total phase change along the closed contour is $2\pi n$. Hence, in the same way as for the situation discussed in section 2.2.1 we obtain

$$\begin{aligned} \oint_C \nabla\theta \cdot d\mathbf{l} &= 2\pi\, n \\ &= (\theta_{Q_b} - \theta_{Q_a}) + (\theta_{P_c} - \theta_{Q_b}) + (\theta_{P_d} - \theta_{P_c}) + (\theta_{Q_a} - \theta_{P_d}) + 2\pi\, n \end{aligned} \tag{4.1.2}$$

Using $\nabla\theta = \frac{2\pi}{\Phi_0}(\Lambda\mathbf{J}_s + \mathbf{A})$ (compare (2.2.2)) and $\varphi = \theta_2 - \theta_1 - \frac{2\pi}{\Phi_0}\int_1^2 \mathbf{A}\cdot d\mathbf{l}$ (compare (2.2.3)) we obtain in analogy to section 2.2.1:

$$\theta_{Q_b} - \theta_{Q_a} = +\varphi_1 + \frac{2\pi}{\Phi_0}\int_{Q_a}^{Q_b} \mathbf{A}\cdot d\mathbf{l} \tag{4.1.3}$$

$$\theta_{P_d} - \theta_{P_c} = -\varphi_2 + \frac{2\pi}{\Phi_0}\int_{P_c}^{P_d} \mathbf{A}\cdot d\mathbf{l} \tag{4.1.4}$$

$$\theta_{P_c} - \theta_{Q_b} = \int_{Q_b}^{P_c} \nabla\theta \cdot d\ell = +\frac{2\pi}{\Phi_0}\int_{Q_b}^{P_c} \Lambda\mathbf{J}_s \cdot d\mathbf{l} + \frac{2\pi}{\Phi_0}\int_{Q_b}^{P_c} \mathbf{A}\cdot d\mathbf{l} \tag{4.1.5}$$

$$\theta_{Q_a} - \theta_{P_d} = \int_{P_d}^{Q_a} \nabla\theta \cdot d\ell = +\frac{2\pi}{\Phi_0}\int_{P_d}^{Q_a} \Lambda\mathbf{J}_s \cdot d\mathbf{l} + \frac{2\pi}{\Phi_0}\int_{P_d}^{Q_a} \mathbf{A}\cdot d\mathbf{l} . \tag{4.1.6}$$

Substitution of (4.1.3) – (4.1.6) into (4.1.2) yields

$$\varphi_1 - \varphi_2 = -\frac{2\pi}{\Phi_0}\oint_C \mathbf{A}\cdot d\ell - \frac{2\pi}{\Phi_0}\int_{Q_b}^{P_c} \Lambda\mathbf{J}_s \cdot d\ell - \frac{2\pi}{\Phi_0}\int_{P_d}^{Q_a} \Lambda\mathbf{J}_s \cdot d\ell . \tag{4.1.7}$$

[7] We use $\sin\alpha + \sin\beta = 2\sin\left(\frac{\alpha+\beta}{2}\right)\cos\left(\frac{\alpha-\beta}{2}\right)$.

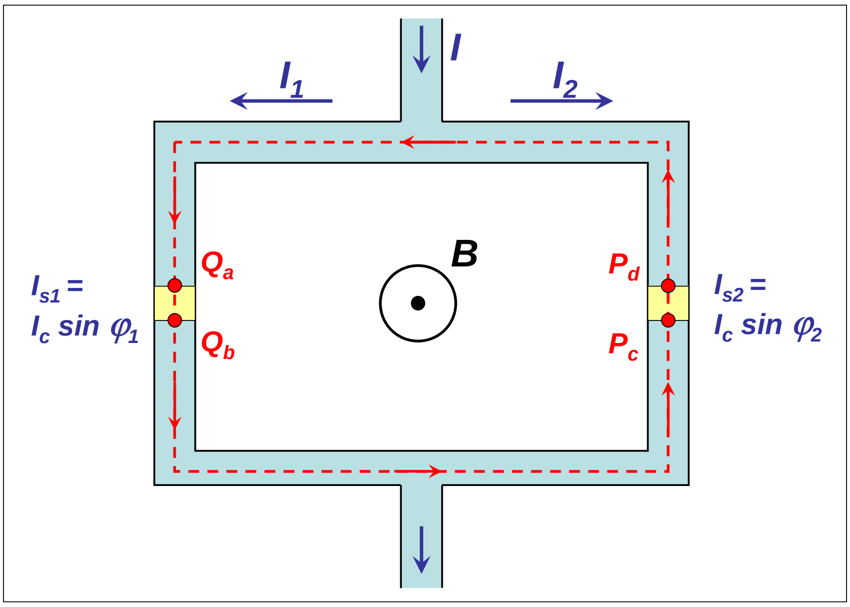

Figure 4.1: The dc-SQUID formed by two Josephson junctions intersecting a superconducting loop. The upper and the lower part of the loop can be represented by the macroscopic wave functions $\Psi_2 = \Psi_{20}\exp(\imath\theta_2)$ and $\Psi_1 = \Psi_{10}\exp(\imath\theta_1)$, respectively. The broken line indicates the closed contour path of the integration.

The integration of $\mathbf{A}$ is around a closed contour and therefore is equal to the total flux Φ enclosed by the superconducting loop. The integration of $\mathbf{J}_s$ follows the same contour C but excludes the integration over the insulating barrier. Furthermore, if the superconducting loop consists of a superconducting material with a thickness large compared to the London penetration depth λ_L, the integration path can be taken deep inside the superconducting material where the current density is negligible. Therefore, the two integrals involving the current density can be omitted and we obtain

$$\boxed{\varphi_2 - \varphi_1 \quad = \quad \frac{2\pi\Phi}{\Phi_0} \ .} \tag{4.1.8}$$

We see that the two phase differences across the junctions are not independent but are linked to each other via the boundary condition that we have to satisfy fluxoid quantization in the superconducting loop. Using expression (4.1.8) we can rewrite (4.1.1) as[8]

$$\boxed{I_s \quad = \quad 2I_c \cos\left(\pi\frac{\Phi}{\Phi_0}\right)\ \sin\left(\varphi_1 + \pi\frac{\Phi}{\Phi_0}\right) \ .} \tag{4.1.9}$$

If the flux Φ threading the loop would be given just by the flux $\Phi_{\rm ext}$ due to the externally applied magnetic field, we would have solved the problem. Then, the maximum supercurrent of the parallel combination is just given by

$$\boxed{I_s^m \quad = \quad 2I_c \left|\cos\left(\pi\frac{\Phi_{\rm ext}}{\Phi_0}\right)\right| \ .} \tag{4.1.10}$$

[8]Here, we use $(\varphi_1+\varphi_2)/2 = [2\varphi_1 + (\varphi_2-\varphi_1)]/2 = \varphi_1 + (\varphi_2-\varphi_1)/2$.

However, in many cases we have to take into account the finite inductance L of the superconducting loop. Then, the flux Φ threading the loop is given by the sum

$$\Phi = \Phi_{\rm ext} + \Phi_L \tag{4.1.11}$$

due to the applied magnetic field and the currents flowing in the loop. If we assume that the two sides of the loop are identical, we can write the currents flowing in the two arms of the loop as

$$I_{s1} = \widetilde{I} + I_{\rm cir} \tag{4.1.12}$$
$$I_{s2} = \widetilde{I} - I_{\rm cir} \ , \tag{4.1.13}$$

where

$$\widetilde{I} = \frac{I_{s1}+I_{s2}}{2} \qquad \text{and} \qquad I_{\rm cir} = \frac{I_{s1}-I_{s2}}{2} \tag{4.1.14}$$

are the average current common in both arms and the current circulating in the loop, respectively. Note that only the latter generates a net magnetic flux in the loop with the total flux then given by

$$\begin{aligned}\Phi &= \Phi_{\rm ext} + LI_{\rm cir} = \Phi_{\rm ext} + \frac{LI_c}{2}(\sin\varphi_1 - \sin\varphi_2) \\ &= \Phi_{\rm ext} + LI_c \sin\left(\frac{\varphi_1-\varphi_2}{2}\right)\cos\left(\frac{\varphi_1+\varphi_2}{2}\right) \ .\end{aligned} \tag{4.1.15}$$

Using (4.1.8), we can write the total flux threading the loop as a function of $\Phi_{\rm ext}$ and φ_1:[9]

$$\boxed{\Phi = \Phi_{\rm ext} - LI_c \sin\left(\pi\frac{\Phi}{\Phi_0}\right)\cos\left(\varphi_1 + \pi\frac{\Phi}{\Phi_0}\right) \ .} \tag{4.1.16}$$

We see that we have now two equations, (4.1.9) and (4.1.16), which determine the behavior of the dc-SQUID. These two equations have to be solved self-consistently. The maximum current I_s^m that can be sent through the SQUID at a given $\Phi_{\rm ext}$ has to be found by maximizing (4.1.9) with respect to φ_1, however, with the constraint given by (4.1.16). This problem has been solved first by **R. de Bruyn Ouboter** and **A.Th.A.M. de Waele**.[10]

In order to analyze limiting cases we introduce the so-called ***screening parameter*** β_L defined as

$$\beta_L \equiv \frac{2LI_c}{\Phi_0} \ . \tag{4.1.17}$$

This parameter represents the ratio of the magnetic flux generated by the maximum possible circulating current $I_{\rm cir} = I_c$ and $\Phi_0/2$. We also see that for $\beta_L = 1$ the coupling energy $2E_J = 2\hbar I_c/2e = \Phi_0 I_c/\pi$ of the two Josephson junctions is, apart from a factor $4/\pi$, equal to the magnetic energy $\Phi_0^2/8L$ due to the magnetic flux $\Phi_0/2$ stored in the superconducting loop.

[9]Here, we use $\sin(-\alpha) = -\sin\alpha$.

[10] R. de Bruyn Ouboter, A.Th.A.M. de Waele, *Superconducting Point Contacts Weakly Connecting Two Superconductors*, Progress in Low Temp. Phys. **VI**, C.J. Gorter ed., Elsevier Science Publishers (1970).

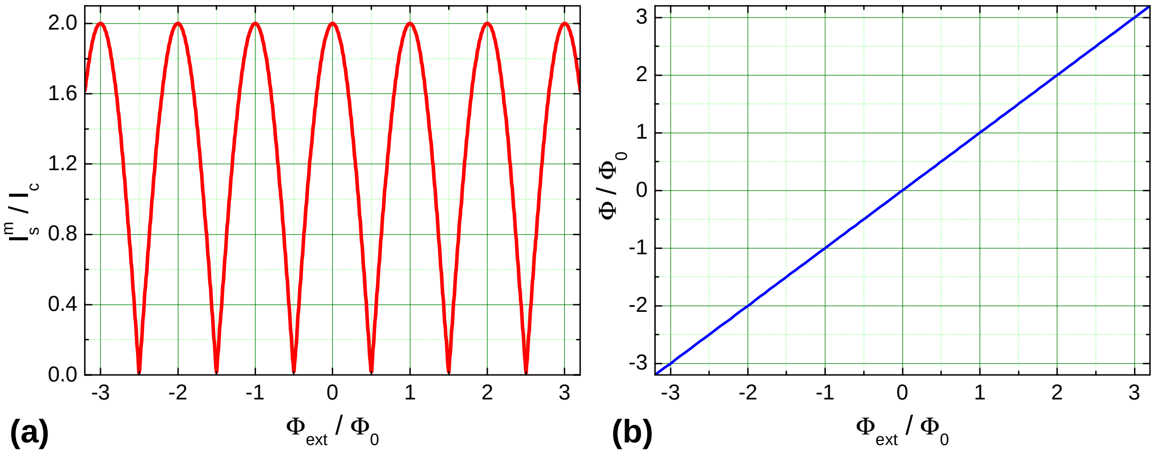

Figure 4.2: (a) The maximum supercurrent I_s^m plotted versus the applied magnetic flux $\Phi_{\rm ext}$ for a dc-SQUID with two identical Josephson junctions in the limit $\beta_L \ll 1$. In (b) the flux threading the SQUID loop is plotted versus the applied flux $\Phi_{\rm ext}$.

Negligible Screening: $\beta_L \ll 1$

In the case $\beta_L \ll 1$ the flux generated by the circulating current is small compared to the flux quantum and therefore can be neglected compared to $\Phi_{\rm ext}$. At a given $\Phi_{\rm ext}$ the maximum supercurrent of the dc-SQUID is found by maximizing (4.1.9) with respect to φ_1. From the condition $dI_s/d\varphi_1 = 0$ we obtain

$$\cos\left(\varphi_1 + \pi\frac{\Phi_{\rm ext}}{\Phi_0}\right) = 0 \ . \tag{4.1.18}$$

Thus, at the maximum we have $\sin\left(\varphi_1 + \pi\frac{\Phi_{\rm ext}}{\Phi_0}\right) = \pm 1$ and the maximum value of the supercurrent is found by taking the sign of the sine term. That is, we obtain the result

$$I_s^m \simeq 2I_c \left|\cos\left(\pi\frac{\Phi_{\rm ext}}{\Phi_0}\right)\right| \ , \tag{4.1.19}$$

which is of course equivalent to (4.1.10). As shown in Fig. 4.2, I_s^m is a periodic function of the external flux. Note that for a loop area of $2\,{\rm mm}^2$ an applied field of 1 nT results in $\Phi_{\rm ext} = \Phi_0$, that is, the periodicity of the curve corresponds to the very small field of 1 nT, which is more than four orders of magnitude smaller than the earth magnetic field.

Large Screening: $\beta_L \gg 1$

For large inductance L we have $LI_c \gg \Phi_0$ and the circulating current tends to compensate the applied flux. The loop of the SQUID looks more and more like the single loop formed by a superconducting wire. This situation was discussed already in section 1.2 when we discussed flux quantization in multiply connected superconductors. Consequently, the total flux in the loop will tend to be quantized:

$$\Phi = \Phi_{\rm ext} + LI_{\rm cir} \simeq n\Phi_0 \ . \tag{4.1.20}$$

Let us consider the case of large screening a bit more closely. The transport supercurrent through the SQUID is the sum of the currents passing junction 1 and 2:

$$I_s = I_c \sin\varphi_1 + I_c \sin\varphi_2 \ . \tag{4.1.21}$$

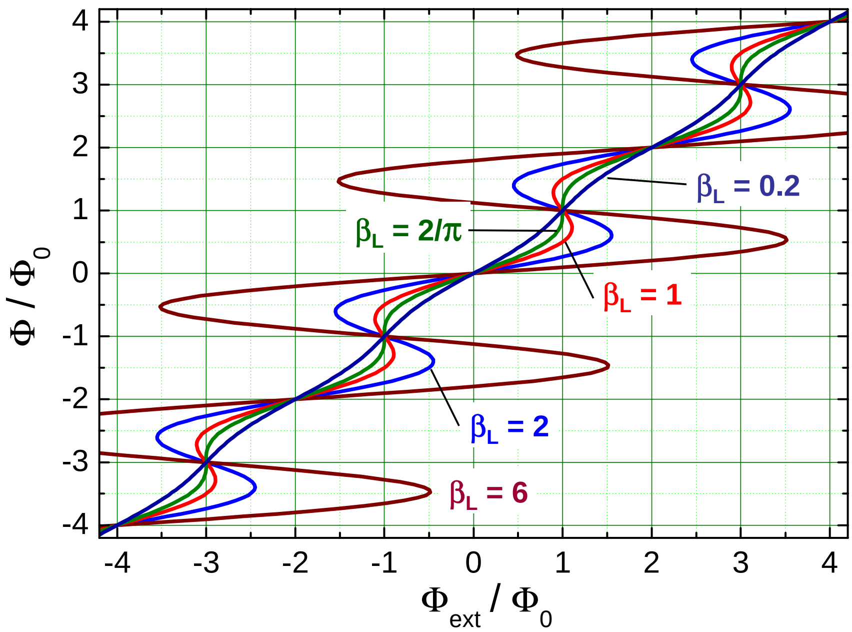

Figure 4.3: The total magnetic flux Φ plotted versus the applied magnetic flux $\Phi_{\rm ext}$ for a dc-SQUID with two identical Josephson junctions for different values of the screening parameter β_L.

On the other hand, the circulating screening current is given by

$$I_{\rm cir} = \frac{I_c}{2}(\sin\varphi_1 - \sin\varphi_2) \ . \qquad (4.1.22)$$

Both (4.1.21) and (4.1.22) are constraint by the condition

$$\varphi_2 - \varphi_1 = \frac{2\pi\Phi}{\Phi_0} \ . \qquad (4.1.23)$$

Note that here the magnetic flux is the sum of the external flux $\Phi_{\rm ext}$ and the flux $\Phi_{\rm cir} = LI_{\rm cir}$ due to the screening current. Given the applied current I and the total flux Φ we have two equations for the two phase differences $\varphi_{1,2}$ and hence can solve for them and finally for $\Phi_{\rm cir}$ and $\Phi_{\rm ext}$. For example, if $I \simeq 0$, we have $\sin\varphi_1 \simeq -\sin\varphi_2$ and obtain

$$\begin{aligned} \Phi_{\rm ext} &= \Phi + LI_c \sin\left(\pi\frac{\Phi}{\Phi_0}\right) \qquad \text{or} \\ \frac{\Phi_{\rm ext}}{\Phi_0} &= \frac{\Phi}{\Phi_0} + \frac{\beta_L}{2}\sin\left(\pi\frac{\Phi}{\Phi_0}\right) \ . \end{aligned} \qquad (4.1.24)$$

This relationship of course can be inverted to obtain Φ as a function of $\Phi_{\rm ext}$ as shown in Fig. 4.3.

An interesting case occurs for $\Phi = n\Phi_0$, for which $\varphi_1 = \varphi_2 + n2\pi$, so that $I_{\rm cir} = 0$ and $\Phi = \Phi_{\rm ext}$. We see that the SQUID response to $\Phi_{\rm ext}$ in integer multiples of Φ_0 is not affected by the screening. However, for practical applications it is often required that the relation between Φ and $\Phi_{\rm ext}$ is single-valued and non-hysteretic. As shown by Fig. 4.3 this is possible only for small values of the screening parameter β_L. This results from the fact that the maximum possible value of $\Phi_{\rm cir}$ is LI_c. Since roughly speaking a multivalued relationship between Φ and $\Phi_{\rm ext}$ can be avoided only for $|\Phi_{\rm cir}| \leq \Phi_0/2$, we immediately see that this is equivalent to $LI_c \leq \Phi_0/2$ or $\beta_L = 2LI_c/\Phi_0 \leq 1$. A more detailed analysis shows that a hysteretic $\Phi(\Phi_{\rm ext})$ dependence can be avoided for $\beta_L \leq 2/\pi$.

We still have to discuss the dependence of the supercurrent on the applied magnetic flux. From (4.1.20) we obtain for large β_L

$$I_{\rm cir} \simeq -\frac{\Phi_{\rm ext} - n\Phi_0}{L} \ . \tag{4.1.25}$$

We see that $I_{\rm cir} \to 0$ for large L. Then, the applied current divides about equally in the two SQUID arms. The maximum current is obtained to $I_s^m \simeq 2I_c$. When n is initially zero, a small screening current $I_{\rm cir} \simeq -\Phi_{\rm ext}/L$ will flow to screen the applied magnetic field. Therefore, the current I_1 will tend to decrease and I_2 to increase with increasing $\Phi_{\rm ext}$. However, since $I_2 \leq I_c$, it will be fixed at I_c as I_1 decreases as

$$I_1 \simeq I_c - \frac{2\Phi_{\rm ext}}{L} \ . \tag{4.1.26}$$

With this expression for I_1 and $I_2 \simeq const \simeq I_c$ we obtain

$$I_s^m \simeq 2I_c - \frac{2\Phi_{\rm ext}}{L} \qquad \text{or} \tag{4.1.27}$$

$$\frac{I_s^m}{2I_c} \simeq 1 - \frac{2\Phi_{\rm ext}}{\Phi_0}\frac{1}{\beta_L} \ . \tag{4.1.28}$$

We see that the modulation of the maximum supercurrent of the SQUID by the applied magnetic flux is strongly decreasing with increasing β_L roughly proportional to $1/\beta_L$.

4.1.2 The Voltage State

Practical dc-SQUIDs are not operated in the zero voltage state. They are operated at a constant bias current above the maximum supercurrent $I_s^m(0)$ at zero applied magnetic flux. That is, the SQUID is in the voltage state. We will show that in this situation the dc-SQUID produces an output voltage that is related to the applied magnetic flux.

Negligible screening: $\beta_L \ll 1$, strong damping: $\beta_C \ll 1$

In order to discuss the dependence of the SQUID voltage on the applied magnetic flux we start with the limit of negligible screening. In this case the total flux in the SQUID loop is just given by the applied flux. We further assume that the junction capacitance is negligible small, that is, we consider the case of strongly overdamped Josephson junctions ($\beta_C \ll 1$) and that the two junctions are identical. Then, we only have to consider the Josephson current and the resistive current giving

$$\begin{aligned} I &= I_c \sin\varphi_1 + I_c \sin\varphi_2 + \frac{V}{R_N} + \frac{V}{R_N} \\ &= 2I_c \cos\left(\pi\frac{\Phi}{\Phi_0}\right) \sin\left(\varphi_1 + \pi\frac{\Phi}{\Phi_0}\right) + 2\,\frac{V}{R_N} \ . \end{aligned} \tag{4.1.29}$$

Here, we have used (4.1.1) and (4.1.8). Let us define the new phase

$$\varphi = \varphi_1 + \pi\,\frac{\Phi}{\Phi_0} \tag{4.1.30}$$

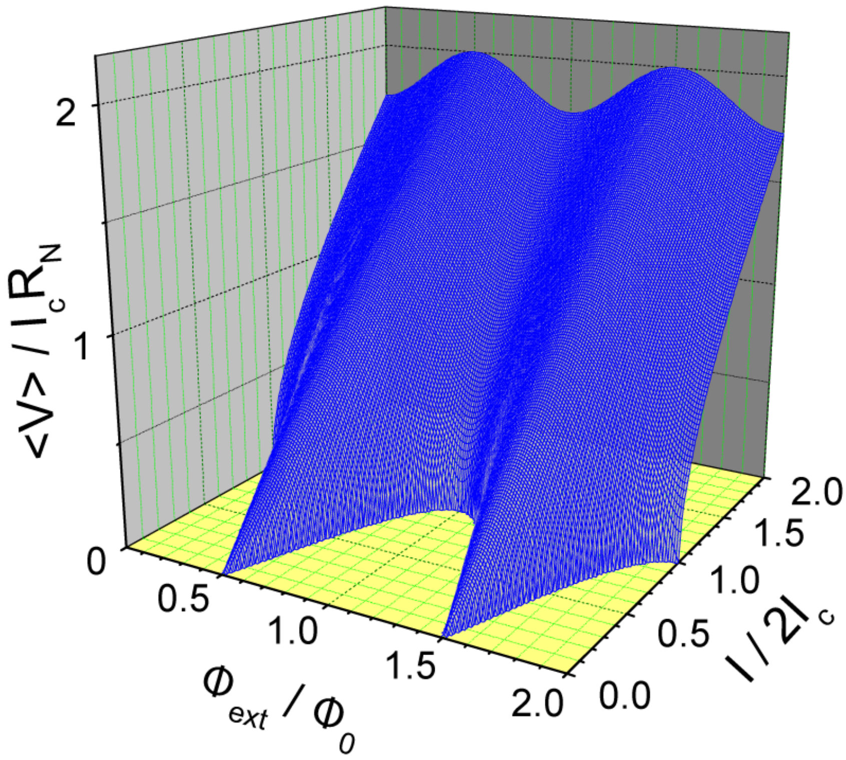

Figure 4.4: Current-voltage characteristics of a dc-SQUID in the limit $\beta_L \ll 1$, $\beta_C \ll 1$ for different values of the applied magnetic flux $\Phi_{\rm ext}$ for a dc-SQUID with two identical Josephson junctions.

and note that due $\Phi \simeq \Phi_{\rm ext} = const$ we have

$$\frac{d\varphi}{dt} = \frac{d\varphi_1}{dt} = \frac{2\pi}{\Phi_0} V(t) \ . \tag{4.1.31}$$

Then, we can rewrite (4.1.29) as

$$I = I_s^m(\Phi_{\rm ext}) \sin\varphi + \frac{2}{R_N} \frac{2\pi}{\Phi_0} \frac{d\varphi}{dt} \tag{4.1.32}$$

with

$$I_s^m(\Phi_{\rm ext}) = 2I_c \cos\left(\pi \frac{\Phi_{\rm ext}}{\Phi_0}\right) \ . \tag{4.1.33}$$

We see, that equation (4.1.32) represents the equation of a single Josephson junction with a maximum Josephson current that depends on the external flux. For a single junction we have used the pendulum as a mechanical analog. In the same way we can use two pendula that are coupled to each other as the analogue for the dc-SQUID. In the case of negligible screening ($\beta_L \ll 1$) the coupling of the two pendula is rigid as can be seen from (4.1.30) and they move with the same angular velocity according to (4.1.31). Note that the rigid coupling is no longer true for significant screening ($\beta_L \geq 1$).

Due to the equivalence of the dc-SQUID with a single junction having a flux dependent maximum Josephson current, the current-voltage characteristic of the dc-SQUID is just given by the RSJ-model result (3.3.8):

$$\boxed{\langle V(t)\rangle \;=\; I_cR_N\sqrt{\left(\frac{I}{2I_c}\right)^2-\left(\frac{I_s^m(\Phi_{\rm ext})}{2I_c}\right)^2} = I_cR_N\sqrt{\left(\frac{I}{2I_c}\right)^2-\left[\cos\left(\pi\frac{\Phi_{\rm ext}}{\Phi_0}\right)\right]^2}\ .} \qquad (4.1.34)$$

The IVCs obtained according to this equation are shown in Fig. 4.4. It can be seen that the IVCs are periodic with the applied magnetic flux with the periodicity of a single flux quantum. Considering the time-averaged junction voltage as a function of the applied flux for different values of the bias current we see that these curves are also periodic with the same periodicity. Furthermore, the minima and maxima of the $\langle V\rangle(\Phi_{\rm ext})$ always appear at the same flux values. Fig. 4.4 also shows the $\cos\pi\Phi_{\rm ext}/\Phi_0$ dependence of the zero voltage supercurrent through the SQUID. Furthermore, it is seen that the maximum modulation of the time-averaged voltage with varying applied flux occurs for $I \simeq 2I_c$.

Finite screening: $\beta_L \sim 1$, intermediate damping: $\beta_C \sim 1$

For practical SQUIDs the inductance L of the loop containing the Josephson junctions must be taken into account. As already discussed above, the loop area should be made large in order to increase the flux threading the SQUID at a given field value. However, a large loop area can not be obtained without increasing the loop inductance. Furthermore, for typical Josephson junctions we cannot neglect the displacement current due to the finite junction capacitance as well as the fluctuating noise current. In this general case the dc-SQUID circuit is governed by a set of time-dependent nonlinear equations that must be solved numerically.

The phase differences across the two junctions have to satisfy the following equations:[11,12,13]

$$V \;=\; \frac{\Phi_0}{4\pi}\left(\frac{d\varphi_1}{dt}+\frac{d\varphi_2}{dt}\right) \qquad (4.1.35)$$

$$2\pi n \;=\; \varphi_2-\varphi_1-2\pi\frac{\Phi_{\rm ext}}{\Phi_0}-2\pi\frac{LI_{\rm cir}}{\Phi_0} \qquad (4.1.36)$$

$$\frac{I}{2} \;=\; \frac{\hbar C}{2e}\frac{d^2\varphi_1}{dt^2}+\frac{\hbar}{2eR_N}\frac{d\varphi_1}{dt}+[I_c\sin\varphi_1+I_{\rm cir}]+I_{F1} \qquad (4.1.37)$$

$$\frac{I}{2} \;=\; \frac{\hbar C}{2e}\frac{d^2\varphi_2}{dt^2}+\frac{\hbar}{2eR_N}\frac{d\varphi_2}{dt}+[I_c\sin\varphi_2-I_{\rm cir}]+I_{F2}\ . \qquad (4.1.38)$$

Equation (4.1.35) relates the SQUID voltage to the rate of phase change. Note that for negligible screening we have $\frac{d\varphi_1}{dt}=\frac{d\varphi_2}{dt}$ and the usual voltage-phase relation is recovered. For finite screening this is no longer the case and we have $\frac{d\varphi_1}{dt}\neq\frac{d\varphi_2}{dt}$. Equation (4.1.36) expresses the fluxoid quantization in the superconducting loop. We see that in contrast to negligible screening (compare (4.1.8)) we have to take into account also the flux $LI_{\rm cir}$ due to the finite inductance of the loop. Equations (4.1.37) and (4.1.38) are Langevin equations coupled via $I_{\rm cir}$. These coupled equations have to be solved numerically under the constraint given by (4.1.36) as a function of the screening parameter $\beta_L = 2LI_c/\Phi_0$, the Stewart-McCumber parameter $\beta_C = 2\pi I_cR_N^2C/\Phi_0$ and the thermal noise parameter $\gamma = 2\pi k_BT/I_c\Phi_0$.

[11] C.D. Tesche, J. Clarke, *dc-SQUID: Noise and Optimization*, J. Low Temp. Phys. **27**, 301 (1977).

[12] J.J.P. Bruines, V.J. de Waal, J.E. Mooij, J. Low Temp. Phys. **46**, 383 (1982).

[13] V.J. de Waal, P. Schrijner, R. Llurba, *Simulation and Optimization of a dc-SQUID with Finite Capacitance*, J. Low Temp. Phys. **54**, 215 (1984).

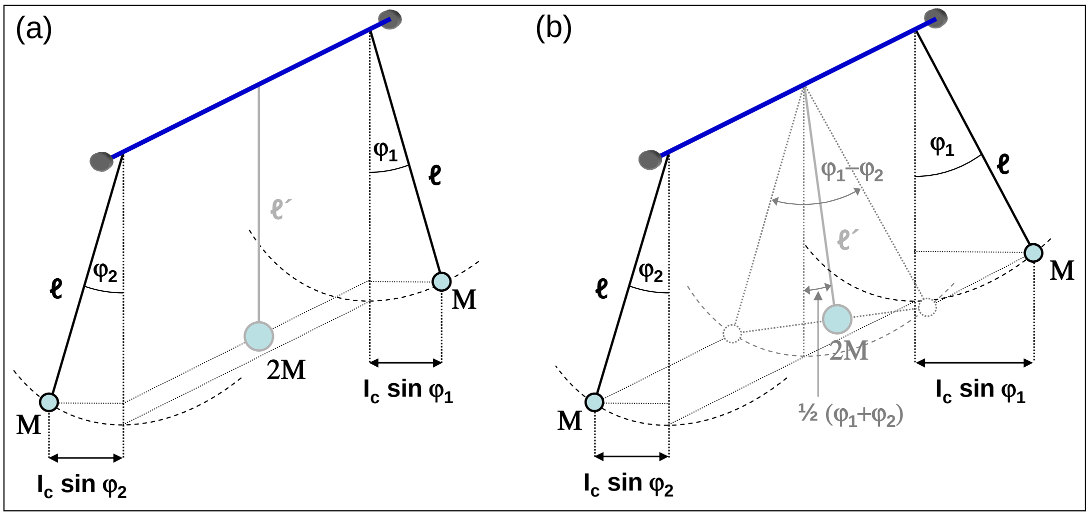

Figure 4.5: The pendulum analogue of a dc SQUID. The pendula are rigidly attached to the bar and the bar can rotate. At negligible screening ($\beta_L \ll 1$) the bar connecting the two pendula is rigid resulting in a combined pendulum with mass $2M$ at the center of mass. (a) Zero applied bias current and (b) finite bias current. The combined pendulum is shown in the center using grey lines.

Mechanical Analogue

We can gain insight into the equations of motion of a dc-SQUID by the pendulum analogue (see Fig. 4.5) already used for the single Josephson junction. The dc-SQUID formed by two identical junctions can be modeled by two pendula with the same mass M and length ℓ hanging from the same pivot point with the two pendula coupled via a twistable bar. The case of negligible screening ($\beta_L = 0$) corresponds to the case that the connecting bar is rigid. The relative angle $\varphi_1 - \varphi_2 = 2\pi\Phi_{\rm ext}/\Phi_0$ is fixed by the external flux. That is, in effect we have to deal with a single combined pendulum with its full mass $2M$ located at the center of mass halfway between the two individual masses, which is at distance $\ell' = \ell\cos[\frac{1}{2}(\varphi_1 - \varphi_2)]$ from the pivot point. Alternatively, we can consider the net gravitational torque (corresponding to the net critical current) as the vector sum of those of the two pendula. In the absence of an applied torque (applied current) the combined pendulum hangs with the center of mass pointing down with the individual pendula at $\frac{1}{2}(\varphi_1 - \varphi_2)$ on either side (see Fig. 4.5a). Note that for $(\varphi_1 - \varphi_2) = \pi$ corresponding to $\Phi_{\rm ext} = \Phi_0/2$ the center of mass is at the pivot point. As a torque (bias current) is applied this is rotating the combined pendulum (see Fig. 4.5b). The circulating current $I_{\rm cir} = \frac{1}{2}(I_c \sin\varphi_1 - \sin\varphi_2)$ is half the difference of the horizontal projections of the two pendula.

In the case of finite screening ($\beta_L > 0$) the situation is a little bit more complicated, since now the bar connecting the two pendula is no longer rigid but flexible. We can regard it as a torsional spring on the rotation axis with a loose spring corresponding to a large loop inductance and hence a large screening effect. An applied flux again results in a finite angle $\varphi_1 - \varphi_2 = 2\pi\Phi/\Phi_0$, which is given now by the total flux $\Phi = \Phi_{\rm ext} + LI_{\rm cir}$. For a large inductance L the applied flux is well screened by the circulating current so that $\Phi \sim 0$. That means, that also $\varphi_1 - \varphi_2 \sim 0$ at zero bias current. This is evident from our mechanical analogue. A large inductance corresponds to a loose spring connecting the pendula. Hence, the applied flux tries to rotate the pendula in opposite directions but they will stay in their bottom position and twist the loose spring connecting them. Due to the loose spring the difference $\varphi_1 - \varphi_2$ is no longer constant as in the case of negligible screening and hence $\frac{d\varphi_1}{dt} \neq \frac{d\varphi_2}{dt}$. As the inductance becomes smaller the connecting spring becomes stiffer and finally rigid at $\beta_L \to 0$.

4.1.3 Operation and Performance of dc-SQUIDs

The principle of operation of a dc-SQUID is shown in Fig. 4.6. The two junctions, which are modeled by the RCSJ model, are connected in parallel in a superconducting loop with inductance L. In order to eliminate hysteretic IVCs, the Stewart-McCumber parameter of the junctions is restricted to $\beta_C \leq 1$. In practice, this is usually achieved by using external shunt resistors (see Fig. 4.11). The IVCs of the SQUID depend on the applied magnetic flux as shown in Fig. 4.4 for $\beta_C \ll 1$ and $\beta_L \ll 1$. In Fig. 4.6b only the IVCs with the largest ($\Phi_{\rm ext} = n\Phi_0$) and the smallest critical current ($\Phi_{\rm ext} = (n + \frac{1}{2})\Phi_0$) are shown. When the SQUID is biased at a constant current $I > 2I_c$, the time-averaged voltage $\langle V \rangle$ of the SQUID varies periodically with the applied flux with period Φ_0 as shown in Fig. 4.6c.

For practical applications the flux threading the loop has to be measured with high resolution. Therefore, the SQUID is operated at the steepest part of the $\langle V \rangle(\Phi_{\rm ext})$ curve, where the ***flux-to-voltage transfer coefficient***

$$\boxed{H \;\; \equiv \;\; \left| \left(\frac{\partial V}{\partial \Phi_{\rm ext}} \right)_{I=const} \right|} \tag{4.1.39}$$

is a maximum. We see that the dc-SQUID can be considered as a flux-to-voltage transducer, which produces an output voltage in response to small variations of the input flux.

The resolution of the SQUID can be characterized by the ***equivalent flux noise*** $\Phi_F(t)$, which has the power spectral density

$$\boxed{S_\Phi(f) \;\; = \;\; \frac{S_V(f)}{H^2}} \tag{4.1.40}$$

at a given frequency f. Here, $S_V(f)$ is the power spectral density of the voltage noise across the SQUID at a fixed bias current. The flux noise power spectral density is inconvenient for comparing the noise in SQUIDs with different values of the loop inductance. A more convenient characterization of the noise is to use the ***noise energy*** $\varepsilon(f)$ associated with $S_\Phi(f)$:

$$\boxed{\varepsilon(f) \;\; = \;\; \frac{S_\Phi(f)}{2L} \; = \; \frac{S_V(f)}{2LH^2} \; .} \tag{4.1.41}$$

The noise energy of the dc-SQUID sets the energy resolution of the SQUID, which for practical applications should be as small as possible. For a given $S_V(f)$ we therefore have to maximize H and L. Using a plausibility consideration we see the following:

1. **Bias current *I*:** In order to maximize H we should choose a bias current just above $2I_c$, since here the modulation of the $\langle V \rangle(\Phi_{\rm ext})$ curve is largest.

2. **Flux bias:** For optimum bias current the flux bias should be close to $(2n+1)\Phi_0/4$, since here H is maximum.

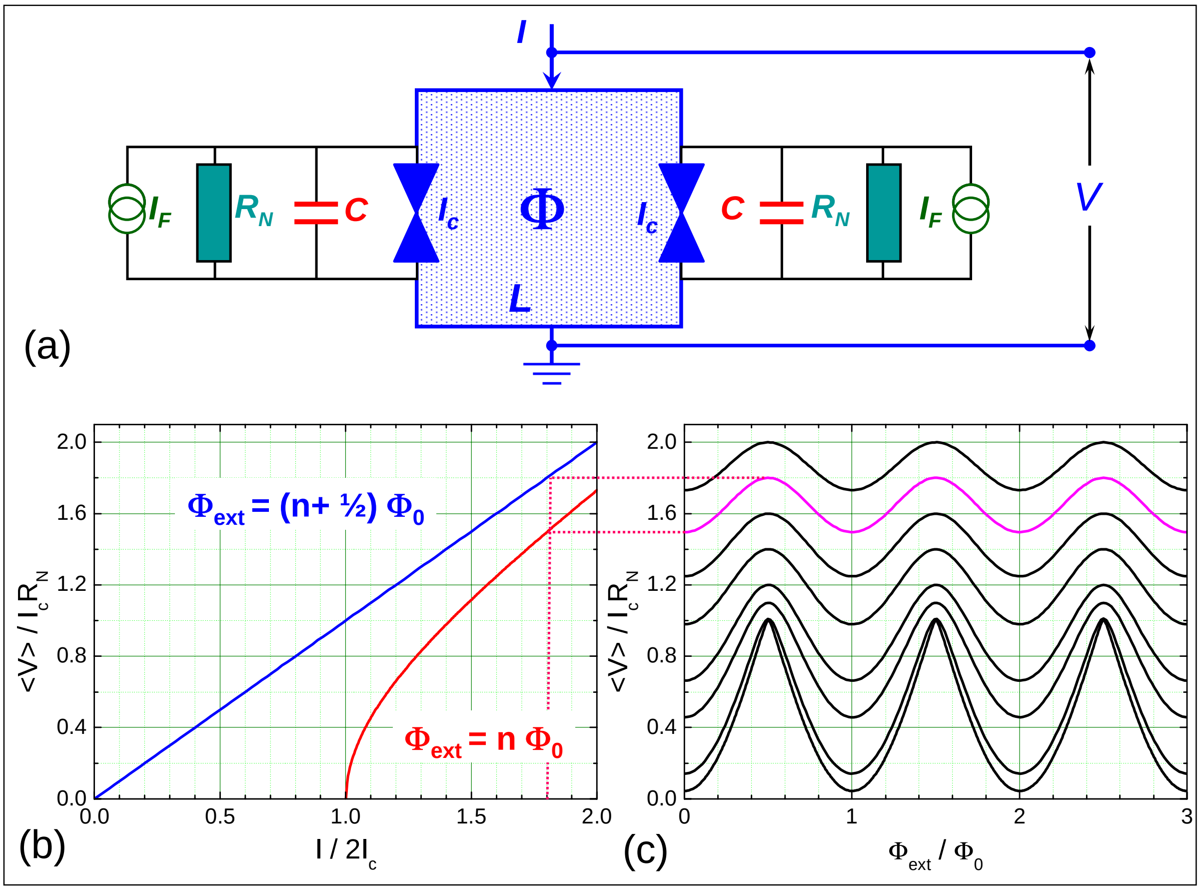

Figure 4.6: (a) The equivalent circuit of a dc-SQUID, (b) the current-voltage characteristics for two different values of the applied magnetic flux ($\Phi_{\rm ext} = n\Phi_0$ and $\Phi_{\rm ext} = (n+1/2)\Phi_0$) and (c) the time-averaged voltage plotted versus the applied flux for different values of the bias current ($I/2I_c = 1.001$, 1.01, 1.1, 1.2. 1.4, 1.6, 1.8, and 2.0).

3. **Junction critical current I_c:** The junction critical currents should be much larger than the thermal noise current, or equivalently, the coupling energy $I_c\Phi_0/2\pi$ should be much larger the the thermal energy k_BT. In this way, noise rounding of the IVCs as shown in Fig. 3.18 is avoided, which would deteriorate H. Computer simulations show that[14]

$$\frac{1}{5}\cdot I_c \quad \gtrsim \quad I_{\rm th} \equiv \frac{2\pi k_B T}{\Phi_0} \tag{4.1.42}$$

is sufficient. At 4.2 K this condition, which is equivalent to asking for a sufficient coupling of the phases of the superconducting wave functions across the two Josephson junctions, implies that $I_c \gtrsim 1\,\mu$A.

4. **The loop inductance L:** The loop inductance should be as large as possible for optimum sensitivity. However, at a given temperature T the thermal energy k_BT causes a root mean square thermal noise flux in the loop, $\langle\Phi_{\rm th}^2\rangle^{1/2} = \sqrt{k_BTL}$. This noise flux should be considerably smaller than Φ_0 giving an upper bound for L. We can define a thermal inductance $L_{\rm th}$ as the inductance value, for which the thermal noise current $I_{\rm th}$ generates just half a flux quantum in the loop, that is $L_{\rm th}I_{\rm th} = \Phi_0/2$ or $2L_{\rm th}I_{\rm th}/\Phi_0 = 1$. In order to keep the effect of thermal fluctuations small, the loop inductance L of the SQUID has to be sufficiently smaller than $L_{\rm th}$. Again, computer simulations

[14] J. Clarke, R. Koch, *The Impact of High Temperature Superconductivity on SQUIDs*, Science **242**, 217 (1988).

show that

$$5 \cdot L \quad \lesssim \quad L_{\rm th} \equiv \frac{\Phi_0}{2I_{\rm th}} \; = \; \frac{\Phi_0^2}{4\pi k_B T} \tag{4.1.43}$$

is sufficient. This constraint, which is equivalent to asking for a sufficient coupling of the phase differences of the two junctions, implies that $L \lesssim 1$ nH at 4.2 K.

In analogy to the screening parameter β_L we can define the parameter

$$\beta_{\rm th} \;=\; \frac{2I_{\rm th}L}{\Phi_0} \;=\; \frac{L}{L_{\rm th}} \;=\; \frac{I_{\rm th}}{I_c}\,\beta_L \;=\; \gamma\,\beta_L \tag{4.1.44}$$

with $\gamma = I_{\rm th}/I_c$ (compare (3.1.17)). This parameter is of crucial importance for the SQUID performance (see Fig. 4.7).

5. **The screening parameter β_L:** The screening parameter $\beta_L = 2I_cL/\Phi_0$ has to be smaller than unity to avoid hysteretic $\langle V\rangle(\Phi_{\rm ext})$ curves. This condition can be easily satisfied by making L small. However, we already have seen that we should make L as large as possible to increase the SQUID sensitivity. Therefore, we should choose $\beta_L \simeq 1$, i.e. as large as possible. For $\beta_L \simeq 1$ and taking the smallest possible I_c value at 4.2 K ($\sim 1\,\mu$A), we obtain $L \lesssim 1$ nH, which is still compatible with the constraint given by (4.1.43).[15]

6. **The Stewart-McCumber parameter β_C:** The Stewart-McCumber parameter has to be smaller than unity in order to avoid hysteretic IVCs. For superconducting tunnel junctions, which intrinsically have large capacitance and hence $\beta_C \gg 1$, this is achieved by using an external shunt resistor smaller than the normal resistance of the junction (see Fig. 4.11). That is, in principle it is not a problem to satisfy the condition $\beta_C \leq 1$. However, using a small shunt resistor $R_{\rm shunt} \ll R_N$ reduces the voltage amplitude of the $\langle V\rangle(\Phi_{\rm ext})$ curves to $I_cR_{\rm shunt} \ll I_cR_N$. Therefore, $R_{\rm shunt}$ should be as large as possible, that is, we have to choose $\beta_C \simeq 1$.

The detailed values of the parameters describing the performance of the SQUID have to be evaluated by numerical simulations.[16,17,18,19] These simulations show that the noise energy of dc-SQUIDs has a minimum for $\beta_L \simeq 1$, $\beta_C \simeq 1$, for a flux bias close to $(2n+1)\Phi_0/4$ and for a bias current I, for which the voltage modulation of the $\langle V\rangle(\Phi_{\rm ext})$ curves is largest. Since the maximum voltage modulation is about I_cR_N we have

$$H \;\simeq\; \frac{I_cR_N}{\Phi_0/2} \simeq \frac{R_N}{L} \tag{4.1.45}$$

for $\beta_L \simeq 1$. In the white noise regime[20] the voltage noise of the SQUID can be estimated by splitting up the current noise power spectral density S_I into an in-phase part $S_I^{in} = 4k_BT/(R_N/2)$ and an out-of-phase

[15]Note that for high temperature superconductor dc-SQUIDs the operation temperature is about 20 times higher and therefore we have the constraint $I_c \gtrsim 20\,\mu$A and $L \lesssim 50$ pH. Again, for $\beta_L \simeq 1$ we obtain with $I_c \simeq 20\,\mu$A an inductance value $L \lesssim 50$ pH, which is compatible with the thermal constraint. However, due to the smaller inductance value it is in general more difficult to couple magnetic flux into the SQUID loop.

[16]C.D. Tesche, J. Clarke, *dc-SQUID: Noise and Optimization*, J. Low Temp. Phys. **27**, 301 (1977).

[17]D. Drung, W. Jutzi, IEEE Trans. Magn. **21**, 330 (1985).

[18]D. Kölle, R. Kleiner, F. Ludwig, E. Dantsker, J. Clarke, *High-transition-temperature superconducting quantum interference devices*, Rev. Mod. Phys. **71**, 631 (1999).

[19]J. Clarke, A.I. Braginski (eds.), *The SQUID Handbook*, Vol. 1: “Fundamentals and Technology of SQUIDS and SQUID Systems” Wiley-VCH, Weinheim (2004).

[20]The low-frequency regime, where $1/f$ noise dominates is not discussed here.

part $S_I^{out} = 4k_BT/2R_N$. Note that for the in-phase current fluctuations, which have the same direction in the two arms of the SQUID, the relevant resistance is $R_N/2$ due two the parallel connection of the two junction resistors. In contrast, for the out-of-phase part, which is in opposite direction in the two arms and results in a circulating current, the relevant resistance is $2R_N$ due to the series connection of the two junctions resistors for the circulating current. In a small signal analysis the voltage noise power spectral density due to the in- and out-of-phase current fluctuations is given by[21,22,23]

$$S_V(f) \quad = \quad S_I^{in}(f)R_d^2 + S_I^{out}(f)\,L^2\,H^2 \;=\; \frac{4k_BT}{R_N}\left[2R_d^2 + \frac{L^2H^2}{2}\right] \;, \qquad (4.1.46)$$

where R_d is the differential resistance at the operation point. With the optimum values $H \sim R_N/L$ and $R_d \sim \sqrt{2}R_N$ obtained from numerical simulations we obtain

$$S_V(f) \quad \simeq \quad \frac{4k_BT}{R_N}\left[4R_N^2 + \frac{R_N^2}{2}\right] \;=\; 18k_BTR_N \;. \qquad (4.1.47)$$

The noise energy then can be estimated to

$$\varepsilon(f) \quad = \quad \frac{S_V(f)}{2LH^2} \simeq \frac{9k_BTL}{R_N} \simeq \frac{9k_BT\Phi_0}{2I_cR_N} \qquad \text{for} \quad \beta_L \simeq 1 \;. \qquad (4.1.48)$$

We see that the noise energy increases with temperature and decreasing I_cR_N product of the Josephson junctions. If we eliminate R_N by using $\beta_C = 2\pi I_cR_N^2C/\Phi_0 \simeq 1$ and if we also eliminate L by using $\beta_L = 2I_cL/\Phi_0 \simeq 1$ we obtain

$$\boxed{\begin{aligned}\varepsilon(f) \quad &\simeq \quad 16k_BT\sqrt{\frac{LC}{\beta_C}} \\ &\simeq \quad 16\sqrt{\pi}k_BT\sqrt{\frac{\Phi_0C_s}{2\pi J_c}} \;=\; \frac{16\sqrt{\pi}k_BT}{\omega_p} \qquad \text{for} \quad \beta_L \simeq 1; \;\; \beta_C \simeq 1 \;.\end{aligned}} \qquad (4.1.49)$$

Here, $C_s = C/A$ is the specific junction capacitance and $J_c = I_c/A$ the critical current density of the junction. We see that we can improve the performance of the dc-SQUID by reducing the temperature as well as by decreasing the capacitance and by increasing the critical current density, i.e. by increasing the plasma frequency of the Josephson junctions. Today critical current densities above 10^3A/cm^2 are used requiring junction areas of the order of $1\,\mu$m^2 for realizing critical current values of a few μA. Until today, a large number of dc-SQUIDs has been studied and it was found that their performance agrees well with the predictions of the numerical simulations. Today it is common to quote the noise

[21] We note that in a more detailed analysis the voltage noise of a single Josephson junction at a measuring frequency f much smaller than the Josephson frequency f_J is given by

$$S_V(f) \quad = \quad \frac{4k_BT}{R_N}\,R_d^2 + \frac{4k_BT}{R_N}\,R_d^2\,\frac{1}{2}\left(\frac{I_c}{I}\right)^2 \;,$$

where the first term is the usual Nyquist noise and the second represents the Nyquist noise generated at frequencies $f_J \pm f$ mixed down to the measurement frequency by the Josephson oscillations due to the nonlinearity of the IVC. The factor $\frac{1}{2}\left(\frac{I_c}{I}\right)^2$ is the mixing coefficient, which vanishes at large bias currents $I \gg I_c$. Furthermore, at sufficiently high bias currents the Josephson frequency exceeds k_BT/h and quantum corrections become important (compare section 3.5.5).

[22] K.K. Likharev, V.K. Semonov, JETP Lett. **15**, 442 (1972).

[23] R.H. Koch, D.J. van Harlingen, J. Clarke, Phys. Rev. Lett. **45**, 2132 (1980).

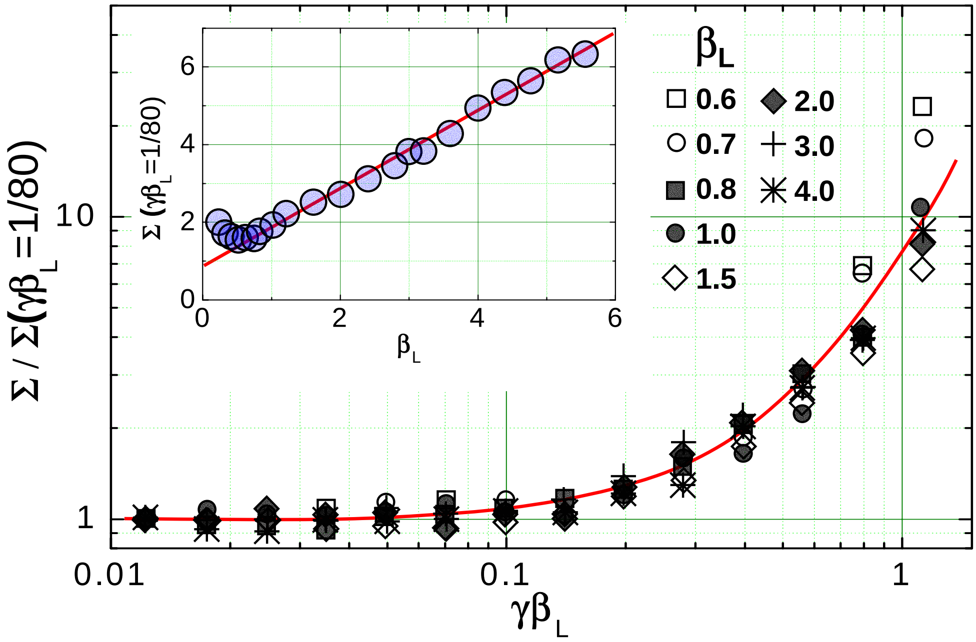

Figure 4.7: Calculated reduced energy resolution $\Sigma(\gamma\beta_L)$ normalized to $\Sigma(\gamma\beta_L = 1/80)$. Inset shows $\Sigma(\gamma\beta_L = 1/80)$ versus β_L (data from D. Kölle *et al.*, Rev. Mod. Phys. **71**, 631 (1999)).

energy of SQUIDs in units of $\hbar \simeq 10^{-34}$Js. Optimized SQUIDs have a noise energy approaching the quantum limit $\hbar$. However, these SQUIDs have very low inductance and therefore are not useful for most applications requiring optimum magnetic field resolution. Best practical dc SQUIDs have reached an energy resolution of some $10\hbar$.[24]

A recent result of a numerical simulation is shown in Fig. 4.7. Here, the reduced noise energy

$$\Sigma(f) = \frac{\varepsilon(f)}{\frac{2\Phi_0 k_B T}{I_c R_N}} \tag{4.1.50}$$

is plotted versus the dimensionless parameter

$$\beta_{\rm th} = \gamma\beta_L = \frac{2\pi k_B T}{I_c \Phi_0}\,\frac{2 I_c L}{\Phi_0} = \frac{L}{\frac{\Phi_0^2}{4\pi k_B T}} \equiv \frac{L}{L_{\rm th}} . \tag{4.1.51}$$

For $\gamma\beta_L \leq 0.2$ corresponding to $L \leq \frac{1}{5}L_{\rm th}$, the reduced noise energy is almost constant, while for higher values of $\gamma\beta_L$ it increases rapidly. The rapid increase in noise energy arises from the rapid degradation of the transfer function with increasing $\gamma\beta_L = L/L_{\rm th}$ due to thermal noise rounding of the IVCs.

4.1.4 Practical dc-SQUIDs

Practical dc-SQUIDs do not only consist of the SQUID loop discussed so far, but also of an antenna and a room temperature electronics as schematically shown in Fig. 4.8. The antenna has both to transfer the quantity that has to be measured into magnetic flux and to couple this flux effectively into the SQUID loop. The SQUID itself acts as a flux-to-voltage transducer. The room temperature electronics has to amplify the voltage signal as well as to provide the current and flux bias.

[24] A.A. Jin, T.R. Stevenson, F.C. Wellstood, W.W. Johnson, IEEE Trans. Appl. Supercond. **AS-7**, 2742 (1997).

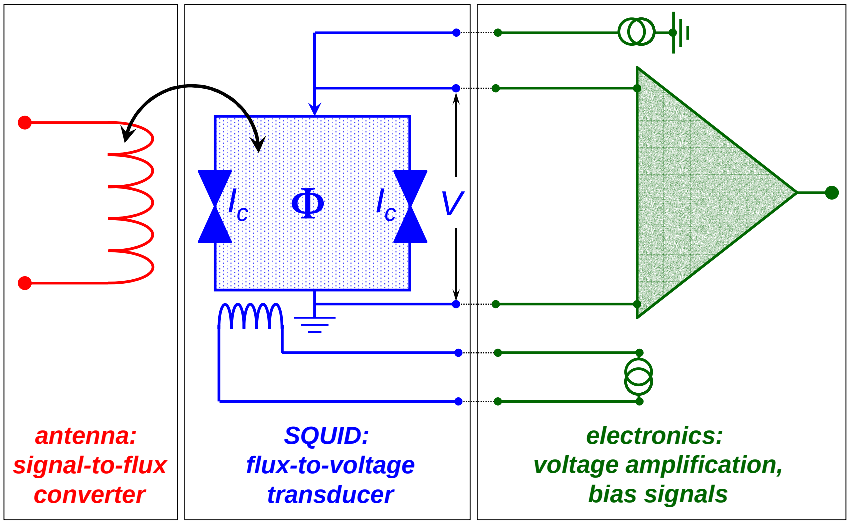

Figure 4.8: The practical dc-SQUID consisting of an antenna acting as a signal-to-flux converter, the SQUID loop acting as the flux-to-voltage transducer, and the room temperature electronics.

The Washer Type dc-SQUID

Obviously, a large area A of the SQUID loop is advantageous to increase the sensitivity of a SQUID, since small field changes ΔB then result in large flux changes $\Delta\Phi_{\rm ext} = A \cdot \Delta B$. However, a large A also results in a large loop inductance L, which may deteriorate the SQUID performance as discussed above. Based on this conflicting requirements various SQUID designs have been developed. In the 1970ies and 1980ies, often three-dimensional loop geometries have been used for the realization of SQUIDs (e.g. by evaporation of a cylinder containing the Josephson junctions on a thin quartz thread).

Today dc-SQUIDs are based on thin film structures, which are patterned using optical and electron beam lithography. Here, a large effective loop area at small loop inductance can be achieved by making use of the perfect diamagnetism of superconductors. As shown in Fig. 4.9, instead of a narrow superconducting loop structure a broad "washer-type" structure can be used. Such geometries have been successfully used for high T_c dc-SQUIDs using grain boundary Josephson junctions.[25,26,27] The washer design was first proposed by **M.B. Ketchen** and therefore these SQUID structures today are denoted as Ketchen-type SQUIDs.[28] This geometry also helps to overcome the problem of coupling the magnetic flux of the antenna system effectively to the SQUID loop of a thin film SQUID. In 1981 **M.B. Ketchen** and **J.M. Jaycox** introduced the idea of depositing a planar spiral input coil on a dc-SQUID in a square washer geometry.[29,30] The thin film planar coil is separated from the SQUID washer only by a thin insulating layer. A typical washer type dc-SQUID is shown schematically in Fig. 4.11. The square washer forms the SQUID loop. It contains a narrow slit, which is closed by a superconducting line containing the two junctions, which are located at the outer rim of the washer.

For the washer geometry shown in in Figs. 4.9 and 4.11, the loop currents circulate around the inner opening (hole or slit) of the washer, which then determines the inductance of the SQUID loop. **Jaycox** and **Ketchen** showed that a square washer with a hole of diameter D (without slit) and an outer edge W

[25] R. Gross *et al.*, Appl. Phys. Lett. **57**, 727 (1990).
[26] R. Gross *et al.*, Physica **C 170**, 315 (1990).
[27] D. Kölle *et al.*, Rev. Mod. Phys. **71**, 631 (1999).
[28] M.B. Ketchen, IEEE Trans. Magn. **MAG-17**, 387 (1980).
[29] M.B. Ketchen, J.M. Jaycox, *Ultra-low Noise Tunnel Junction dc-SQUID with a Tightly Coupled Planar Input Coil*, Appl. Phys. Lett. **40**, 736 (1982).
[30] J.M. Jaycox, M.B. Ketchen, *Planar Coupling Scheme for Ultra-low Noise dc-SQUIDs*, IEEE Trans. Magn. **17**, 400 (1981).

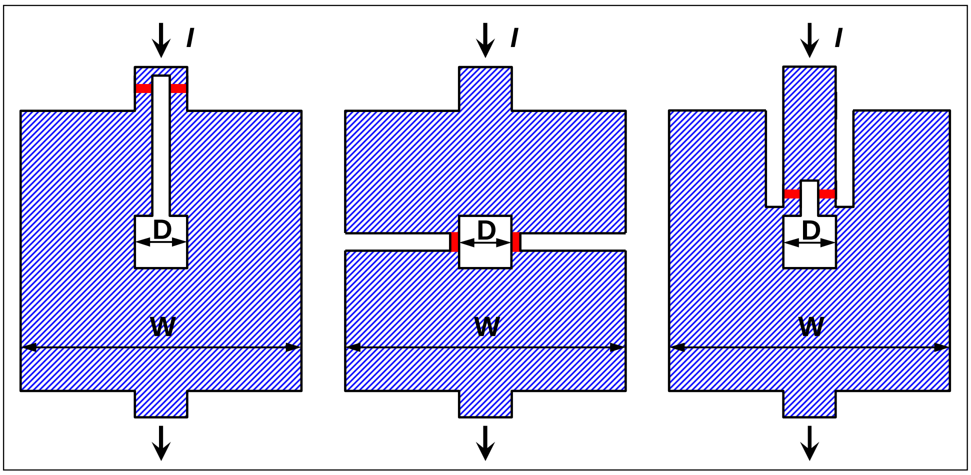

Figure 4.9: Sketch of various geometries for planar dc-SQUIDs with washer geometry.

has the inductance

$$L \simeq 1.25\,\mu_0 D \tag{4.1.52}$$

in the limit $W \gg D$. That is, the loop inductance scales with the inner diameter D. In contrast, the effective area of the SQUID loop is[31]

$$A_{\rm eff} \propto D \cdot W \ , \tag{4.1.53}$$

that is, it scales with the outer dimension of the washer. Of course, one cannot increase W arbitrarily, since for large W one starts to trap magnetic flux quanta in the washer area during cool down even in small magnetic fields. The thermally activated motion of these flux quanta generate disturbing $1/f$-noise. An experimental example for the flux focusing effect is shown in Fig. 4.10 for a geometry shown in the inset. Here, $A_{\rm eff}/D^2$ is plotted versus W^2/D^2 on a double logarithmic scale. In such plot a straight line with slope $1/2$ is expected according to (4.1.53) in good agreement with the data.

We briefly address the inductance and the coupling of a spiral input coil that can be put on top of the washer as shown in Fig. 4.11. Neglecting the parasitic inductance associated with the Josephson junctions, the following expressions for the inductance L_i of the spiral input coil, the mutual inductance M_i and the coupling coefficient α^2 between the spiral and the SQUID loop are found:

$$L_i \simeq n^2 L + L_s \tag{4.1.54}$$

$$M_i \simeq \sqrt{n^2 L \cdot L} = nL \tag{4.1.55}$$

$$\alpha^2 \simeq \frac{1}{1 + L_s/n^2 L} \ . \tag{4.1.56}$$

Here, L_s is the stripline inductance of the spiral coil, n the number of turns of the spiral input coil and n^2L the geometric self-inductance of the input coil. For the estimate of M_i we have assumed that the flux due to a current flowing in the spiral input coil is perfectly coupled in the SQUID hole. The coupling coefficient α is obtained from the expression $\alpha = M_i/\sqrt{L_i L} = nL/\sqrt{(n^2L + L_s)L}$. As an example, for $D = 20\,\mu$m we obtain $L \simeq 30$ pH. For a 50 turn input coil we obtain $L_i \simeq 75$ nH[32] and $M_i \simeq 1.5$ nH. The

[31] M.B. Ketchen, W.J. Gallagher, A.W. Kleinsasser, S. Murphy, J.R. Clem, in *SQUID'85*, H.D. Hahlbohm and H. Lübbig eds., Walther de Gruyter, Berlin (1985), p. 865.

[32] The stripline inductance is usually negligible for a 50 turn coil.

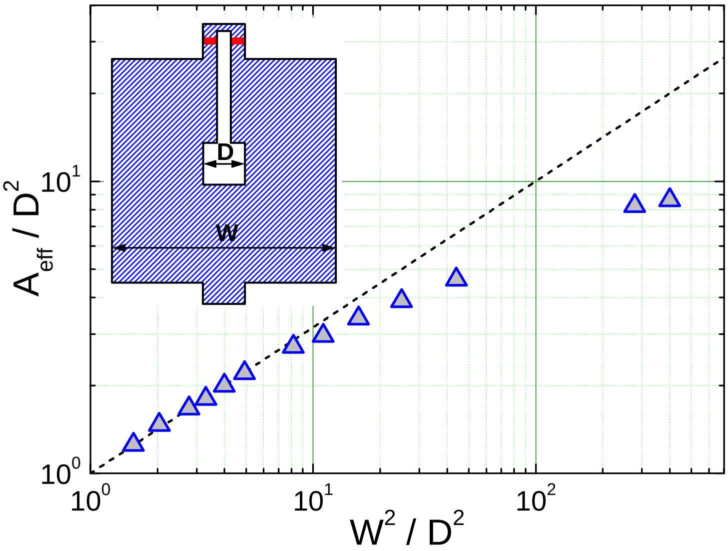

Figure 4.10: Flux focusing effect in a washer-type $YBa_2Cu_3O_{7-\delta}$ grain boundary junction dc SQUID measured at 77 K. The dashed line shows the theoretical dependence expected according to (4.1.53). The deviations at large W^2/D^2 values are caused by the finite slit inductance of the used washer geometry shown in the inset (data according to R. Gross *et al.*, Appl. Phys. Lett. **57**, 727 (1990)).

experimentally determined coupling coefficient typically ranges between 0.6 and 0.8. A specific problem of the washer-type dc SQUID geometry is the considerable capacitance between the spiral input coil and the square washer. This can result in LC-resonances. These resonances, in turn, result in structures in the IVCs, which can give rise to excess noise. The effect of the LC-resonances can be reduced by reducing the number of turns on the washer and thereby reducing the parasitic capacitance (in this case an intermediate superconducting transformer can be used to couple in the signal). On the other hand, the shunt resistance of the junctions can be decreased thereby increasing the damping.

Low-T_c dc-SQUIDs: Low-T_c dc SQUIDs are fabricated using standard multilayer thin film technology (cf. Fig. 4.11). In order to increase the energy sensitivity, Josephson junctions with a high plasma frequency have to be used. This is achieved by using high critical current density junctions, which allow to minimize the junction area and hence the junction capacitance. Although various materials combinations have been used so far, the most successful is the combination of niobium and aluminium. This combination is stable in time and not affected by thermal cycling. Furthermore, Nb/AlO_x/Nb tunnel junctions show a low level of $1/f$ noise due to critical current fluctuations compared to e.g. NbN/MgO/NbN junctions.

High-T_c dc-SQUIDs: Today high-T_c dc-SQUIDs are also fabricated using multilayer thin film technology. However, in contrast to low-T_c materials an heteroepitaxial growth of the different superconducting layers is required to avoid grain boundaries in the thin film structures. These are known to be responsible for a high level of $1/f$-noise. A further problem in the fabrication of high-T_c dc-SQUIDs is the poor reproducibility of the junctions. Various junction types such as grain boundary junctions, ramp junctions or edge junctions have been used with different success.[33,34]

Due to the problem of heteroepitaxial growth of multilayer structures the integration of the input coil

[33] R. Gross, P. Chaudhari, *Status of dc-SQUIDs in the High Temperature Superconductors*, in *Principles and Applications of Superconducting Quantum Interference Devices*, pp. 419–479, A. Barone ed., World Scientific, Singapore (1992).

[34] For a more recent review see D. Kölle *et al.*, Rev. Mod. Phys. **71**, 631 (1999).

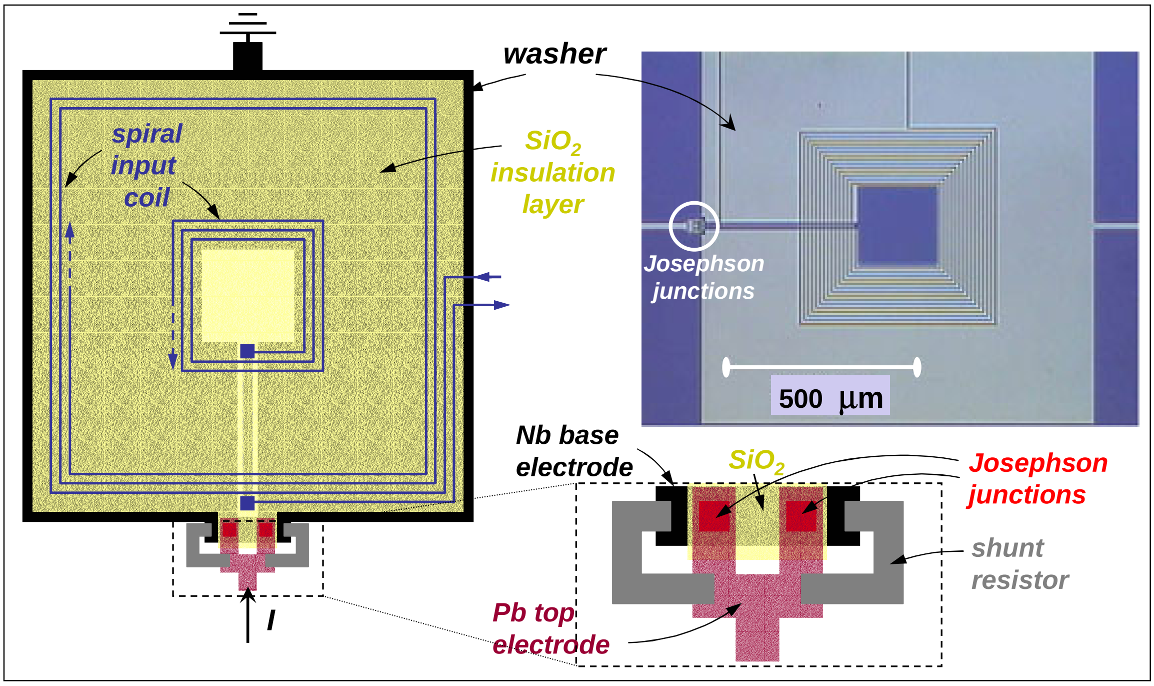

Figure 4.11: Sketch of a Nb/Pb dc-SQUID using a square washer geometry and a planar spiral input coil. The junction area is shown on an enlarged scale on the right. Also shown is an optical micrograph of a washer-type Pb/Nb dc-SQUID (by courtesy of J. Clarke).

on a washer structure is still a challenge for high-T_c SQUIDs.[35,36] Therefore, often so-called flip-chip structures have been applied where the input coil is fabricated on a separate chip and then flip-chipped on the washer.[37]

In order to avoid complicated multilayer structures it is also common to use directly coupled high-T_c dc-SQUIDs. Here, the SQUID loop is directly coupled to a parallel loop that acts as a signal pick-up loop. The big advantage of such directly coupled SQUIDs is the fact that only a single superconducting layer is required that can be grown with high quality on a single or bi-crystalline substrate. A schematic drawing of such a SQUID can be found in Fig. 4.22). For such directly coupled dc-SQUIDs field sensitivities down to 20 fT/$\sqrt{\text{Hz}}$ have been obtained in the white noise regime at 77 K.[38]

4.1.5 Read-Out Schemes

The Flux-Locked Loop Operation

The $\langle V\rangle(\Phi_{\rm ext})$ curves of the dc-SQUID are nonlinear. Therefore, a linear relation between an input signal and the output voltage is obtained only in the small signal limit. This problem can be solved by using the SQUID in a feedback circuit as a null-detector for magnetic flux.[39] One simply applies an oscillating magnetic flux with a peak-to-peak amplitude of about $\Phi_0/2$ and a frequency $f_{\rm mod}$ in the 100 kHz regime as shown in Fig. 4.12. If the quasistatic flux is exactly $n\Phi_0$, the resulting ac voltage is a rectified version

[35] J.W.M. Hilgenkamp, G.C.S. Brons, J.G. Soldevilla, R.P. Ijsselstein, J. Flokstra, H. Rogalla, Appl. Phys. Lett. **64**, 3497-3499 (1994).
[36] B. David, D. Grundler, J.P. Krumme, O. Doessel, IEEE Trans. Appl. Supercond. **AS-5**, 2935-2938 (1995).
[37] P.A. Nilsson, Z.G. Ivanov, E.A. Stephantsov, H.K. Hemmes, J.W.M. Hilgenkamp, J. Flokstra, Inst. Phys. Conf. Ser. **148**, 1537-1540 (1995), D. Dew-Highes ed., Institute of Physics, Bristol.
[38] D. Kölle, A.H. Micklich, F. Ludwig, E. Dantsker, D.T. Nemeth, J. Clarke, Appl. Phys. Lett. **63**, 2271-2273 (1993).
[39] J. Clarke, W.M. Goubau, M.B. Ketchen, J. Low. Temp. Phys. **25**, 99 (1976).

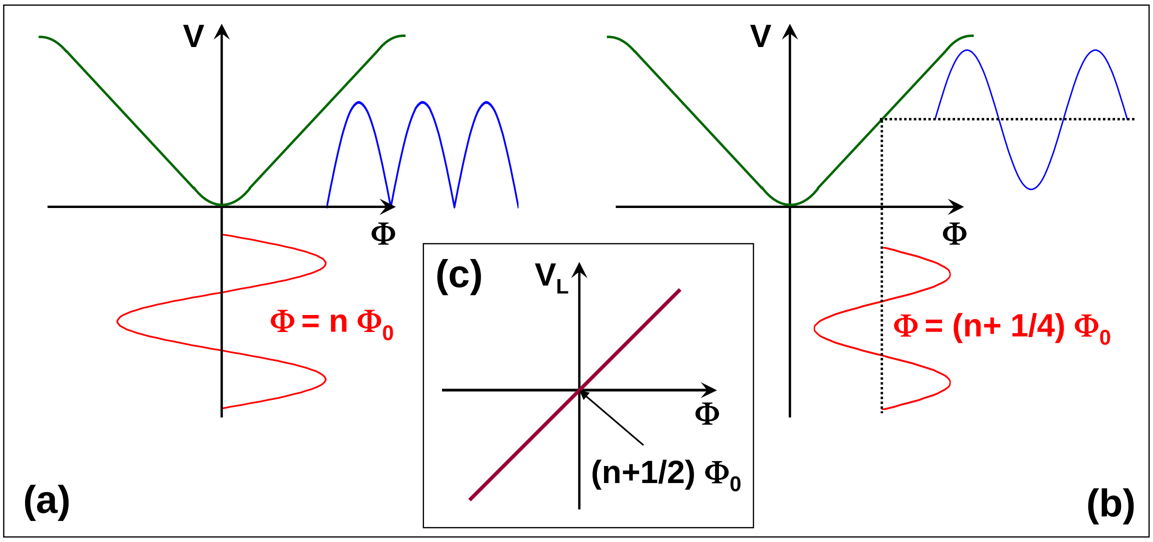

Figure 4.12: Flux modulation scheme for a dc-SQUID showing the voltage across the SQUID for (a) $\Phi = n\Phi_0$ and (b) $\Phi = (n+\frac{1}{4})\Phi_0$. In (c) the output signal V_L of the lock-in amplifier is plotted versus the applied flux.

of the input signal. That is, it contains only a $2f_{\rm mod}$ frequency component. If this signal is detected by a lock-in amplifier referenced to the fundamental frequency $f_{\rm mod}$, the resulting output voltage is zero. In contrast, if the quasistatic flux is $(n+\frac{1}{4})\Phi_0$, the voltage across the SQUID is at $f_{\rm mod}$ and the output signal from the lock-in amplifier will be maximum. Thus, increasing the flux from $n\Phi_0$ to $(n+\frac{1}{4})\Phi_0$ the lock-in output signal will increase, whereas it will increase in the negative direction on decreasing the flux from $n\Phi_0$ to $(n-\frac{1}{4})\Phi_0$. Instead of a sinusoidal a square-wave flux signal can be used. Then, for the operation point $\Phi = n\Phi_0$ and a peak-to-peak amplitude of $\Phi_0/2$ the SQUID is biased at the points of maximum slope of the $\langle V\rangle(\Phi_{\rm ext})$ curve for each half-wave of the square-wave signal.

The ac voltage across the SQUID is usually coupled to a low noise preamplifier via a cooled transformer, which results in an increase of the low SQUID impedance from R_d to N^2R_d, where R_d is the differential resistance of the SQUID at the operation point and N the turns-ratio of the transformer. One also can use a cooled LC series resonant circuit, which provides an impedance Q^2R_d, where Q is the quality of the tank circuit. The values of N or Q are chosen to obtain an optimum impedance match between the SQUID and the room temperature preamplifier.

Fig. 4.13 shows the equivalent circuit of a dc-SQUID operated in the ***flux-locked loop***. An oscillator applies a modulating flux to the SQUID and also serves as the reference for the lock-in amplifier. After amplification, the ac voltage signal from the SQUID is phase sensitively detected by the lock-in amplifier. The output voltage V_L of the lock-in amplifier is sent to an integrator. The output voltage of the integrator is decreasing and increasing for negative and positive V_L, respectively. The output signal of the integrator is connected to the SQUID via a resistor R_f to the feedback coil L_f. If we are applying a small flux change $+\delta\Phi$ to the SQUID, the lock-in will generate a positive output voltage proportional to $\delta\Phi$. The positive output signal will cause an increase of the integrator output voltage, which in turn is causing an increase of the current through the feedback coil. The integrator voltage will increase until the current through the feedback coil is sufficient to compensate the small applied flux change. Then, the total flux coupled to the SQUID and, in turn, the lock-in signal is zero and the integrator output voltage stays constant. We see that the SQUID is operating as a null detector.

The change $\delta V_{\rm in}$ of the integrator output voltage is directly proportional to the flux change $\delta\Phi$. With the change of the feedback current $\delta I_f = \delta V_{\rm in}/R_f$ and the flux induced by the feedback current, $\delta\Phi_f = k^2L_f\delta I_f$ (here k^2 is the coupling constant between the feedback coil and the SQUID loop), we obtain

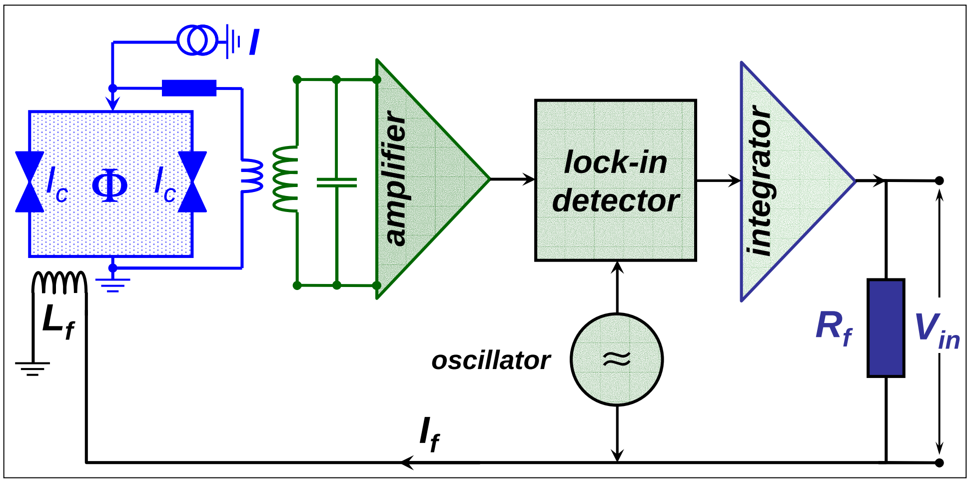

Figure 4.13: The modulation and feedback circuit of a dc-SQUID.

from the condition $|\delta\Phi_f| = |\delta\Phi|$

$$\delta V_{\rm in} = \frac{R_f}{k^2 L_f}\,\delta\Phi\ . \tag{4.1.57}$$

We see that the output signal increases with increasing feedback resistance. Furthermore, the output signal is linear with $\delta\Phi$ even if the flux change is several Φ_0.

The typical modulation frequency of the flux-locked loop circuit is from 100 kHz to several MHz. Using suitable electronics a very high dynamic range above 140 dB and a signal bandwidth of up to 100 kHz can be achieved. An important quantity is the slew rate, which gives the speed at which the feedback circuit can compensate for rapid flux changes at the input. State of the art SQUID electronics has slew rates of up to $10^7\Phi_0$/s.

Bias Current Reversal: For dc-SQUIDs based on high temperature superconductors often the bias current is modulated in addition to the flux. The reason for that is that Josephson junctions based on high temperature superconductors usually show large low-frequency fluctuations of the critical current.[40,41,42,43] These fluctuations can be eliminated by a periodic reversal of the bias current.[44,45] Since the fluctuations of the critical current of the two junctions are independent, they can be separated in a symmetric and antisymmetric part. The symmetric part results in a shift of the $V(\Phi_{\rm ext})$ curves along the voltage axis. This shift is eliminated by the flux modulation technique discussed above, since only the modulated signal at $f_{\rm mod}$ is detected by the lock-in amplifier. In contrast, the asymmetric part corresponds to a circulating current, which induces magnetic flux fluctuations and hence results in a shift of the $V(\Phi_{\rm ext})$ curve along the flux axis. By a periodic reversal of the bias current at a frequency $f_{\rm rev}$ much larger than the low-frequency I_c-fluctuations one obtains a periodic shift of the $V(\Phi_{\rm ext})$ curve in opposite directions. Then, by averaging over several periods also the asymmetric fluctuations can be eliminated.

[40] R. Gross, P. Chaudhari, M. Kawasaki, A. Gupta, M. B. Ketchen, IEEE Trans. Magn. **MAG-27**, 2565 (1991).

[41] R. Gross, *Grain Boundary Josephson Junctions in the High Temperature Superconductors*, in *Interfaces in High-T_c Superconducting Systems*, S. L. Shinde and D. A. Rudman eds., Springer Verlag, New York (1994), pp. 176-210

[42] A. Marx, L. Alff, R. Gross, IEEE Trans. Appl. Supercond. **7**, 2719 (1997).

[43] A. Marx, R. Gross, Appl. Phys. Lett. **70**, 120 (1997).

[44] R.H. Koch, J. Clarke, W. M. Goubau, J. M. Martinis, C. M. Pegrum, and D. J. Van Harlingen, J. Low Temp. Phys. **51**, 207 (1983).

[45] V. Foglietti, W. J. Gallagher, M. B. Ketchen, A. W. Kleinsasser, R. H. Koch, S. I. Raider, and R. L. Sandstrom, Appl. Phys. Lett. **49**, 1393 (1986).

The application of both flux modulation and bias current reversal is called double modulation technique. It can reduce the low-frequency $1/f$-noise of SQUIDs based on high temperature superconductors by several orders of magnitude.[46,47]

Additional Positive Feedback: An important reason for the use of the flux modulation technique is the fact that the voltage changes $\delta V(\Phi_{\rm ext})$ (typically less than $100\,\mu$V/Φ_0) and the SQUID impedance (typically a few Ω) are small. This is inadequate for semiconductor devices. Applying the flux modulation, the SQUID impedance can be increased by a step-up transformer and matched to the room temperature semiconductor electronics. An alternative way is to use the ***additional positive feedback*** (APF) technique, in which part of the bias current is used to obtain an asymmetric $V(\Phi_{\rm ext})$ dependence with a steep slope and hence larger value for $\partial V/\partial\Phi$. In this case a direct read-out of the SQUID signal with low noise room temperature semiconductor electronics is possible.[48,49]

Additional Topic:
Digital Read-Out Schemes

Fujimaki *et al.*[50] and **Drung** *et al.*[51,52] have developed schemes in which the output from the SQUID is digitized and fed back to the SQUID as an analog signal to flux-lock the loop. Fujimaki *et al.* used Josephson digital circuits to integrate their feedback system on the same chip as the SQUID. Drung *et al.* obtained a flux resolution of about $10^{-6}\Phi_0/\sqrt{\rm Hz}$ in a 50 pH SQUID. They were also able to reduce the $1/f$ noise by using a modified bias current modulation scheme. In general, the cryogenic digital feedback schemes have the advantage that they are compact, offer wide flux-locked bandwidth and produce digitized output signals for transmission to room temperature.

Additional Topic:
The Relaxation Oscillation Scheme

Mück and **Heiden** have operated a dc SQUID with hysteretic junctions in a relaxation oscillator.[53] Here, the SQUID is shunted by a series connection of an inductor and resistor. The circuit performs relaxation oscillations at a frequency depending on the flux in the SQUID. The oscillation frequency has a minimum for $(n+\frac{1}{2})\Phi_0$ and a maximum for $n\Phi_0$ with a typical frequency modulation of about 100 kHz at an oscillation frequency of about 10 MHz. The advantage of this scheme is that it produces a large voltage across the SQUID so that no matching network to the room temperature electronics is required. The room temperature electronics is allowed to be simple and compact. A flux resolution of about $10^{-5}\Phi_0/\sqrt{\rm Hz}$ for a 80 pH SQUID operated at 4.2 K has been achieved. The so-called double relaxation oscillation SQUID (DROS) is briefly addressed in section 4.3.1.

[46] R.H. Koch, W. Eidelloth, B. Oh, R. P. Robertazzi, S. A. Andrek, and W. J. Gallagher, Appl. Phys. Lett. **60**, 507 (1992).

[47] A.H. Micklich, D. Koelle, E. Dantsker, D. T. Nemeth, J. J. Kingston, R. F. Kroman, and J. Clarke, IEEE Trans. Appl. Supercond. **3**, 2434 (1993).

[48] D. Drung, Physica **C 368**, 134 (2001).

[49] D. Drung, in *SQUID Sensors: Fundamentals, Fabrication and Applications*, NATO Science Series E: Applied Sciences, Vol. 329, Kluwer Academic Publishers, Dordrecht, Boston, London (1996).

[50] N. Fujimaki, H. Tamura, T. Imamura, S. Hasuo, ISSCC San Francisco, (1988), pp. 40-41.

[51] D. Drung, Cryogenics **26**, 623-627 (1986).

[52] D. Drung, E. Crocoll, R. Herwig, M. Neuhaus, W. Jutzi, IEEE Trans. Magn. **MAG-25**, 1034-1037 (1989).

[53] M. Mück, C. Heiden, IEEE Trans. Magn. **MAG-25**, 1151-1153 (1989).

4.2 Additional Topic: The rf-SQUID

In contrast to the dc SQUID the rf-SQUID is formed by a superconducting loop containing only a single Josephson junction. Although it is still widely used today, it has seen less development in recent years compared to the dc SQUID. Whereas the dc SQUID is operated by applying a dc current and measuring the time-averaged voltage, the rf-SQUID is operated by applying an rf current via a tank circuit inductively coupled to the SQUID loop and measuring the time-averaged rf-voltage of the tank circuit. This makes the choice of names obvious. The advantage of the rf-SQUID compared to the dc SQUID is the fact that it requires only a single Josephson junction and no dc current has to be applied. Therefore, no current leads have to be attached which guarantees safe operation and good protection against current spikes. However, as we will see below, at 4.2 K the energy resolution of the rf-SQUID is limited by the read-out electronics and therefore is worse than that of dc-SQUIDs. However, at 77 K, the commonly used operation temperature of SQUIDs based on high temperature superconductors, this problem is relaxed. Although less sensitive than the dc-SQUID, the rf-SQUID is entirely adequate for a large variety of applications and is until today more widely used than the dc SQUID.

4.2.1 The Zero Voltage State

We consider the rf-SQUID shown in Fig. 4.14. In the same way as for the dc SQUID the total phase change along a closed contour line is $2\pi n$:

$$\oint_C \nabla\theta \cdot d\mathbf{l} \quad = \quad 2\pi\, n \;=\; (\theta_{Q_b} - \theta_{Q_a}) + (\theta_{Q_a} - \theta_{Q_b}) + 2\pi\, n \tag{4.2.1}$$

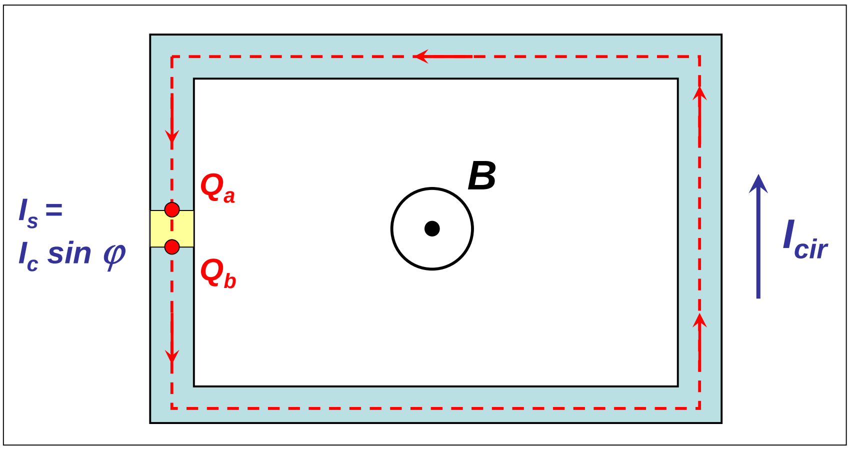

Figure 4.14: The rf-SQUID formed by a single Josephson junction intersecting a superconducting loop. The broken line indicates the closed contour path of the integration.

Using $\nabla\theta = \frac{2\pi}{\Phi_0}(\Lambda \mathbf{J}_s + \mathbf{A})$ (compare (2.2.2)) and $\varphi = \theta_2 - \theta_1 - \frac{2\pi}{\Phi_0}\int_1^2 \mathbf{A}\cdot d\mathbf{l}$ (compare (2.2.3)) we obtain

$$\theta_{Q_b} - \theta_{Q_a} = +\varphi + \frac{2\pi}{\Phi_0}\int_{Q_a}^{Q_b} \mathbf{A}\cdot d\mathbf{l} \tag{4.2.2}$$

$$\theta_{Q_a} - \theta_{Q_b} = \int_{Q_a}^{Q_b} \nabla\theta \cdot d\mathbf{l} = +\frac{2\pi}{\Phi_0}\int_{Q_a}^{Q_b} \Lambda \mathbf{J}_s \cdot d\mathbf{l} + \frac{2\pi}{\Phi_0}\int_{Q_a}^{Q_b} \mathbf{A}\cdot d\mathbf{l} \ . \tag{4.2.3}$$

Substitution these expression into (4.2.1) yields

$$\varphi = -\frac{2\pi}{\Phi_0}\oint_C \mathbf{A}\cdot d\mathbf{l} - \frac{2\pi}{\Phi_0}\int_{Q_a}^{Q_b} \Lambda \mathbf{J}_s \cdot d\mathbf{l} \ . \tag{4.2.4}$$

The integration of **A** around the close contour is equal to the total flux Φ enclosed by the superconducting loop. The integration of $\mathbf{J}_s$ follows the same contour C but excludes the integration over the insulating barrier. Furthermore, if the superconducting loop consists of a superconducting material with a thickness large compared to the London penetration depth λ_L, the integration path can be taken deep inside the superconducting material where the current density is negligible. Therefore, the integral involving the current density can be omitted and we obtain

$$\boxed{\varphi = -\frac{2\pi\Phi}{\Phi_0} \ .} \tag{4.2.5}$$

The phase difference across the junction determines the supercurrent

$$I_s = I_c \sin\left(-\frac{2\pi\Phi}{\Phi_0}\right) = -I_c \sin\frac{2\pi\Phi}{\Phi_0} \ . \tag{4.2.6}$$

The total flux Φ threading the loop is given by the sum of the flux $\Phi_{\rm ext}$ due to an externally applied magnetic field $B_{\rm ext}$ and the flux $LI_{\rm cir}$ due to the circulating current $I_{\rm cir}$. With $I_{\rm cir} = I_s$ we obtain

$$\Phi = \Phi_{\rm ext} + LI_{\rm cir} = \Phi_{\rm ext} - LI_c \sin\frac{2\pi\Phi}{\Phi_0} \ . \tag{4.2.7}$$

Introducing the screening parameter $\beta_{L,\rm rf} = 2\pi LI_c/\Phi_0$ we can rewrite this expression and obtain[54]

$$\boxed{\frac{\Phi}{\Phi_0} = \frac{\Phi_{\rm ext}}{\Phi_0} - \frac{\beta_{L,\rm rf}}{2\pi}\sin\left(2\pi\frac{\Phi}{\Phi_0}\right) \ .} \tag{4.2.8}$$

The variation of Φ with $\Phi_{\rm ext}$ is shown in Fig. 4.15 for two different values of $\beta_{L,\rm rf}$. The regions with positive slope are stable, whereas those with negative slope are not. Regions with negative slope only appear for $\beta_{L,\rm rf} > 1$. Most practical rf-SQUIDs are operated in this regime.

[54]Note that the screening parameter deviates from that defined for the dc SQUID by a factor of π.

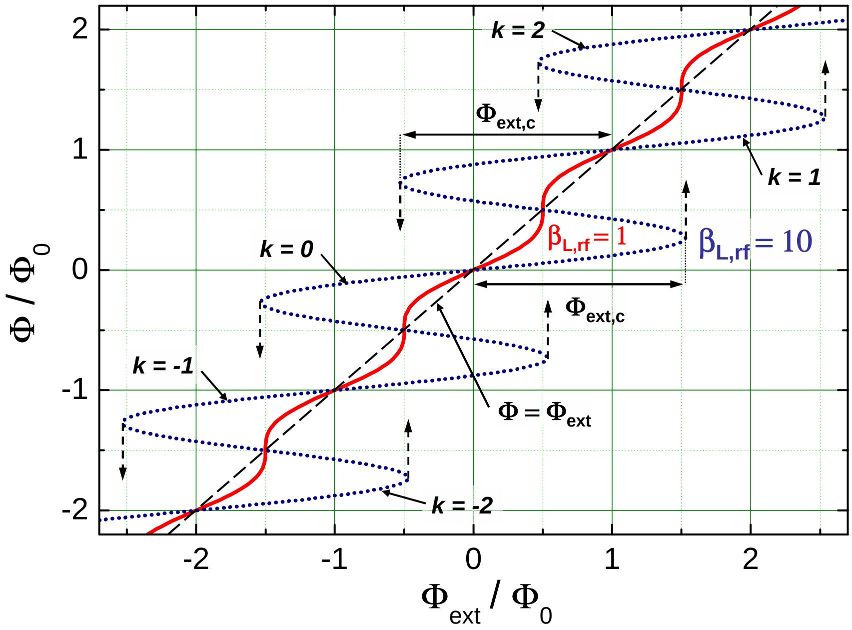

Figure 4.15: Total flux Φ versus applied flux $\Phi_{\rm ext}$ for a rf-SQUID for $\beta_{L,\rm rf} = 1$ (solid line) and 10 (dotted line). The dashed line shows the dependence for $\beta_{L,\rm rf} = 0$.

If we are slowly increasing $\Phi_{\rm ext}$, the total flux Φ increases less rapidly than $\Phi_{\rm ext}$, since the flux due to the shielding current opposes $\Phi_{\rm ext}$. However, when I_s reaches I_c, this shielding behavior cannot be continued, since the critical current of the Josephson junction is reached. Therefore, at a critical value $\Phi_{\rm ext,c}$ the junctions momentarily switches into the voltage state and a flux quantum can penetrate the loop. The SQUID switches from the $k = 0$ to the $k = 1$ quantum state. If we subsequently reduce the applied flux again, the SQUID remains in the $k = 1$ state until $\Phi_{\rm ext} = \Phi_0 - \Phi_{\rm ext,c}$ is reached. At this point I_s again exceeds I_c and the SQUID returns to the $k = 0$ state. That is, in sweeping back and forth the applied flux a hysteresis loop is traced out.

4.2.2 Operation and Performance of rf-SQUIDs

Operation of rf-SQUIDs

As already mentioned the rf-SQUID is operated at radio frequencies. The SQUID loop is inductively coupled to the coil of an LC resonant circuit called tank circuit with a quality factor $Q = R_T/\omega_{\rm rf}L_T$ as shown in Fig. 4.16. Here, $\omega_{\rm rf} = 1/\sqrt{L_T C_T}$ is the resonance frequency of the tank circuit, L_T, C_T and R_T are the inductance, capacitance and the damping resistance of the tank circuit. The mutual inductance between the inductance L of the SQUID loop and L_T of the tank circuit is $M = \alpha\sqrt{L_T L}$. The tank circuit is excited by a rf-current $I_{\rm rf}\sin\omega_{\rm rf}t$, which results in a rf-current $I_T = QI_{\rm rf}$ in the tank circuit. The rf-voltage is amplified by a high impedance preamplifier.

For the case of $\beta_{L,\rm rf} < 1$ the $\Phi(\Phi_{\rm ext})$ curves are non-hysteretic and the rf-SQUID behaves as a nonlinear inductor, which is modifying the resonance frequency $1/\sqrt{L_{\rm T,eff}C_T}$ of the tank circuit periodically with the applied flux. Here, $L_{\rm T,eff}$ is the effective inductance of the tank circuit, which deviates from L_T due to the coupling to the SQUID loop.[55] If the resonant circuit is operated close to its resonance frequency, the

[55]We can write the total flux through L_T as $\Phi_T = L_T I_T - MI_{\rm cir}$, where M is the mutual inductance and $I_{\rm cir}$ the circulating current in the SQUID loop. On the other hand we can write the flux through the SQUID loop as $\Phi = \alpha\Phi_T$, where α is the coupling coefficient between L and L_T. With $\Phi = LI_{\rm cir}$ we obtain $I_{\rm cir} = \alpha\Phi_T/L = \alpha L_T I_T/L$. Then we obtain $\Phi_T =$

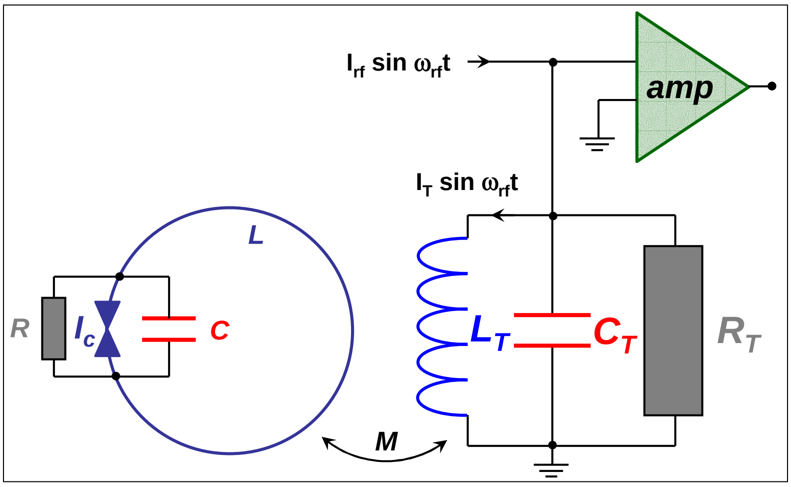

Figure 4.16: The rf-SQUID inductively coupled to the resonant tank circuit.

change of the resonance frequency causes a strong change of the rf-current and hence of the rf-voltage of the tank circuit.

For $\beta_{L,\mathrm{rf}} > 1$, the situation is different, since we have to deal with hysteretic $\Phi(\Phi_{\mathrm{ext}})$ curves. The total applied flux to the SQUID is

$$\Phi_{\mathrm{ext}} \quad = \quad \Phi_s + \Phi_{\mathrm{rf}} \sin \omega_{\mathrm{rf}} t \quad . \tag{4.2.9}$$

It is composed of a low frequency (static) signal flux Φ_s and a rf-flux Φ_{rf} coupled to the SQUID via the tank circuit. Here,

$$\Phi_{\mathrm{rf}} \quad = \quad M \cdot I_T \; = \; M \cdot Q I_{\mathrm{rf}} \tag{4.2.10}$$

is determined by the applied rf-current I_{rf}, the Q factor of the tank circuit and the mutual inductance M. As soon as $\Phi_s + \Phi_{\mathrm{rf}}$ exceeds the critical flux value $\Phi_{\mathrm{ext,c}}$, a hysteresis loop is traced out in the $\Phi(\Phi_{\mathrm{ext}})$ curve. This results in an energy loss proportional to the area of the hysteresis loop and hence in a damping of the tank circuit. It is obvious from Fig. 4.15 that the damping is minimum, if the signal flux is close to $n \cdot \Phi_0$, whereas it is maximum, if the signal flux is close to $\frac{2n+1}{2} \cdot \Phi_0$. This shows that also for the case $\beta_{L,\mathrm{rf}} > 1$ the tank voltage is a periodic function of the applied flux.

In order to discuss how the tank voltage V_T depends on the signal flux Φ_s and the rf-flux Φ_{rf} we discuss the situations $\Phi_s = n\Phi_0$ and $\Phi_s = (n + \frac{1}{2})\Phi_0$. We first consider the case $\Phi_s = n\Phi_0$ with $n = 0$. On increasing I_{rf} the tank voltage V_T initially increases linearly with I_{rf} as long as the resulting rf-flux $\Phi_{\mathrm{rf}} = MQI_{\mathrm{rf}}$ does not exceed the critical value $\Phi_{\mathrm{ext,c}}$. The corresponding critical rf-current is $I_{\mathrm{rf,c}} = \Phi_{\mathrm{ext,c}}/M$ and the tank voltage is

$$V_T^{(0)} \quad = \quad \omega_{\mathrm{rf}} L_T I_{\mathrm{rf,c}} \; = \; \omega_{\mathrm{rf}} L_T \, \frac{\Phi_{\mathrm{ext,c}}}{M} \quad . \tag{4.2.11}$$

Here, the superscript 0 indicates $\Phi_s = n\Phi_0$ with $n = 0$. If we further increase the rf-current resp. rf-flux a jump to the $k = +1$ or $k = -1$ branch of the $\Phi(\Phi_{\mathrm{ext}})$ curve occurs and a hysteresis loop is traced out

$(L_T - \alpha M L_T/L) I_T$. That is, we have the effective inductance $L_{T,\mathrm{eff}} = L_T(1 - \alpha M/L)$. With $M = \alpha\sqrt{L_T L}$ we finally obtain $L_{T,\mathrm{eff}} = L_T(1 - \alpha^2\sqrt{L_T L}/L)$. For $\alpha = 0$ we obtain the obvious result $L_{T,\mathrm{eff}} = L_T$, for $\alpha = 1$ the tank circuit inductance is reduced to the effective value $L_{T,\mathrm{eff}} = L_T(1 - \sqrt{L_T/L})$.

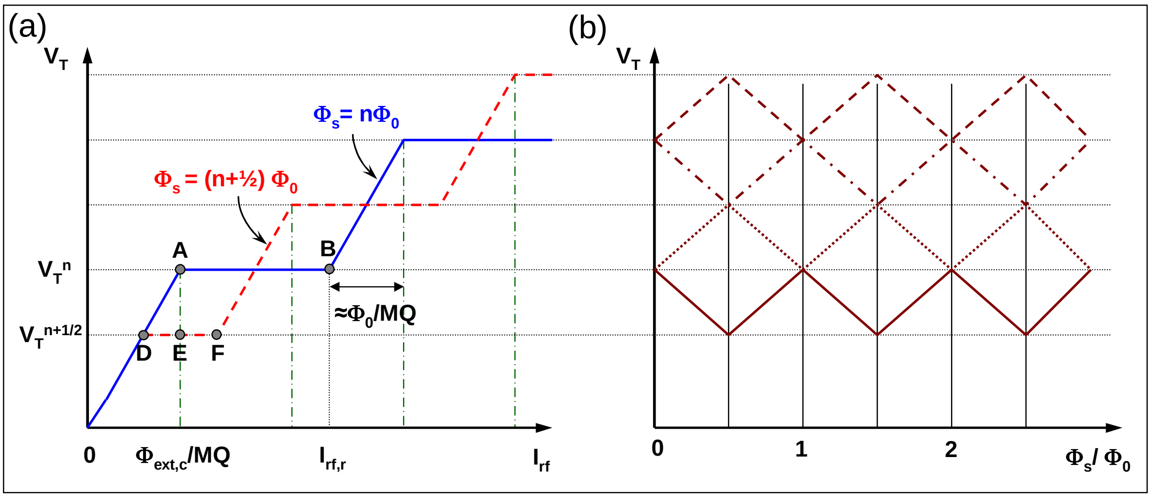

Figure 4.17: (a) Tank voltage V_T plotted versus rf-current $I_{\rm rf}$ for $\Phi_s = n\Phi_0$ and $\Phi_s = (n+\frac{1}{2})\Phi_0$. (b) Tank voltage V_T plotted versus signal flux Φ_s for constant rf-current values marked in (a) by the vertical dash-dotted lines.

(see Fig. 4.15). This is associated with an energy loss ΔE extracted from the tank circuit. Because of this loss, the rf-current amplitude in the tank circuit and, in turn, the rf-flux coupled into the SQUID loop is reduced below $\Phi_{\rm ext,c}$ in the next cycle. That is, no hysteresis loops are traversed until the tank circuit has recovered what usually takes several cycles. A further increase of the rf-current would result in the same jumps to the $k = +1$ or $k = -1$ branches at the same current resp. flux value. That is, the transitions occur at the same rf-current amplitude $I_{\rm rf,c}$ corresponding to the same voltage V_T^0 given by (4.2.11). The only difference is that the tank circuit recovers faster due to the larger $I_{\rm rf}$ and hence the transitions occur at a higher rate. Hence, on increasing $I_{\rm rf}$ the tank voltage stays constant at V_T^0 and we obtain a horizontal branch from point A to B in the $V_T(I_{\rm rf})$ curve (see Fig. 4.17a) The horizontal branch extends until $I_{\rm rf,r}$. At this value the rf-current amplitude is large enough to compensate for the energy loss within a single rf-cycle. Then, a transition is induced in each rf-cycle and the tank voltage V_T increases linearly again until the next critical rf-value is reached, where transitions from the $k = \pm 1$ to the $k = \pm 2$ states become possible. Here, the energy loss increases suddenly, so that the next horizontal branch in the $V_T(I_{\rm rf})$ curve is obtained by the same reason as discussed above.

In order to see how the $V_T(I_{\rm rf})$ curves depend on the signal flux we discuss the case $\Phi_s = (n+\frac{1}{2})\Phi_0$ with $n = 0$. The flux loops traced out during a rf-cycle are now shifted by $\Phi_0/2$. Therefore, during the positive cycle transitions to the $k = +1$ branch occur at the flux $\Phi_{\rm ext,c} - \Phi_0/2$, whereas during the negative cycle transitions occur at $-(\Phi_{\rm ext,c} + \Phi_0/2)$. As a result, when we increase $I_{\rm rf}$ we observe the first horizontal part in the $V_T(I_{\rm rf})$ curve already at

$$V_T^{(1/2)} = \omega_{\rm rf} L_T \frac{\Phi_{\rm ext,c} - \Phi_0/2}{M} \quad . \tag{4.2.12}$$

The horizontal part extends to the rf-current value, which is large enough to compensate for the energy loss within a single rf-cycle. On further increasing $I_{\rm rf}$ we obtain a linear part again until $I_{\rm rf}$ reaches the next critical value corresponding to a peak flux value of $-(\Phi_{\rm ext,c} + \Phi_0/2)$. Then transitions to both the $k = +1$ and $k = -1$ branch are allowed. In total, we observe a series of horizontal branches and linear risers for $\Phi_s = \Phi_0/2$ interlocking those obtained for $\Phi_s = 0$ (see Fig. 4.17a). $V_T(I_{\rm rf})$ curves for intermediate flux values are situated between the two curves obtained for $\Phi_s = \Phi_0/2$ and $\Phi_s = 0$. The $V_T(\Phi_s)$ curves for constant $I_{\rm rf}$ are triangular as shown in Fig. 4.17b.

The change of V_T on increasing the signal flux from 0 to $\Phi_0/2$ is obtained to $\omega_{\rm rf} L_T \Phi_0/2M$ by subtracting (4.2.12) from (4.2.11). Thus, for small flux changes near $\Phi_s = \Phi_0/4$ we find the flux-to-voltage transfer function (compare Fig. 4.17b)

$$H = \left(\frac{\partial V_T}{\partial \Phi_s}\right)_{I_{\rm rf}=const} = \frac{\omega_{\rm rf} L_T}{M} . \qquad (4.2.13)$$

This expression suggests that we can increase H arbitrarily by reducing $M \propto \alpha$. However, then we would completely decouple the SQUID loop from the tank circuit and can no longer perform any measurement. That is, there must be a lower bound for α. The lower bound results from the fact that we must be able to choose a specific value of $I_{\rm rf}$ that intersects the first step of the $V_T(I_{\rm rf})$ curves for all signal flux values. According to Fig. 4.17a, this means that point F has to lie to the right of point E or, equivalently, that $\overline{\rm DF}$ has to exceed $\overline{\rm DE}$. We can estimate $\overline{\rm DF}$ by noting that the power dissipation at D is zero and $E_{J0}\omega_{\rm rf} = I_c\Phi_0\omega_{\rm rf}/2\pi$ at F. This means that $\frac{1}{2}(I_{\rm rf}^F - I_{\rm rf}^E)V_T^{1/2} = I_c\Phi_0\omega_{\rm rf}/2\pi$. Furthermore, from Fig. 4.17a we see that $I_{\rm rf}^E - I_{\rm rf}^D = \Phi_0/2MQ$. Using $LI_c \simeq \Phi_0$ and $V_T^{1/2}$ from (4.2.12) the condition $I_{\rm rf}^E > I_{\rm rf}^D$ can be written as

$$\alpha^2 Q \gtrsim \frac{\pi}{4} . \qquad (4.2.14)$$

If we use the approximation $\alpha^2 \sim 1/Q$ we obtain the transfer function

$$H \approx \frac{\omega_{\rm rf} L_T}{\alpha\sqrt{L_T L}} = \omega_{\rm rf}\sqrt{Q\frac{L_T}{L}} . \qquad (4.2.15)$$

During practical operation of a rf-SQUID one adjusts $I_{\rm rf}$ so that the SQUID stays biased on the first step for all values of Φ_s. The rf-voltage across the tank circuit is amplified and demodulated to produce a signal that is periodic in Φ_s as shown in Fig. 4.17b. Then, in the same way as the dc SQUID a flux locked loop operation is performed by applying a modulating flux at typically 100 kHz and amplitude $\Phi_0/2$. The voltage produced by this modulation is lock-in detected and fed back into the modulation coil to flux-lock the SQUID.

Additional Topic:
Noise in rf-SQUIDs

Noise in the rf-SQUID results from the fact that the switching from the $k=0$ to the $k=1$ state at $\Phi_{\rm ext,c}$ shows stochastic fluctuations due to thermal activation. These fluctuations have two consequences. First, noise is introduced on the step voltage V_T resulting in an equivalent flux noise[56,57]

$$S_\Phi \approx \frac{(LI_c)^2}{\omega_{\rm rf}}\left(\frac{2\pi k_B T}{I_c\Phi_0}\right)^{4/3} . \qquad (4.2.16)$$

Second, the noise causes a finite slope of the horizontal branches of the $V_T(I_{\rm rf})$ curves. **Jackel** and **Buhrman** introduced a slope parameter $\eta = \Delta V_{\rm T,step}/\Delta V_{\rm T,0}$, where $\Delta V_{\rm T,step}$ is the increase of the tank voltage along the length of the step and $\Delta V_{\rm T,0}$ is the voltage separation of two adjacent steps. They showed that η is related to S_Φ by the relation[58]

$$\eta^2 \approx \frac{S_\Phi\omega_{\rm rf}}{\pi\Phi_0^2} . \qquad (4.2.17)$$

[56] J. Kurkijärvi, W.W. Webb, in *Proceedings of the Applied Superconductivity Conference*, Annapolis, Maryland (1972), pp. 581-587.

[57] J. Kurkijärvi, J. Appl. Phys. **44**, 3729 (1973).

[58] L.D. Jackel, R.A. Buhrman, J. Low. Temp. Phys. **19**, 201 (1975).

This relation has been verified in many experiments.

Beyond the intrinsic noise of the rf-SQUID one has to take into account the finite noise temperature $T_{\rm amp}$ of the rf-amplifier. Furthermore, part of the coaxial line connecting the tank circuit to the preamplifier is at room temperature. Since the capacitance of the line and the preamplifier contribute a significant part to the total capacitance of the tank circuit, part of the resistive damping of the tank circuit is well above the operation temperature of the SQUID. This adds additional noise which can be included into the preamplifier noise by assuming an effective noise temperature $T_{\rm amp}^{\rm eff}$. The noise energy by the extrinsic circuit is given by $2\pi\eta k_B T_{\rm amp}^{\rm eff}/\omega_{\rm rf}$.[59] Together with the intrinsic noise (4.2.16) this results in an energy resolution of

$$\boxed{\varepsilon \simeq \left(\frac{\pi\eta^2\Phi_0^2}{2L} + 2\pi\eta k_B T_{\rm amp}^{\rm eff}\right)\frac{1}{\omega_{\rm rf}}\ .} \tag{4.2.18}$$

We see that the energy resolution of the rf-SQUID scales as $1/\omega_{\rm rf}$. Therefore, it is obvious to increase the tank frequency. However, one has to bear in mind that also $T_{\rm amp}$ increases with increasing frequency. The energy resolution of rf-SQUIDs operated at typical frequencies of a few 10 MHz is a few 10^{-29}J/Hz. This sensitivity has been improved by using higher resonance frequencies[60,61] and cold preamplifiers.[62,63] For systems operating at frequencies up to 3 GHz and using high electron mobility transistors energy sensitivities down to 3×10^{-32}J/Hz have been obtained.[64]

Comparing (4.2.18) to (4.1.48) we see that the intrinsic energy resolution of the rf-SQUID can be roughly approximated by $\varepsilon \sim k_B T/\omega_{\rm rf}$, whereas that of the dc SQUID is roughly $\varepsilon = k_B T/\omega_c$. Here, $\omega_c = 2\pi I_c R_N/\Phi_0$ is the characteristic frequency, which typically ranges in the 100 GHz regime. This shows that the better intrinsic energy resolution of the dc SQUID is mainly related to the fact that $\omega_c \gg \omega_{\rm rf}$.

4.2.3 Practical rf-SQUIDs

Low T$_c$ rf-SQUIDs

RF-SQUIDs based on metallic low temperature superconductors are commercially available since the early 1970s (notably from Biomagnetic Technologies (BTi) – formerly S.H.E. Corporation, Quantum Design, and Tristan Technologies Inc.). The early rf-SQUIDs had a toroidal configuration machined from Nb. These devices are operated at a few 10 MHz and typically have a white noise energy of 5×10^{-29}J/Hz and a $1/f$ noise of roughly 10^{-28}J/Hz at 0.1 Hz. Today rf-SQUIDs are fabricated in the same way as dc-SQUIDs using thin film technology. Energy sensitivities down to a few 10^{-32}J/Hz have been achieved in the white noise regime.

High T$_c$ rf-SQUIDs

After the discovery of the high temperature superconductors rf-SQUIDs based on the cuprate superconductors have been developed operating at 77 K. In order to increase the operation frequency conventional

[59] R.P. Giffard, J.C. Gallop, B.N. Petley, Prog. Quantum Electr. **4**, 301 (1976).
[60] A. Long, T.D. Clark, R.J. Prance, M.G. Richards, Rev. Sci. Instrum. **50**, 1376 (1979).
[61] J.N. Hollenhorst, R.P. Giffard, IEEE Trans. Magn. **15**, 474 (1979).
[62] H. Ahola, G.H. Ehnholm, B. Rantala, P. Ostman, J. Low. Temp. Phys. **35**, 313 (1979).
[63] M. Mück, Th. Becker, Ch. Heiden, Appl. Phys. Lett. **66**, 376 (1995).
[64] J. Clarke, IEEE Trans. Electron. Devices **27**, 1896 (1980).

washer-type rf-SQUIDs have been incorporated into a superconducting $\lambda/2$ microstrip resonator, which serves as the tank circuit (see Fig. 4.18).[65,66] In this way a flux noise level of $10\,\mu\Phi_0/\sqrt{\mathrm{Hz}}$ could be obtained for a 50 pH rf SQUID operated at 150 MHz. This noise was found to be independent of frequency down to 1 Hz.

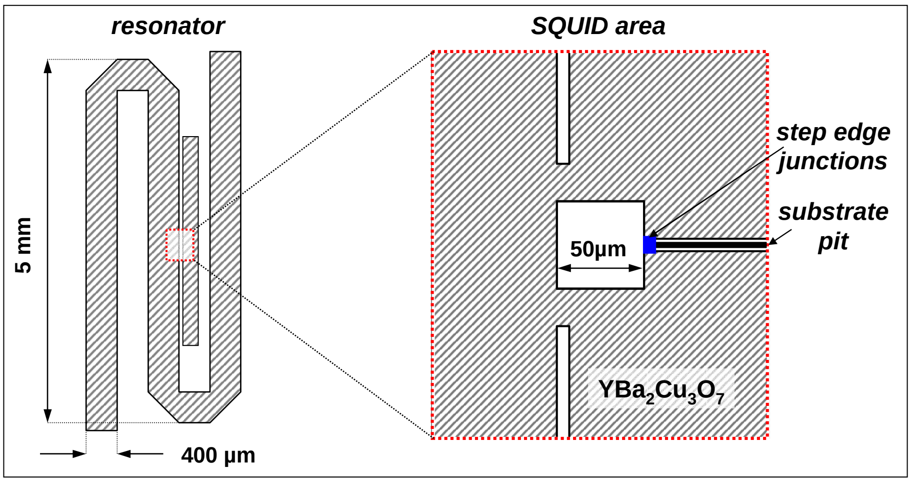

Figure 4.18: Schematic drawing of a high-T_c rf-SQUID integrated into a $\lambda/2$ resonator. The right hand side shows a magnified view of the SQUID area (after Y. Zhang, M. Mück, A.I. Braginski, H. Töpfer, Supercond. Sci. Technol. **77**, 269 (1994)).

[65] Y. Zhang, M. Mück, A.I. Braginski, H. Töpfer, Supercond. Sci. Technol. **77**, 269 (1994).

[66] A.I. Braginski, in *SQUID Sensors: Fundamentals, Fabrication and Applications*, H. Weinstock ed., NATO Science Series E: Applied Sciences, Vol. 329, Kluwer Academic Publishers, Dordrecht, Boston, London (1996).

4.3 Additional Topic: Other SQUID Configurations

Over the years many other SQUID configurations besides the dc- and rf-SQUID have been developed. A few of them are briefly addressed in the following.

4.3.1 The DROS

To simplify the readout electronics of SQUIDs, the flux-to-voltage transfer coefficient should be large enough such that direct readout of the SQUID output voltage by standard room-temperature preamplifiers is possible. Compared with the standard dc SQUIDs, the ***Double Relaxation Oscillation SQUID*** (DROS) provides very large flux-to-voltage transfer and large modulation voltage, and thus simple flux-locked loop electronics can be used for SQUID operation.[67,68,69]

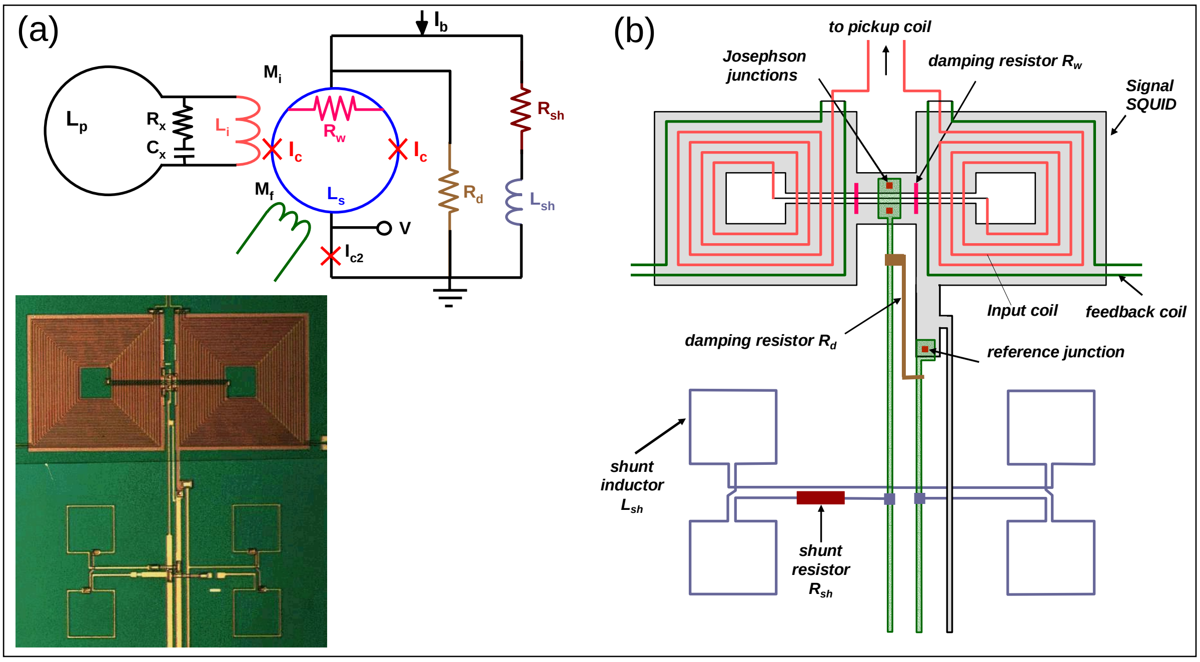

Figure 4.19: (a) Schematic circuit drawing of a double relaxation oscillation SQUID sensor and (b) close-up view of the DROS. I_b is the bias current, $2I_c$ is the critical current of the signal SQUID, L_s is the inductance of the signal SQUID, $R_{\rm sh}$ and $L_{\rm sh}$ are the resistance and inductance of the relaxation circuit, respectively, R_d and R_w are damping resistors, M_i and M_f are the mutual inductances between the SQUID and the input coil L_i and the feedback coil, respectively, R_x and C_x are used to damp the input coil resonance. The output voltage V is measured across the reference junction I_{c2}. Also shown is an optical micrograph of the SQUID sensor (after Y. H. Lee, J. M. Kim, H. C. Kwon, Y. K. Park, J. C. Park, D. H. Lee, and C. B. Ahn, Progress in Supercond. **Vol. 2**, 20-26 (2000)).

The DROS consists of a hysteretic ($\beta_C > 1$) dc SQUID (the signal SQUID) and a hysteretic junction (the reference junction), shunted by a relaxation circuit of an inductor and a resistor. In this way the system

[67] D. J. Adelerhof, H. Nijstad, F. Flokstra and H. Rogalla, *(Double) relaxation oscillation SQUIDs with high flux-to-voltage transfer: Simulations and experiments*, J. Appl. Phys. **76**, 3875-3886 (1994).

[68] M.J. van Duuren, Y.H. Lee, D.J. Adelerhof, J. Kawai, H. Kado, J. Flokstra, H. Rogalla, IEEE Trans. Appl. Supercond. **AS-6**, 38-44 (1996).

[69] D. Drung, *Advanced SQUID readout electronics*, in *SQUID Sensors: Fundamentals, Fabrication and Application*, H. Weinstock ed., Dordrecht, Kluwer Academic Publishers (1996), pp. 63-116.

performs relaxation oscillations (cf. section 4.1.5). Instead of the reference junction also a reference SQUID can be used. However, the reference junction has the advantage to be less susceptible for flux trapping than the reference SQUID and to eliminate the lines needed for the adjustment of a reference flux.

The schematic circuit drawing of the DROS planar gradiometer and the close-up view of the DROS are shown in Fig. 4.19a and b, respectively. In an adequate bias current range, the DROS functions as a comparator of the two critical currents, namely the signal critical current and the reference critical current. Thus, the voltage output of the DROS behaves like a square-wave function as the signal flux changes, resulting in a very large flux-to-voltage transfer coefficient when the two critical currents are equal.

As an example, in Fig. 4.19b a gradiometer-type signal SQUID is shown with two square-shaped washers connected in parallel. A reference junction is used instead of the reference SQUID. The high flux-to-voltage transfer coefficient of typically $3\,\mathrm{mV}/\Phi_0$ enables direct readout by simple room temperature electronics with a modest voltage noise. By integrating a pickup coil consisting of two planar coils (typical size: $10 \times 10\,\mathrm{mm}^2$, baseline length: a few cm) connected in series on the same chip a planar gradiometer with a field gradient noise of a few fT/cm Hz in the white noise regime can be obtained.

4.3.2 The SQIF

For the realization of SQUIDs also interferometer structures consisting of more than two junctions can be used. As we have seen, for $\beta_L \ll 1$ the dependence of the maximum Josephson current of a dc SQUID on the external flux corresponds to the diffraction pattern of a double slit configuration. In analogy to optics it is evident that we can achieve an even steeper $I_s^m(\Phi_{\mathrm{ext}})$ dependence by using a structure corresponding to an optical grid. Such a structure is obtained by putting N junctions in parallel. The problem in the realization of such structures is the requirement to fabricate a large number of identical Josephson junctions and loops separating them. If the junction and loop parameters vary considerably, the resulting interference pattern is very irregular and hardly useful. However, recently it was pointed out that also irregular configurations are useful. Such arrays have been named ***Superconducting Quantum Interference Filters*** (SQIFs).

By using an irregular parallel array of Josephson junctions as shown in Fig. 4.20a, the resulting interference pattern, i.e. the $I_s^m(\Phi_{\mathrm{ext}})$ dependence of the array shows a sharp peak at zero flux followed by a very steep decrease. A similar result is obtained for the array voltage $V(\Phi_{\mathrm{ext}})$ at constant bias current (see Fig. 4.20b). The idea then is to use the peak in the maximum Josephson current to realize a sensitive flux sensor. Typically, a SQIF device consists of a parallel array of several 10 Josephson junctions. Devices with both low-T_c and high-T_c Josephson junctions have been realized.[70,71] Compared to dc SQUIDs the SQIF shows a considerably higher flux-to-voltage transfer coefficient. Beyond irregular parallel arrays also series configurations of dc SQUIDs with varying loop size and two-dimensional structures have been studied.[72]

4.3.3 Cartwheel SQUID

In so-called cartwheel SQUIDs the SQUID loop consists of several loops forming a cartwheel. The loops are parallel to each other thereby reducing the total inductance of the SQUID loop. Cartwheel SQUIDs

[70] J. Oppenländer, Ch. Häussler, T. Träuble, N. Schopohl, Physica **C 368**, 119 (2002).

[71] V. Schultze, R.I. Ijsselstein, H.-G. Meyer, J. Oppenländer, Ch. Häussler, N. Schopohl, IEEE Trans. Appl. Supercond. **AS-13**, 775 (2003).

[72] J. Oppenländer, P. Caputo, Ch. Häussler, T. Träuble, J. Tomes, A. Friesch, N. Schopohl, Appl. Phys. Lett. **83**, 969 (2003); IEEE Trans. Appl. Supercond. **AS-13**, 771 (2003).

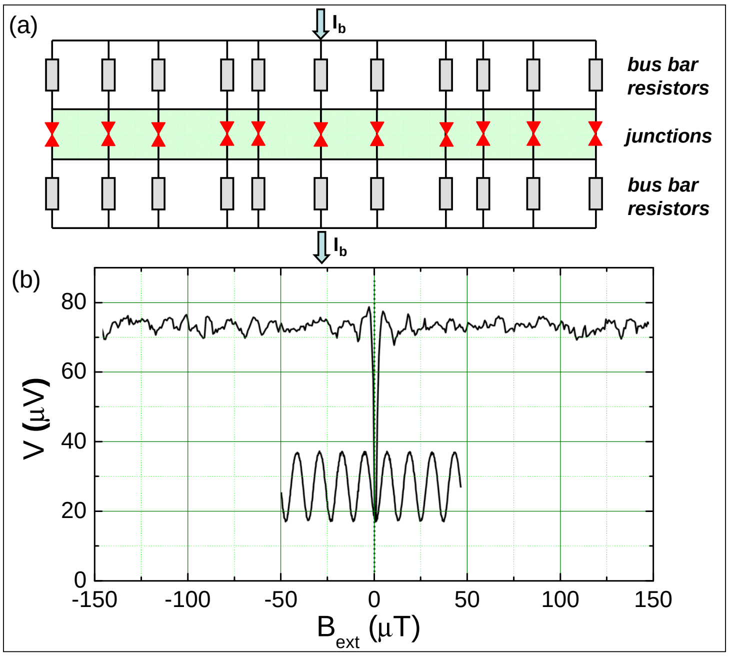

Figure 4.20: (a) Schematic diagram of a parallel Superconducting Quantum Interference Filter (SQIF) circuit. The different array loops have different areas. The bias current I_b is fed into the array through bus bar resistors. (b) Voltage response of a parallel SQIF plotted vs. the magnetic applied field B_{ext} (upper curve). The lower curve shows a part of the voltage response of a conventional two junction SQUID (after J. Oppenländer, Ch. Häussler, T. Träuble, N. Schopohl, Physica **C 368**, 119 (2002)).

have been fabricated both from low-T_c and high-T_c materials. With a high-T_c version field sensitivities down to 18 fT/$\sqrt{\mathrm{Hz}}$ have been achieved in the white noise regime.[73] A more detailed description of the cartwheel SQUID is given in section 4.4.1 in our discussion of SQUID magnetometers (see also Fig. 4.22d and e).

[73] F. Ludwig, E. Dansker, R. Kleiner, D. Kölle, J. Clarke, S. Knappe, D. Drung, H. Koch, N. Alford, T.W. Button, Appl. Phys. Lett. **66**, 1418-1420 (1995).

4.4 Instruments Based on SQUIDs

In principle, a SQUID can sense any kind of signal that can be converted into a flux coupled into the SQUID loop. Therefore, both dc- and rf-SQUIDs are used as sensors in a broad assortment of instruments. In the following we briefly discuss some of them. Each SQUID instrument involves a specific antenna attached to the input of the SQUID. This antenna determines the quantity that is measured by the SQUID as shown in Fig. 4.21.

In using the SQUID in different applications involving different antenna at the input we should recognize that the presence of an input circuit influences both the signal and the noise properties of the SQUID. On the other hand, the SQUID reflects a complex impedance into the input. Furthermore, the SQUID represents a nonlinear device. Therefore, a full description of the interactions is complicated and we will not go into the details here. We only will concentrate on one important aspect that already was recognized in 1971 by **J.E. Zimmerman**.[74] Suppose we are connecting a pick-up loop of inductance L_p to the input coil of the SQUID with inductance L_i to form a magnetometer as shown in Fig. 4.21. It can be shown that the SQUID inductance L is thereby reduced to the value

$$L' = L - \frac{M^2}{L_i + L_p} = L\left(1 - \frac{\alpha^2 L_i}{L_i + L_p}\right) , \qquad (4.4.1)$$

where α^2 is the coupling coefficient between L and L_i, which determines the mutual inductance $M_i = \alpha\sqrt{L_i L}$ between L and L_i. Here, we have neglected any stray inductances in the leads connecting L_i and L_p. The reduction in L tends to increase the transfer function ($H \sim R_N/L$ for the dc-SQUID) of the SQUID.

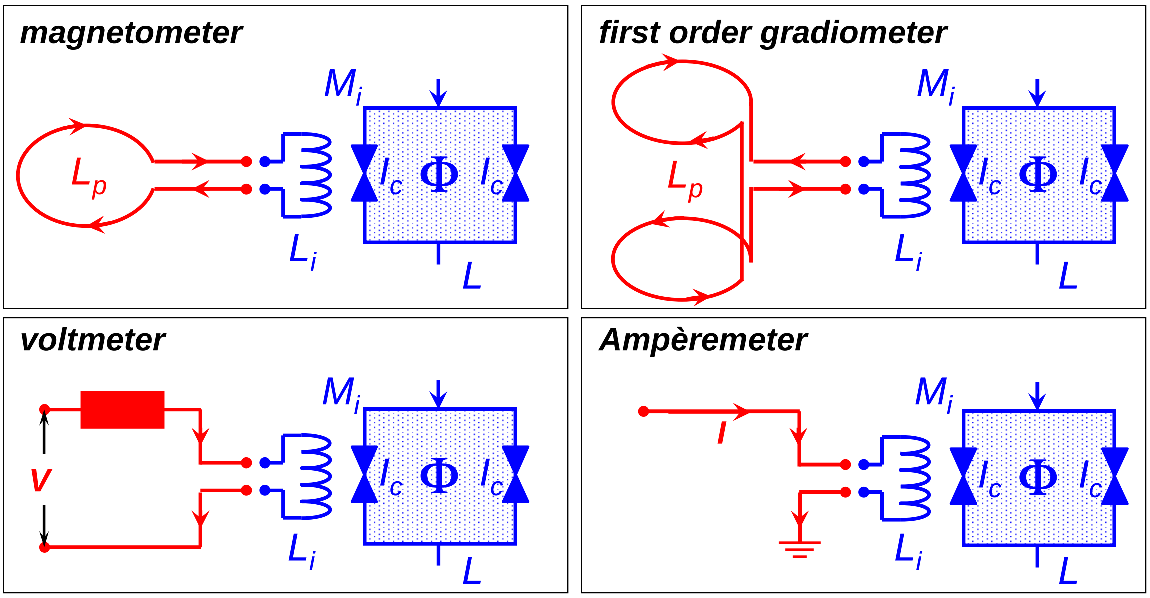

Figure 4.21: Different types of input antenna for superconducting quantum interference devices used in different applications. The input antenna converts the quantity to be measured into magnetic flux.

[74] J.E. Zimmerman, *Sensitivity enhancement of SQUIDs through the use of fractional turn loops*, J. Appl. Phys. **42**, 4483 (1971).

4.4.1 Magnetometers

The probably most simple and straightforward SQUID instrument is the SQUID magnetometer. Here, a pick-up loop with inductance L_p is connected to the input coil of the SQUID forming a superconducting flux transformer. That is, a small flux change $\delta\Phi^p = N_p A_p \delta B_{\rm ext}$ applied to the pick-up loop is causing a shielding current $I_{\rm sh}$ flowing through both the pick-up and the input coil. Here, A_p and N_p are the area and turn number of the pick-up loop. The current through the input coil generates a magnetic flux that is coupled into the SQUID loop. Flux quantization requires that

$$\delta\Phi^p + (L_i + L_p) I_{\rm sh} = N_p A_p \delta B_{\rm ext} + (L_i + L_p) I_{\rm sh} = 0 \ . \tag{4.4.2}$$

We have neglected the effects of the SQUID on the input circuit. The flux coupled into the SQUID operated in the flux locked loop is

$$\delta\Phi = M_i |I_{\rm sh}| = M_i \frac{\delta\Phi^p}{L_i + L_p} = \frac{\alpha\sqrt{L_i L}}{L_i + L_p}\,\delta\Phi^p = \frac{\alpha\sqrt{L_i L}}{L_i + L_p} N_p A_p \delta B_{\rm ext} \ , \tag{4.4.3}$$

where $M_i = \alpha\sqrt{L_i L}$ is the mutual inductance between L_i and L.

In order to find the minimum detectable value of $\delta\Phi^p$, we equate $\delta\Phi$ to the equivalent flux noise of the SQUID. Defining S_Φ^p as the spectral density of the flux noise referred to the pick-up loop, we find

$$S_\Phi^p = \frac{(L_i + L_p)^2}{M_i^2} S_\Phi = \frac{(L_i + L_p)^2}{\alpha^2 L_i L} S_\Phi \ . \tag{4.4.4}$$

Introducing the equivalent noise energy referred to the pick-up loop, we obtain

$$\varepsilon^p = \frac{S_\Phi^p}{2L_p} = \frac{(L_i + L_p)^2}{L_i L_p} \frac{S_\Phi}{2\alpha^2 L} = \frac{(L_i + L_p)^2}{L_i L_p} \frac{\varepsilon}{\alpha^2} \ . \tag{4.4.5}$$

Analyzing (4.4.5) we see that it has the minimum value

$$\varepsilon^p(f) = \frac{4\varepsilon(f)}{\alpha^2} \tag{4.4.6}$$

for $L_i = L_p$. Thus, a maximum fraction $\alpha^2/4$ of the energy in the pick-up loop is transferred to the SQUID, if we match L_p and L_i. Here, we have neglected the noise currents in the input circuit and the fact that the input circuit reduces the SQUID inductance.

With the optimum flux resolution for $L_p = L_i$ we can give the corresponding magnetic field resolution $S_B^p(f) = S_\Phi^p(f)/(\pi r_p^2)^2$, where r_p is the radius of the pick-up loop. With $S_\Phi^p = 8\varepsilon L_p/\alpha^2$ we obtain

$$S_B^p(f) = \frac{8L_p}{\alpha^2(\pi r_p^2)^2}\,\varepsilon(f) \ . \tag{4.4.7}$$

The inductance of the superconducting pick-up coil made from a wire with radius r_0 is given by $L_p = \mu_0 r_p[\ln(8r_p/r_0) - 2]$ and can be approximated by $L_p \simeq 5\mu_0 r_p$ over a wide range of values r_p/r_0. Therefore, we obtain $S_B^p(f) \approx 4\mu_0\varepsilon/\alpha^2 r_p^3 \propto 1/A_p^{3/2}$. This shows that we can increase the magnetic field resolution by increasing the radius of the pick-up loop while keeping $L_p = L_i$. In practice, of course there is a limitation due to the finite size of the cryostat used for cooling down the system. Furthermore, a spatially varying signal is averaged over the area of the pick-up loop. Taking $\varepsilon \simeq 10^{-28}$J/Hz, $\alpha = 1$ and $r_p = 25$ mm, we calculate $\sqrt{S_B^p} \simeq 5\times10^{-15}$T/$\sqrt{\rm Hz}$. This is a much better value than that achieved with non-superconducting magnetometers.

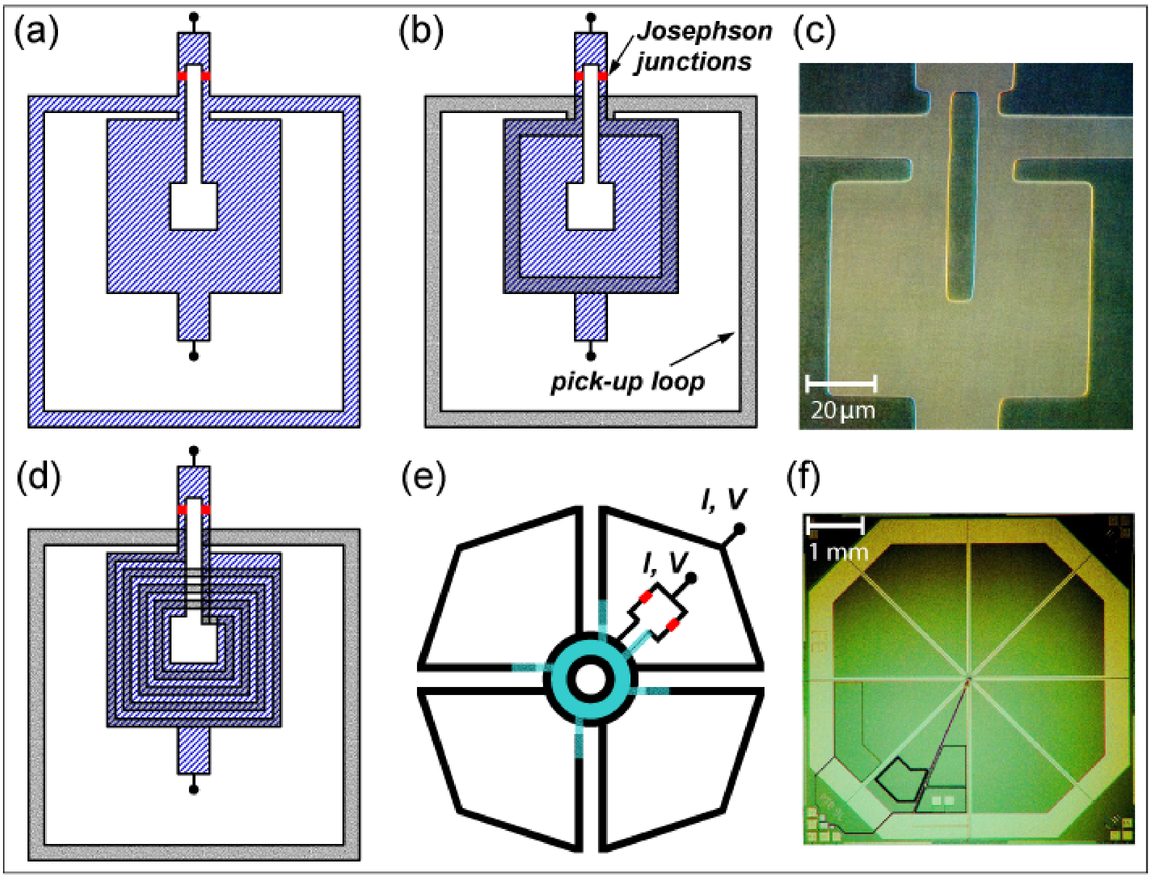

Figure 4.22: Various types of thin film SQUID magnetometers: (a) directly coupled SQUID magnetometer (single layer structure), (b) flip-chip magnetometer with single-turn input coil, (c) optical micrograph of a directly coupled YBCO grain boundary junction dc SQUID (by courtesy of D. Kölle), (d) flip-chip magnetometer with multi-turn input coil, (e) multi-loop magnetometer (the inner part consists of a trilayer structure), and (f) optical micrograph of a 8-loop Nb SQUID magnetometer (by courtesy of PTB Braunschweig).

Thin Film Magnetometers

SQUIDs operated at 4.2 K or below can make use of wire wound flux transformers. The wire wound flux transformer is then connected to the planar multi-turn thin film input coil positioned on top of the SQUID washer. Note that the contact between the input coil and the flux transformer must be superconducting. Unfortunately, for high temperature superconductors there exists no highly flexible superconducting wire that could be connected via a superconducting contact to the input coil. Therefore, no wire-wound flux transformers can be used und thin film flux transformers have to be applied. A solution to the problem is the directly coupled SQUID (see Fig. 4.22a).[75,76] It consists of a large pick-up loop of inductance L_p and area A_p directly connected to the SQUID body of inductance $L \ll L_p$. A magnetic field $B_{\rm ext}$ applied to the pickup loop induces a screening current $I_{\rm sh} = B_{\rm ext}A_p/L_p$, which in turn links a flux $(L - L_J)I_{\rm sh}$ to the SQUID. Here, L_J is the parasitic inductance of the striplines incorporating the junctions, to which the current does not couple. The effective area is $A_{\rm eff} = (L - L_J)A_p/L_p \pm A_s$, where $A_s \ll A_{\rm eff}$ is the effective area of the bare SQUID and the sign of A_s depends on the relative senses of the SQUID and the pickup loop. We note that the direct coupling of the flux transformer and the SQUID body can be avoided by coupling the SQUID loop in a flip-chip arrangement to a single-layer flux transformer (see Fig. 4.22b)

[75]M. Matsuda, Y. Murayama, S. Kiryu, N. Kasai, S. Kashiwaya, M. Koyanagi, and T. Endo, IEEE Trans. Magn. **MAG-27**, 3043 (1991).
[76]D. Koelle, A. H. Miklich, F. Ludwig, E. Dantsker, D. T. Nemeth, and J. Clarke, Appl. Phys. Lett. **63**, 2271 (1993).

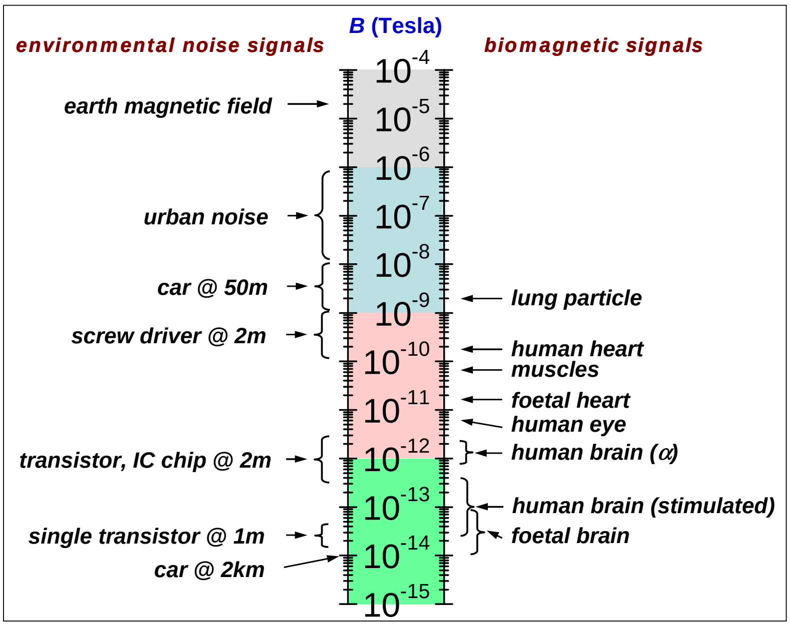

Figure 4.23: Signal strength of some magnetic noise signals compared to that of biomagnetic signals.

fabricated on a separate substrate.[77]

A general problem of using single turn flux transformers as shown in Fig. 4.22a and b is the bad coupling due to $N_p = N_i = 1$. In order to improve the situation, multi-turn input coils have been used (see Fig. 4.22c). The fabrication of such structures, however, already requires multi-layer thin film technology, which is complicated for the high temperature superconductors due to the requirement of heteroepitaxial growth.

A completely different concept for achieving large effective areas is the multi-loop magnetometer (see Fig. 4.22e). It was originally proposed and demonstrated by **J.E. Zimmerman** in 1971.[78] The essential idea is to connect N loops in parallel, thus reducing the total inductance to a level acceptable for a SQUID, while keeping the effective area large. In the thin-film multiloop magnetometer, shown schematically in Fig. 4.22d, N loops are connected in parallel with the connection made at the center via coplanar lines. The two Josephson junctions connect the upper and lower superconducting films of the central trilayer structure. Today sensitive multiloop SQUID magnetometers are fabricated using niobium thin-film technology. For example, with eight parallel loops and a diameter of 7.2 mm these devices have a typical magnetic field sensitivity of $1.5\,\mathrm{fT}/\sqrt{\mathrm{Hz}}$ down to a few Hz at 4.2 K.[79] These devices have been used successfully for multichannel biomagnetic studies.[80,81]

4.4.2 Gradiometers

Since SQUIDs are very sensitive magnetic field sensors, they are susceptible to all kind of perturbing magnetic field fluctuations caused by the environment. Fig. 4.23 shows a collection of perturbing signals compared to interesting biomagnetic signals. For example, a screw driver placed about 5 m from

[77] D. Koelle, A. H. Miklich, E. Dantsker, F. Ludwig, D. T. Nemeth, J. Clarke, W. Ruby, and K. Char, Appl. Phys. Lett. **63**, 3630 (1993).
[78] J.E. Zimmerman, J. Appl. Phys. **42**, 4483 (1071).
[79] D. Drung, in *SQUID Sensors: Fundamentals, Fabrication and Applications*, NATO ASI Series, edited by H. Weinstock (Kluwer Academic, Dordrecht), p. 63 (1996).
[80] D. Drung, R. Cantor, M. Peters, H.-J. Scheer, and H. Koch, Appl. Phys. Lett. **57**, 406 (1990).
[81] D. Drung, S. Knappe, and H. Koch, IEEE Trans. Appl. Supercond. **3**, 2019 (1995).

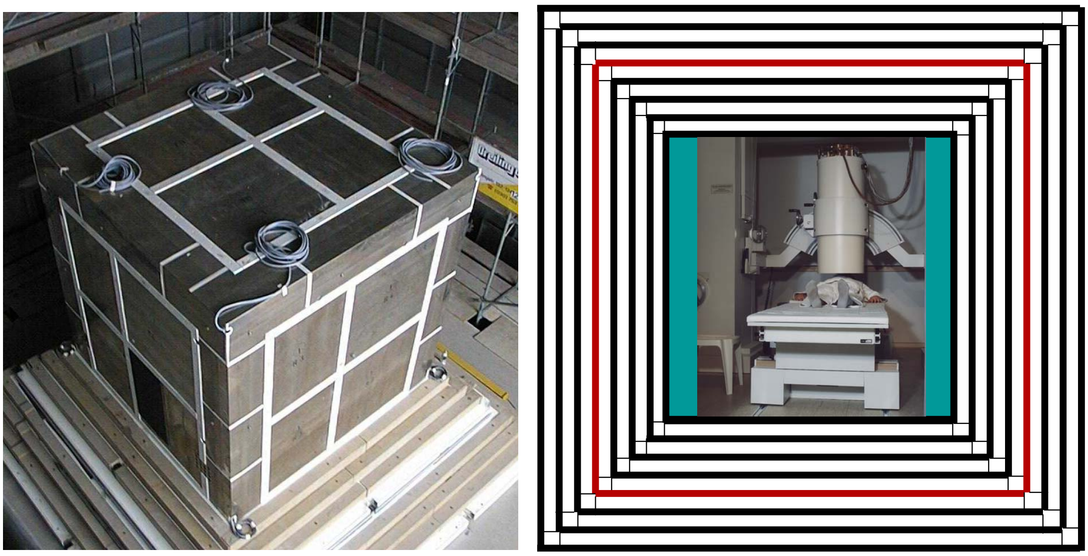

Figure 4.24: Magnetically shielded room at the PTB in Berlin. Left: Photograph of the shielded room with a diameter of 2.9 m. Right: Cross-sectional view showing the seven μ-metal and the single Al layer as well as a photograph of the multi-channel SQUID system positioned inside the room (by courtesy of PTB Berlin).

the SQUID sensor is generating a magnetic field strength above the signal originating from our heart activity. Signals originating from our brain activity are even much smaller. They are of the same order of magnitude as those of a car passing at a distance of about 2 km.

In order to do biomagnetic measurements one has to reduce the perturbing magnetic fields of the environment. First of all, the SQUID set-up has to be made from non-magnetic materials. Furthermore, one can use μ-metal shields to reduce static and low-frequency perturbing magnetic fields by about three to four orders of magnitude. A convenient but expensive way is the use of magnetically shielded rooms. One of the most effective magnetically shielded rooms is presently used by the PTB in Berlin (see Fig. 4.24). The walls of the room consist of 7 μ-metal shields and an additional Al-layer for shielding of high-frequency electromagnetic fields. In addition, an active magnetic field reduction is used. In this way a shielding factor of 2×10^6 and 2×10^8 is achieved at a frequency of 0.01 and 5 Hz, respectively.

In many situations magnetic shielding is too expensive or one simply cannot shield perturbing signals. This is for example the case, when one is interested in the measurement of brain signals, which are superimposed by the much stronger heart signals (compare Fig. 4.23). In this case the use of gradiometers is useful. Ideal gradiometers of n^{th} order are susceptible only to gradients of n^{th} and higher order. Since signals of remote sources appear almost constant at the sensor position, they are strongly suppressed by gradiometers. For example, the signals generated by the heart are almost constant at a sensor placed on the head of a person for the measurement of the brain signals. Therefore, the heart signals are strongly suppressed by the use of gradiometers. In contrast, the brain signals are very close to the sensor and have strong gradients.

Figs. 4.25a and b show a few axial gradiometer configurations, which can be realized by winding a superconducting wire on a suitable support structure. Such gradiometers are widely used in SQUID sensors applied in magneto encephalography. For a first order gradiometer a constant magnetic field is generating shielding currents flowing in opposite directions in the two coils. Hence, there is no net flux and no net shielding current flowing to the SQUID input coil. In contrast, for a gradient $dB_z/dz \neq 0$ the shielding currents in the two sub-coils are different. Hence there is a net flux and shielding current. In the same way, for a second order gradiometer, a constant field gradient is causing no net flux and shielding current. For a third order gradiometer this is the case for a second order gradient and so on.

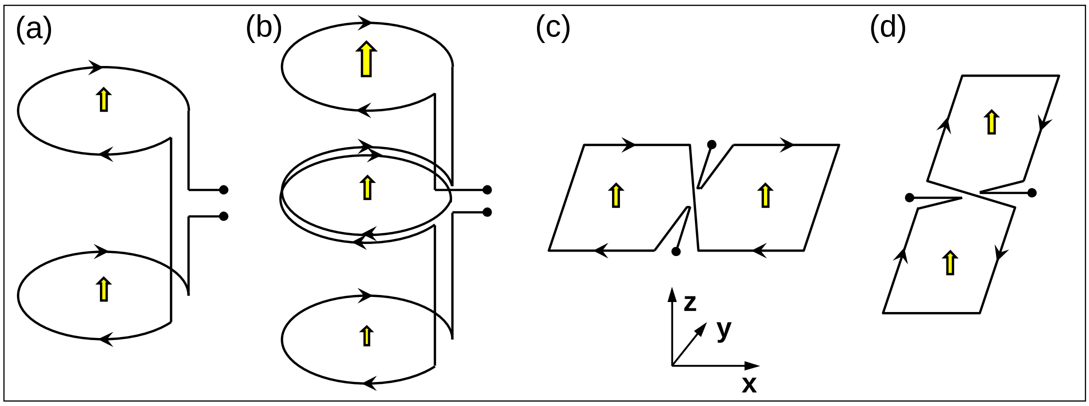

Figure 4.25: (a) First and (b) second order axial gradiometer detecting dB_z/dz and d^2B_z/dz^2. (c) and (d) show planar first order gradiometers for dB_z/dx and dB_z/dy. The big arrows mark the direction of the magnetic field, the small arrows that of the shielding currents.

Beyond axial gradiometers one also can design various planar gradiometers. For example, a first order planar gradiometer has the shape of a "8". If the axis of the "8" is along the y-direction and the direction perpendicular to it is the z-direction, the gradiometer is measuring the gradient dB_z/dy. In the same way gradiometers for other gradients can be constructed.[82] We also note that beyond the so-called hardware gradiometers shown in Fig. 4.25 also software gradiometers can be used. Here, for example the signals of two magnetometers can be combined to realize a first order gradiometer by means of a suitable software. By combining a larger number of magnetometers or low-order gradiometers various higher order gradiometers can be realized.

4.4.3 Susceptometers

SQUID susceptometers are used today in many laboratories for measuring the magnetic properties of materials. The susceptibility can be measured by a first order gradiometer as shown in Fig. 4.25a. The sample to be studied and the gradiometer are brought into a static homogeneous magnetic field. The sample is positioned in one of the pick-up loops of the gradiometer. If the sample would be non-magnetic, there would be no output signal from the gradiometer provided that the magnetic field is perfectly homogeneous and the gradiometer perfectly balanced. However, for a magnetic sample with a nonvanishing susceptibility χ an additional flux is generated in one of the pick-up loops of the gradiometer. This results in a finite shielding current that is coupling flux to the SQUID via the SQUID input coil connected to the gradiometer.

Today sophisticated SQUID susceptometers are commercially available.[83] In these systems usually the sample is moved along an axial second order gradiometer. The resulting signal is measured as a function of the position and fitted to a theoretically expected curve. These susceptometers allow to measure the susceptibility in the temperature range between 1.8 and 400 K in fields up to 7 T at a resolution of about 10^{-8}emu.

For even more sensitive measurements of very small samples one can use miniature SQUID susceptome-

[82]Note that for the measurement of the gradients dB_z/dz, dB_y/dy and dB_x/dx three-dimensional gradiometer configurations are required, whereas the other gradients can be measured by planar configurations.

[83]For example: Magnetic Property Measurement System (MPMS), Quantum Design, 6325 Lusk Boulevard, San Diego, CA 92121-3733, USA.

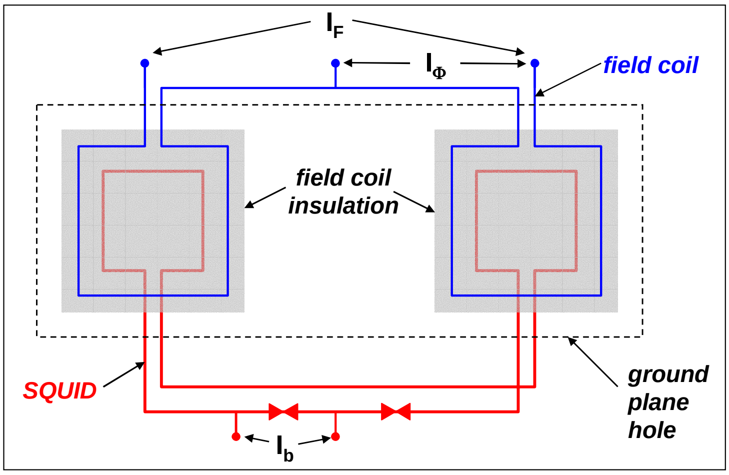

Figure 4.26: Thin film miniature SQUID susceptometer. The SQUID consisting of two series connected pick-up loops wound in opposite sense are placed on a superconducting ground plane to minimized the inductance due to the connecting lines. The hole in the ground plane is indicated by the dashed line.

ters, which have been pioneered by **Ketchen** and coworkers.[84,85,86] An example for a miniature SQUID susceptometer is shown in Fig. 4.26. The SQUID loop is formed by two pick-up loops that are wound in opposite sense and connected in series. The pick-up loops are deposited on a superconducting ground plane in order to minimize the inductance of the whole device. The SQUID is flux biased at the position of maximum transfer function H by applying a control current I_Φ to one of the pick-up loops. Furthermore, a magnetic field can be applied to both loops via the field current I_F. By passing part of this current into the center connector one can obtain a high degree of balance between the two loops. The sample to be measured is placed over one of the loops. The output of the SQUID, when the field is applied, is then proportional to the magnetization of the sample. The sensitivity of the miniature SQUID susceptometer is impressive. It is capable of detecting the magnetization of about 3000 electron spins.

4.4.4 Voltmeters

As shown in Fig. 4.21 a SQUID can be used for the detection of small voltages. The voltage to be measured is transformed to a current via an input resistor. The current flowing into the input coil is coupling flux to the SQUID loop, which generates an output signal that is proportional to the voltage at the input. The use of SQUIDs as sensitive voltmeters was proposed by **J. Clarke** already in 1966.[87] In practical voltmeters the SQUID voltage output signal from the flux-locked loop is fed back to the known input resistor to realize a null-balancing measurement of the voltage. The resolution of the SQUID voltmeter is limited by the Nyquist noise in the input circuit, which varies from about $10^{-12}\mathrm{V}/\sqrt{\mathrm{Hz}}$ for an input resistance of $0.01\,\Omega$ to about $10^{-10}\mathrm{V}/\sqrt{\mathrm{Hz}}$ for $100\,\Omega$. That is, SQUID voltmeters are superior to semiconductor amplifiers, which have a typical voltage input noise of several $10^{-10}\mathrm{V}/\sqrt{\mathrm{Hz}}$ for low impedance samples. Typical applications are the measurement of thermoelectric voltages, the measurement of the transport properties of low resistance metallic nanostructures, the study of low-frequency $1/f$ noise in Josephson junctions and SQUIDs, or the study of nonequilibrium phenomena in superconductors such as quasiparticle charge imbalance.

[84]M.B. Ketchen, D.D. Awschalom, W.J. Gallagher, A.W. Kleinsasser, R.L. Sanstrom, J.R. Rozen, B. Bumble, IEEE Trans. Magn. **MAG-25**, 1212-1215 (1989).

[85]M.B, Ketchen, T. Kopley, H. Ling, Appl. Phys. Lett. **44**, 1008-1010 (1984).

[86]D.D. Awschalom, J. Warnock, IEEE Trans. Magn. **MAG-25**, 1186-1192 (1989).

[87]J. Clarke, *A superconducting galvanometer employing Josephson tunneling*, Phil. Mag. **13**, 115-127 (1966).

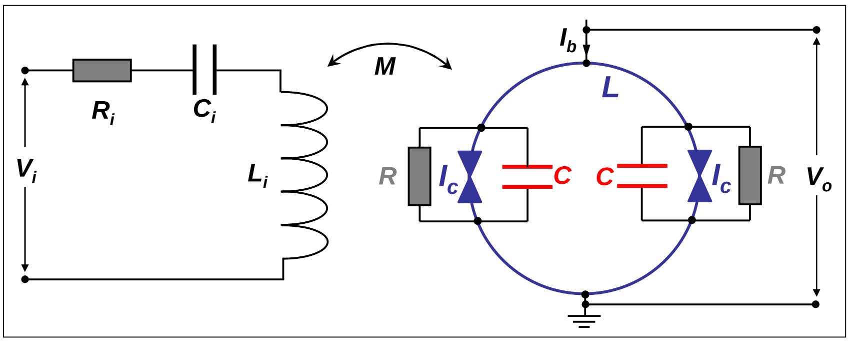

Figure 4.27: Schematic circuit diagram of a tuned radio-frequency amplifier based on a dc SQUID.

4.4.5 Radiofrequency Amplifiers

Over the last years SQUIDs have been used to develop low-noise amplifiers for frequencies up to 100 MHz.[88] As shown in Fig. 4.27 one can realize a tuned amplifier by connecting an input circuit consisting of a series connection of an input inductance L_i, an input capacitor C_i and an input resistor R_i to the SQUID. The presence of this input circuit modifies the SQUID parameters and the magnitude of the noise spectral density.[89] Furthermore, the SQUID reflects back an impedance $\omega^2 M^2/Z$ into the input circuit, where Z is the input impedance of the SQUID.[90] Fortunately, if the coupling coefficient α between the input inductance and the SQUID inductance is small enough, one can neglect the mutual influence of the SQUID and the input circuit.

For a signal frequency f generated by a source with resistance R_i the optimum noise temperature of the amplifier is given by[91]

$$T_N^{\rm opt} = \frac{\pi f}{k_B H} \left(S_V S_I - S_{VI}^2\right)^{1/2} . \tag{4.4.8}$$

Here, H is the flux-to-voltage transfer coefficient of the SQUID, S_V and S_I the voltage and current noise spectral density of the SQUID, respectively, and S_{VI} is the cross-spectral density. The latter arises from the correlations between S_V and S_I, because the asymmetric part of the current noise generates a flux noise, which in turn contributes to the total voltage noise for $H \neq 0$ (compare section 4.1.3). Simulations show that $S_I \approx 11 k_B T/R_N$ and $S_{VI} \approx 12 k_B T$ for a SQUID with $\beta_L = 1$, $\gamma = 0.05$ and $\Phi = (2n+1)\Phi_0/4$.[92]

The minimum noise temperature is actually obtained off-resonance. If one wants to operate the amplifier at the resonance frequency of the input circuit, the noise temperature is increased to

$$T_N^{\rm res} = \frac{\pi f}{k_B H} \left(S_V S_I\right)^{1/2} . \tag{4.4.9}$$

The corresponding power gain is $G \approx H/\omega$. Note that expressions (4.4.8) and (4.4.9) do not contain the Nyquist noise of the input resistor R_i which may be significant and exceeds the noise of the amplifier. **Hilbert** and **Clarke** fabricated several amplifiers and achieved $G = 18.6$ and $T_N = 1.7 \pm 0.5$ K at 93 MHz. The theoretically expected values were 17 dB and 1.1 K.

[88] C. Hilbert, J. Clarke, *dc-SQUIDs as radiofrequency amplifiers*, J. Low Temp. Phys. **61**, 263-280 (1985).
[89] C. Hilbert, J. Clarke, J. Low Temp. Phys. **61**, 237-262 (1985).
[90] J.M. Martinis, J. Clarke, J. Low Temp. Phys. **61**, 227-236 (1985).
[91] J. Clarke, *SQUIDs: Principles, Noise and Applications*, in *Superconducting Devices*, S.T. Ruggiero and D.A. Rudman, eds., Academic Press Inc., Boston (1990), pp. 51-100.
[92] C.D. Tesche, J. Clarke, J. Low Temp. Phys. **37**, 397-403 (1979).

At $T = 0$ the Nyquist noise has to be replaced by the quantum expression taking into account zero point fluctuations. It was shown by **Koch** *et al.* that in the quantum limit the noise temperature of a tuned amplifier is given by[93]

$$T_N^{\text{quantum}} = \frac{hf}{k_B \ln 2} \ . \tag{4.4.10}$$

This is the result for any quantum limited amplifier.

[93] R.H. Koch, D.J. van Harlingen, J. Clarke, Appl. Phys. Lett. **38**, 380-382 (1981).

4.5 Applications of SQUIDs

Due to their exceptional sensitivity and the fact that SQUID sensors are sensitive to all kind of signals that can be converted to a magnetic flux signal by the input antenna, SQUIDs have found widespread applications. In this section we describe a few of them.

4.5.1 Biomagnetism

Non-invasive medical investigations utilizing the detection of magnetic signals originating from the human body are termed biomagnetic methods. Over the last decades, ***biomagnetic imaging*** has been developed as a new modality for functional diagnosis providing valuable new insight into a broad variety of problems. The basic idea is that every activity of the brain is connected with neuronal ionic currents and every beat of the heart is generated by ionic depolarization currents. These currents create magnetic fields that can be measured non-invasively outside the body. By measuring the field strength and direction at many positions, a field map can be constructed that allows the calculation of the location of the source inside the body. The electrical potentials at the surface are well known signals in medical diagnosis (EEG: electroencephalography, ECG: electrocardiography). However, since the human body consists of different tissues with different electrical conductivities, it is usually very difficult to determine the location of a current source from the measurement of the potentials on the surface. In contrast, very simple volume conductor models are adequate to interpret the magnetic field distribution for the localization of sources (MEG: magnetoencephalography, MCG: magnetocardiography).[94] Over the last decades a remarkable success has been achieved in applying SQUID systems to magnetoencephalography and magnetocardiography.[95,96,97,98] These achievements in biomagnetic imaging are closely related to the high level of development of SQUID instrumentation. On the one hand, biomagnetism has been the major driving force for improvements in SQUID system development. However, on the other hand, better SQUID systems opened up new perspectives and applications and produced better results in biomagnetism.

The magnetic fields to be measured in biomagnetism are extremely small (see Fig. 4.23) and range from the 100 fT (brain) to the 10 pT regime (heart).[99] Therefore, highly sensitive SQUID magnetometers are a prerequisite for the detection of biomagnetic signals. In particular, the SQUID sensors should have very low $1/f$ noise, since the typical frequency range of biomagnetic signals is between 1 and 100 Hz. Note that the field strength of a single neuron is only about 0.1 fT and would not be sufficient to be detected. What is measured is the combined action of some 10 000 neurons.

The aim of an MCG or MEG measurement is to determine the spatio-temporal magnetic field distribution in a measurement plane just above the thorax or the head. Thus, in the ideal case, the magnetic field signals should be detected simultaneously by a set of SQUID sensors covering this plane with a spatial sampling frequency which allows all relevant features to be detected. Real SQUID systems are, of course, a compromise. In order to reduce system costs, one approach is to use single measurement

[94] M. Hämäläinen, R. Hari, R.J. Ilmoniemi, J. Knuutila, O.V. Lounasmaa, *Magnetoencephalography – theory, instrumentation and applications to noninvasive studies of the working human brain*, Rev. Mod. Phys. **65**, 413-492 (1993).

[95] C. Baumgartner, L. Deecke, G. Stroink, and S. J. Williamson, eds., *Biomagnetism: Fundamental Research and Clinical Applications*, Proc. 9th Int. Conf. Biomagnetism, in Studies in Applied Electromagnetics and Mechanics, vol. **7**, IOS Press, Amsterdam (1995).

[96] C.J. Aine, Y. Okada, G. Stroink, S. Swithenby, and C. C. Wood, eds., Biomag 96, Proc. 10th Int. Conf. Biomagnetism, vol. **1** and **2**, Springer, New York (2000).

[97] T. Yoshimoto, M. Kotani, S. Kuriki, H. Karibe, and N. Nakasato, eds., *Recent Advances in Biomagnetism*, Proc. 11th Int. Conf. Biomagnetism, Tohoku University Press, Sendai (1999).

[98] J. Nenonen, R.J. Ilmoniemi, T. Katila (eds.), Biomag 2000, Proc. 12th Int. Conf. Biomagnetism, Helsinki University of Technology, Espoo, Finland (2001).

[99] J.P. Wikswo Jr., IEEE Trans. Appl. Supercond. **5**, 74 (1995).

Figure 4.28: Multichannel SQUID systems for magnetoencephalography (left, CTF Systems Inc., Vancouver, Canada) and magnetocardiography (right, Biomagnetic Technologies, San Diego, USA)

position SQUID systems and to scan these systems over several measurement sites to carry out a measurement of the spatio-temporal magnetic field distribution. Another approach is to use a SQUID system with many SQUIDs that measure simultaneously the magnetic field signals at the sites according to the positional configuration of the SQUID sensors. Today in most cases complex multichannel SQUID systems are used consisting of a large number of channels (up to several hundred).[100,101] Fig. 4.28 shows two multichannel systems used for magnetoencephalography (left) and magnetocardiography (right). Unfortunately, the specification of multichannel SQUID systems often is confusing, since usually no distinction is made between the number of SQUIDs in a system, the number of signal output channels and the number of measurement sites. For example, a number of SQUIDs is frequently used for gradiometry or other purposes and only a subtotal of all SQUIDs is involved in the measurement itself. From the point of view of cardiology only the number of measurement sites is relevant. For example, a sophisticated single measurement position SQUID sensor for unshielded operation may well contain up to more than 10 SQUIDs, that is, the system would require more than 1 000 SQUIDs for 100 measuring sites.

The magnetic signals generated by the human brain are of the order of 100 fT and therefore much smaller than the environmental noise signals (see Fig. 4.23). Hence, today almost all multichannel SQUID systems are operated in magnetically shielded rooms consisting of several layers of μ-metal (see Fig. 4.24). Unfortunately, these shielded rooms have a typical weight of several tons and cost about EUR 500 000. There is an ongoing discussion whether or not it is possible to perform biomagnetic measurements of high quality also in an unshielded environment. Active shielding has been proposed as well as systems that carry out software corrections using several additional magnetometers and gradiometers that measure the environmental noise.[102,103] In any case gradiometer configurations have to be used for the detection of brain signals to suppress the much stronger signals generated by the heart. Today both wirewound and thin-film gradiometers are used.[104,105]

[100] J. Vrba, S.E. Robinson, Supercond. Sci. Techn. **15** , R51 (2002).

[101] V. Pizella, S. Della Penna, C. Del Gratta, G.L. Romani, Supercond. Sci. Techn. **14** , R79 (2001).

[102] H.J.M. ter Brake, N. Janssen, J. Flokstra, D. Veldhuis, and H. Rogalla, IEEE Trans. Appl. Supercond. **AS-7**, 2545 (1997); Meas. Sci. Technol. **8**, 927 (1997); Supercond. Sci. Technol. **10**, 512 (1997).

[103] B. David,O. Dössel, V. Doormann, R. Eckart, W. Hoppe, J. Krüger, H. Laudan, and G. Rabe, IEEE Trans. Appl. Supercond. **AS-7**, 3267 (1997).

[104] J. Vrba, in *SQUID Sensors: Fundamentals, Fabrication and Applications*, NATO ASI Series, H. Weinstock ed., Kluwer Academic, Dordrecht (1996), p. 117.

[105] J. Borgmann, P. David, G. Ockenfuß, R. Otto, J. Schubert, W. Zander, and A. I. Braginski, Rev. Sci. Instrum. **68**, 2730 (1997).

Signal Reconstruction

The magnetic field distribution measured by the SQUID system is caused by currents flowing in the human body. Unfortunately, it is impossible to calculate the current distribution from the measured field distribution even if we could measure the field distribution with arbitrary precision. The reason for that is the fact that the so-called inverse problem of electrodynamics has no unique solution.[106] That is, many different current distributions can create similar field patterns. Fortunately, not all of these current distributions are physiologically meaningful. Therefore, making additional model assumptions based on medical background knowledge the inverse problem can be solved. All models have in common that the current distribution is assumed to be the sum of elementary physiological sources that can be modeled as current dipoles. Current dipoles consist of short localized conductor segments and broad volume currents flowing back through the surrounding tissue closing the circuit. Both the short current path and the volume current contribute to the magnetic field. Obviously, a detailed description of the volume currents depends on the geometry and conductivity of the surrounding tissue. Often simplifying assumptions are made as e.g. a homogeneous spherical or half-space model.

By measuring the field distribution by a multichannel SQUID system the orientation and position of the current dipoles can be determined. For example, in this way the coordinates of the brain regions responsible for an epileptic attack can be determined. These regions in turn can be superimposed with a three-dimensional image of the brain obtained by magnetic resonance imaging.

Magnetocardiography

The heart signals are of the order of 100 pT and therefore by about three orders of magnitude larger than the brain signals. However, fine structures with signal amplitudes of only a few pT are clinically relevant. In MCG the goal is to determine the sources of pathological signals with high precision in three dimensions. Therefore, all three vector components of the magnetic field have to be measured. In Fig. 4.29a a common measurement configuration in MCG is illustrated. The instantaneous heart action is modeled by a current dipole associated with a magnetic field threading the sensor plane. The planar sensor loops detect B_z, the z-component of the field. Thus, for this configuration, some sensors yield positive and others negative values of the instantaneous field component B_z. From the measured distribution of B_z values a so-called field map can be derived for every instant during the heart beat. Doing so one is interpolating between the values obtained in the different measuring channels. Common representations of such maps are by iso-contour lines or by false color scaling as shown in Fig. 4.29b and c. Since such maps can be constructed for each instant during a heart beat, a video sequence of such maps can be constructed to give the medical doctor a valuable impression of the spatio-temporal dynamics of the evolution of the magnetic field associated with the heart function.

Two magnetic field map sequences (MFMS) covering a whole heart beat are shown in Fig. 4.29b and c. The sequence on the left is that of a volunteer with a healthy heart, whereas on the right the map sequence of a patient is shown who suffered from ventricular tachycardia. The differences in field distributions are considerable. It should be noted that a great variety of MFMS exists due to the biological variability. Each heart-healthy individual and each patient has its own finger print of an MFMS that may even vary in time and circumstances for a particular person. The art of interpreting these patterns is to identify the signatures in these varying patterns that are clinically relevant indications of typical pathologies.

While shielded rooms offer excellent conditions for basic biomagnetic research, unshielded operation of SQUID systems is the ultimate goal from the commercial point of view. This is in particular true for MCG applications. However, this goal is very hard to achieve and requires state-of-the-art noise suppression

[106] J. Sarvas, Phys. Med. Biol. **32**, 11 (1987).

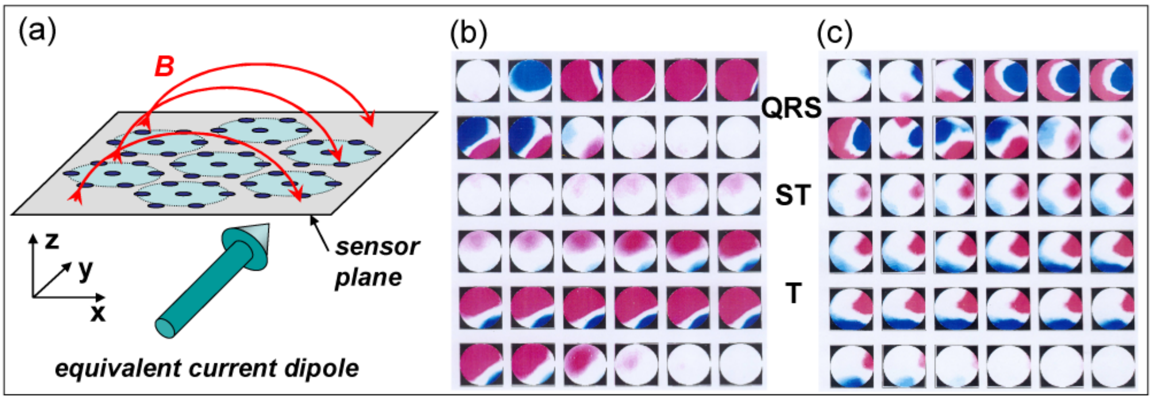

Figure 4.29: (a) Typical measurement configuration for MCG. (b) Magnetic field map sequences (false color representation) of a heart-healthy volunteer and (c) of a patient with a high risk for sudden heart death (according to H. Koch, IEEE Trans. Appl. Supercond. **AS-11** 49-59 (2001)).

techniques by sophisticated gradiometer approaches. In recent years considerable progress has been made as far as ever better noise suppression techniques are concerned, and combinations of hardware and software gradiometers produced impressive results.[107] An example is shown in Fig. 4.30 where the magnetic field distribution during the R-peak above the thorax of a healthy volunteer is shown in an arrow field representation. The field distribution was measured with a SQUID configuration consisting of 11 SQUID chips positioned at the sides of two cubes placed on top of each other.[108] Thus the vector components B_x, B_y and B_z of two planes could be approximated by composing the signals from the individual SQUIDs according to $B_x \sim (B_{x1} + B_{x2})/2$. The acquired field distribution is surprisingly smooth and simple and it is straightforward to derive the corresponding current distribution generating the measured magnetic field pattern. Improved vector magnetometer systems containing modules with an even larger number of SQUIDs allow the measurement of the magnetic field vectors in three planes at many measurement sites. Then, by exploitation of redundancies and vector analytical relations (such as curl and div), a comprehensive picture of the biomagnetic field is obtainable.

Magnetoencephalography

Magnetoencephalography (MEG) is a completely noninvasive, non-hazardous technology for functional brain mapping. It provides a spatial resolution of about 2 mm and an excellent temporal resolution on the order of 1 ms, during the localization and characterization of the electrical activity of the central nervous system by measuring the associated magnetic fields emanating from the brain. MEG measures the intercellular currents of the neurons in the brain giving a direct information on the spontaneous or stimulated brain activity. Since MEG takes its measurements directly from the activity of the neurons themselves, its temporal resolution is comparable with that of intracranial electrodes. Since the first MCG-SQUID experiments in 1970,[109] a large number of different MEG-system solutions have been introduced, which we will not address here. MEG has particularly profitted from advances in computing algorithms and SQUID sensor hardware. Due to the small signals SQUID sensors with optimum field resolution are required. Furthermore, the suppression of noise signals is an important aspect in MEG.

[107] J. Vrba, *SQUID gradiometers in real environments*, in *SQUID Sensors: Fundamentals, Fabrication and Applications*, H. Weinstock, ed., NATO ASI Series E: Applied Sciences, Vol. 329, pp. 117-178, Kluwer Academic Publishers, Dordrecht (1996).

[108] M. Burghoff, H. Schleyerbach, D. Drung, L. Trahms, and H. Koch, *A vector magnetometer module for biomagnetic application*, IEEE Trans. Appl. Supercond. **AS-9**, 4069-4072 (1999).

[109] D. Cohen, E. A. Edelsack, and J.E. Zimmerman, *Magnetocardiograms taken inside a shielded room with a superconducting point-contact magnetometer*, Appl. Phys. Lett. **19**, 278-280 (1970).

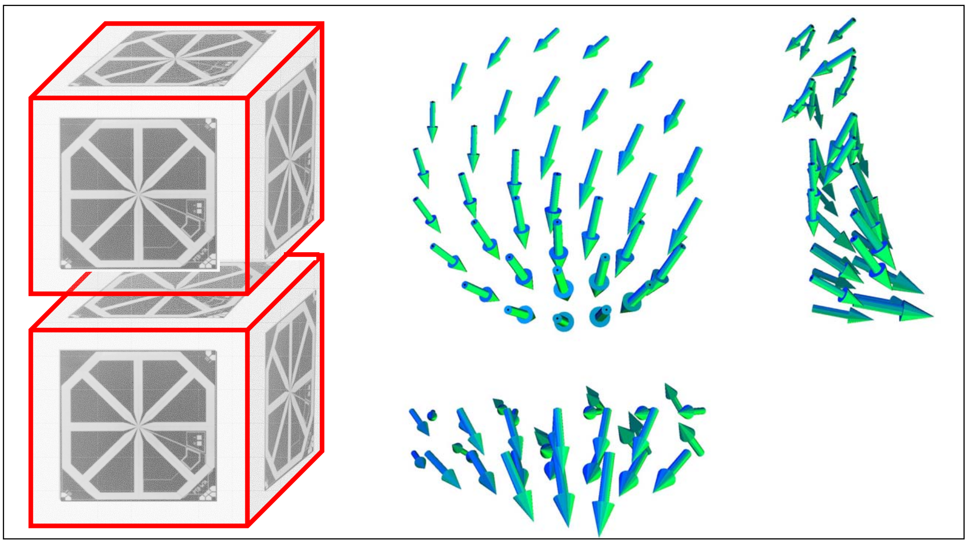

Figure 4.30: Magnetic vector field during the R peak measured sequentially at 37 positions with an 11 SQUID chip configuration as shown on the left. Displayed are the top view and two side views of an arrow representation of the field distribution (courtesy of PTB Berlin).

The information provided by MEG is entirely different from that provided by Computer Tomography (CT) or Magnetic Resonance Imaging (MRI). Whereas these techniques provide structural/anatomical information, MEG provides functional information. That is, MEG is a functional imaging technique complementary to the anatomical imaging methods MRI and CT. Of course, the two modalities can be combined into a composite image containing information on function *and* anatomy. It is obvious that the combination of MEG and MRI techniques has considerable clinical potential.

Of course, SQUID based MEG has to compete with various other functional imaging techniques such as Positron Emission Tomography (PET) and functional MRI (fMRI), which are weakly invasive and measure signals caused by changes of blood flow. At present, the time resolution of MEG (about 1 ms) is far superior to that of the other techniques, while the spatial resolution is similar. In general, MEG's strengths complement those of other brain activity measurement techniques such as electroencephalography (EEG), PET and fMRI. Here particular advantages of MEG are that the measured biosignals are not distorted by the body as in EEG (unless ferromagnetic implants are present) and that it is completely non-invasive, as opposed to PET and possibly MRI/fMRI. The clinical uses of MEG are in detecting and localizing epileptiform spiking activity in patients with epilepsy, and in localizing eloquent cortex for surgical planning in patients with brain tumors or intractable epilepsy. In research, MEG's primary use is the measurement of time courses of activity, which cannot be measured using fMRI.

4.5.2 Nondestructive Evaluation

An interesting field of application of SQUID sensors is ***nondestructive evaluation*** (NDE). NDE is the noninvasive identification of structural or material flaws in a specimen. Examples are the imaging of surface and subsurface cracks or pits due to corrosion or fatigue in aging aircraft and reinforcing rods in concrete structures.[110,111] Of course, there are several competing methods for NDE such as acoustic, thermal, and electromagnetic techniques. However, these methods are often not entirely adequate for detecting flaws at an early enough stage, usually because of a lack of spatial or depth resolution. Since

[110] J.P. Wikswo Jr., IEEE Trans. Appl. Supercond. **AS-5**, 74 (1995).

[111] G.B. Donaldson, A. Cochran, R.M. Bowman, *More SQUID Applications*, in *The New Superconducting Electronics*, H. Weinstock, R.W. Ralston (eds.), Kluwer Academic Publishers, Deventer (1993), pp. 181-220.

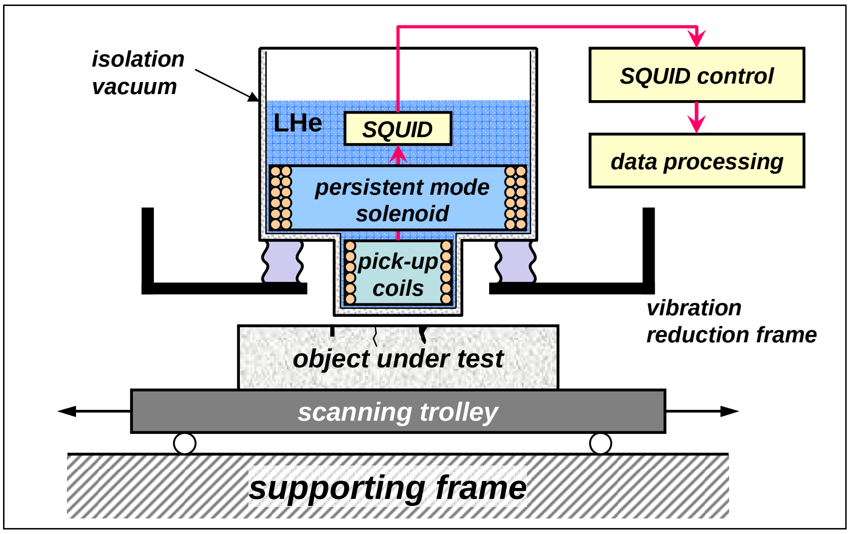

Figure 4.31: Typical experimental set-up for SQUID based NDE. For high-T_c SQUIDs liquid nitrogen or cryocoolers instead of liquid helium is used for cooling. The sample motion is controlled by a motorized motion control and linear encoders.

the object to be studied usually is at room temperature and an important parameter is the lateral spatial resolution, which is of the order of the distance between the sensor and the object under study, the distance between the inner cold wall and the outer warm wall of the SQUID measuring systems must be as small as possible. Therefore, SQUIDs based on high temperature superconductors operated at 77 K are advantageous for NDE applications. In this case the required dewars or cryocoolers are simpler and more compact.

Fig. 4.31 shows a typical experimental set-up for SQUID based NDE. A magnet is used to magnetize the object under study, which is placed below the pick-up coil of a SQUID sensor. Cracks in the plate or variations in the magnetic properties will disturb the magnetic field pattern and the resulting flux change is detected by the SQUID sensor. The advantage of the SQUID sensor is that the flux changes can be measured with unchanged sensitivity in rather high background fields. This method of detection is also called remote magnetometry.

An important application of SQUIDs in NDE is the detection of subsurface damage in metallic structures such as aircraft parts by eddy current techniques. Here, an alternating magnetic field produced by a drive coil is applied and the fields generated by the induced eddy currents in the structure are lock-in detected. The eddy currents are diverted by structural flaws resulting in distortions of the magnetic field. Since the eddy currents flow over a skin depth, which is inversely proportional to the square root of the frequency, deep defects require correspondingly low frequencies. Here, the flat frequency response of SQUIDs is a distinct advantage over the response of currently used coil systems, which fall off with decreasing frequency. Demonstrations of eddy-current NDE using high-Tc SQUIDs have been reported by a number of groups.[112,113,114,115,116] One should note however that the better sensitivity of SQUID systems has to be retained in a mobile unit capable of operating in the magnetically unfriendly environment such as an

[112]Y. Tavrin, H.-J. Krause, W. Wolf, V. Glyantsev, J. Schubert, W. Zander, and H. Bousack, Cryogenics **36**, 83 (1995).
[113]M. Mück, M., M. v. Kreutzbruck, U. Baby, J. Tröll, and C. Heiden, Physica C **282-287**, 407 (1997).
[114]M. v. Kreutzbruck, J. Tröll, M. Mück, C. Heiden, and Y. Zhang, IEEE Trans. Appl. Supercond. **AS-7**, 3279 (1997).
[115]R. Hohmann, H.-J. Krause, H. Soltner, Y. Zhang, C. A. Copetti, H. Bousack, and A. I. Braginski, IEEE Trans. Appl. Supercond. **AS-7**, 2860 (1997).
[116]H.-J. Krause, Y. Zhang, R. Hohmann, M. Grüneklee, M. I. Faley, D. Lomparski, M. Maus, H. Bousack, and A. I. Braginski, in *Proceedings of the EUCAS'97*, Ueldhoven Institute of Physics Conference Series No. 158, H. Rogalla and D. H. A. Blank eds., Institute of Physics, Philadelphia (1997), p. 775.

aircraft maintenance hangar or a factory.

NDE with SQUIDs can also be used for the detection of magnetic fields generated by specimens containing magnetized components.[117] Furthermore, by scanning samples of steel one can explore the correlation between mechanical stress and magnetic-field distribution. This represents a unique probe of the mechanical or thermal stress to which a sample has been subjected. For example, it was shown that SQUID sensors based on second-order electronic gradiometers can be used to detect ferrous inclusions in the disks of turbine engine rotors.[118] In an other application a dc SQUID magnetometer was used to detect fine magnetic particles in a rapidly moving copper wire. The nitrogen-cooled SQUID was surrounded by a magnetic shield and the wire was pulled through holes in the shield about 15 mm below the SQUID sensor at speeds of 10 to 500 m/min. Iron particles as small as 50 μm in diameter could be detected. The goal of this technique is to locate impurities that make the wire brittle, causing it to break. Fortunately, most NDE applications do not require the highest sensitivity of SQUID sensors, since the Nyquist noise generated by the sample can be of the order of 1 pT/$\sqrt{\mathrm{Hz}}$. However, this noise level is still much lower than that of coil systems conventionally used for eddy current NDE. Thus, NDE applications based in particular on high-T_c SQUIDs are very promising.

4.5.3 SQUID Microscopy

Scanning SQUID microscopy (SSM) is a modern technique capable of imaging the magnetic field distribution in close proximity across the surface of a sample under investigation with high sensitivity and modest spatial resolution. It is based on a thin-film SQUID sensor. Initially, scanning SQUID microscopes were based on low-T_c dc-SQUIDs and have been used to image static magnetic fields with a combination of high field and spatial resolution.[119,120] Shortly afterwards, high-T_c SQUID microscopes have been developed, in which the sample could be either at 77 K or at room temperature.[121,122,123,124] Most often, the sample is moved over the SQUID in a two-dimensional scanning process and the magnetic signal is plotted versus the coordinate to produce an image. The frequency at which the image is obtained ranges from near zero, where simply the static magnetic field produced by the sample is measured, to beyond 1 GHz. Today SQUID microscopes with cold samples have a spatial resolution of about 5 μm, while those with room temperature samples have a resolution ranging between 30 and 50 μm. A recent innovation has dramatically improved the spatial resolution for cold samples, albeit at the price of reduced magnetic field sensitivity. A soft magnetic tip is used to focus the flux from the sample into the SQUID resulting in a spatial resolution of the order of 0.1 μm.[125]

Fig. 4.32 shows a SQUID microscope, in which the sample is kept at room temperature. The SQUID is mounted in vacuum at the upper end of a sapphire rod (cold finger), the lower end of which is cooled by liquid nitrogen. Superinsulation surrounding the rod ensures that the temperature gradient along the rod is negligible. The SQUID is separated from the room temperature part and atmospheric pressure by a thin window, which may be either a 75 μm thick sapphire disk or a 3 μm thick Si_xN_y window fabricated

---

[117] G.B. Donaldson, S. Evanson, M. Otaka, K. Hasegawa, T. Shimizu, and K. Takaku, Br. J. Non-Destr. Test. **32**, 238 (1990).

[118] Y. Tavrin, M. Siegel, and J. Hinken, 1999, IEEE Trans. Appl. Supercond. **AS-9**, 3809 (1999).

[119] A. Mathai, D. Song, Y. Gim, and F. C. Wellstood, IEEE Trans. Appl. Supercond. **AS-3**, 2609 (1993).

[120] C.C. Tsuei, J. R. Kirtley, C. C. Chi, L. S. Yu-Jahnes, A. Gupta, T. Shaw, J. Z. Sun, and M. B. Ketchen, Phys. Rev. Lett. **73**, 593 (1994).

[121] R.C. Black, A. Mathai, F. C. Wellstood, E. Dantsker, A. H. Miklich, D. T. Nemeth, J. J. Kingston, and J. Clarke, Appl. Phys. Lett. **62**, 2128 (1993).

[122] R.C. Black,F. C. Wellstood, E. Dantsker, A. H. Miklich, D. Kölle, F. Ludwig, and J. Clarke, IEEE Trans. Appl. Supercond. **AS-5**, 2137 (1995).

[123] T.S. Lee, E. Dantsker, and J. Clarke, Rev. Sci. Instrum. **67**, 4208 (1996).

[124] T.S. Lee, Y. R. Chemla, E. Dantsker, and J. Clarke, IEEE Trans. Appl. Supercond. **AS-7**, 3147 (1997).

[125] P. Pitzius, V. Dworak, and U. Hartmann, in *Extended Abstracts of the 6th International Superconductive Electronics Conference (ISEC'97)*, H. Koch and S. Knappe eds., Physikalisch-Technische Bundesanstalt, Berlin, Vol. 3, (1997), p. 395.

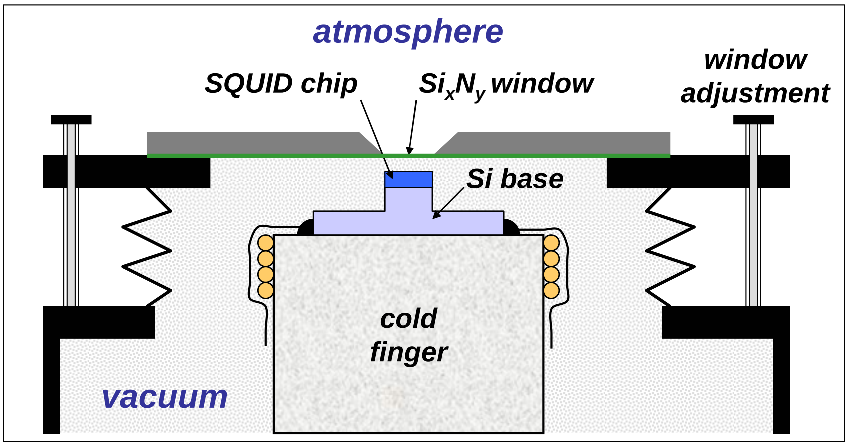

Figure 4.32: Cross-sectional view of a scanning SQUID microscope. The distance between the SQUID sensor and the Si_xN_y window can be adjusted by adjustment screws.

on a Si chip. In the first case, the SQUID-to-sample separation is typically 150 μm, whereas in the latter, the separation can be as low as 15 μm. Note that the smaller the SQUID-to-sample distance the better the spatial resolution. The entire system is surrounded by a μ-metal shield to exclude spurious magnetic field fluctuations.

For low-frequency operation (typically less than 1 kHz) the SQUID is operated in the flux lock loop. Here, a typical application is the study of the magnetic properties of superconducting thin-film structures as well as the diagnostics of superconducting integrated circuits or highly sensitive bolometers. In such application the sample is usually at the same temperature as the SQUID sensor. Two typical examples are shown in Fig. 4.33. Furthermore, SSM can be applied to study magnetic properties of the ultra-thin magnetic films. The distribution of stray magnetic fields produced by the remnant magnetization or the induced magnetization of the film can be visualized. The domain structures, the orientation of the magnetic moment and the value of the magnetization can be determined. Moreover, SSM has the potential to image the magnitude of a magnetic field normal component over the surface of magnetic recording media. It also can be applied to the analysis of chips or wafers in microelectronics[126,127] or the study of magnetically active bacteria.[128] For higher-frequency operation (typically 1 kHz to 1 MHz) the SQUID is operated open loop and a drive coil is used to apply a sinusoidal magnetic field to induce eddy currents in the sample and modulate the flux in the SQUID.[129] The magnetic response of the sample is determined by measuring the amplitude and phase of the output from the SQUID: the out-of-phase component corresponds to the eddy current in the sample. The imaging frequency has further been extended from 1 MHz to 1 GHz by applying a rf-field to the sample, which, in turn, couples an rf-flux into the SQUID.[130]

There are many other techniques for imaging magnetic fields at surfaces: decoration techniques,[131] magneto-optical imaging,[132] magnetic force microscopy,[133] scanning Hall probe microscopy,[134] scan-

[126] S. Chatraphorn, E.F. Fleet, F.C. Wellstodd, J. Appl. Phys. Lett. **92**, 4731 (2002).
[127] J. Beyer, H. Matz, D. Drung, Th. Schurig, Appl. Phys. Lett. **74**, 2863 (1999).
[128] T.S. Lee, Y.R. Chemla, E. Dantsker, J. Clarke, IEEE Trans. Appl. Supercond. **AS-7**, 3147 (1997).
[129] R.C. Black, F. C. Wellstood, E. Dantsker, A. H. Miklich, J. J. Kingston, D. T. Nemeth, and J. Clarke, Appl. Phys. Lett. **64**, 1 (1994).
[130] R.C. Black, F. C. Wellstood, E. Dantsker, A. H. Miklich, D. T. Nemeth, D. Koelle, F. Ludwig, and J. Clarke, Appl. Phys. Lett. **66**, 1267 (1995).
[131] D. J. Bishop, P. L. Gammel, D. A. Huse, and C. A. Murray, Science **255**, 165 (1992).
[132] S. Gotoh and N. Koshizuka, Phys. C **176**, 300 (1991).
[133] D. Rugar, H. J. Mamin, P. Guethner, S. E. Lambert, J. E. Stern, I. McFadyen, and T. Yogi, J. Appl. Phys. **68**, 1169 (1990).
[134] A. M. Chang, H. D. Hallen, L. Harriott, H. F. Hess, H. L. Kao, J. Kwo, R. E. Miller, R. Wolfe, and J. van der Ziel, Appl.

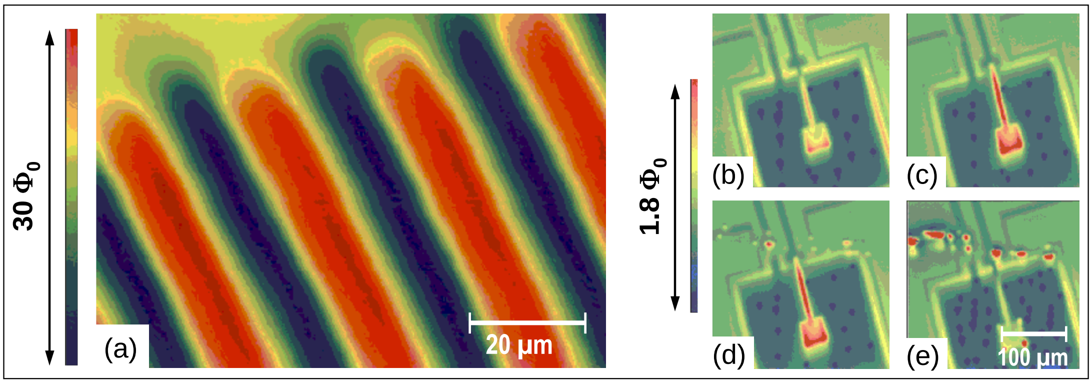

Figure 4.33: (a) Scanning SQUID microscopy image showing the magnetic field distribution above the alignment track on a 5.25 in floppy disk. The color code gives the flux range threading the 10 μm diameter SQUID loop oriented normal to the disk surface. (b) to (e) Images of the normal component of the field above a high-T_c YBCO washer SQUID with a scratch running from the upper left to the middle right. (a) Washer cooled in low field, then (b) cycled to 0.6 G, and (c) to 2.2 G at 4.2 K, and finally (d) cycled to 2.4 G at 77 K. Flux traps first along the scratch, and then at inside corners of the SQUID (according to J. R. Kirtley, M. B. Ketchen, C. C. Tsuei, J. Z. Sun, W. J. Gallagher, Lock See Yu-Jahnes, A. Gupta, K. G. Stawiasz, S. J. Wind, IBM J. Res. Develop. **39**, 655 (1995)).

ning electron microscopy with polarization analysis (SEMPA),[135] and electron holography.[136] Each of these techniques has its own advantages: For example, the magneto-optical techniques are relatively simple and provide the possibility for time-resolved studies, and the electron microscope techniques have very good spatial resolution.[137] The advantage of the scanning SQUID microscope is its very high sensitivity. Roughly speaking, the scanning SQUID microscope is orders of magnitude more sensitive to magnetic fields than the other techniques. In addition, it gives an easily calibrated absolute value for the local magnetic fields. A disadvantage of SSM is its relatively poor spatial resolution. Whereas for SSM a resolution of only 5 μm has been demonstrated, SEMPA, for example, has a spatial resolution of 30-50 nm. Nevertheless, there are many possible applications of SSM, which do not require submicron spatial resolution.

4.5.4 Gravity Wave Antennas and Gravity Gradiometers

SQUID systems are used in a number of experiments designed for measuring gravitational forces. Important topics in this area are inertial navigation, general relativity verification, the analysis of deviations from the $1/r^2$ law and the detection of gravitational waves. Gravitational waves are emitted by bodies when the mass distribution varies non-spherically (e.g. collapsing star or rotating double star). To detect gravitational waves one can look for the expansion and contraction oscillations caused by the gravitational wave. A simple version of such a setup is called a ***Weber bar*** – a large, solid piece of metal with electronics attached to detect any vibrations. [138,139] However, the expected length change $\Delta\ell/\ell$ is extremely small and typically below 10^{-19}. Therefore, highly sensitive detectors are required having a resolution down to 10^{-21}.

A typical experimental setup is shown in Fig. 4.34. The vibrations of the large bar are amplified by a

Phys. Lett. **61**, 1974 (1992).

[135] M. R. Scheinfein, J. Unguris, M. H. Kelley, D. T. Pierce, and R. J. Celotta, Rev. Sci. Instrum. **61**, 2501 (1990).

[136] K. Harada, T. Matsuda, J. Bonevich, M. Igarashi, S. Kondo, G. Pozzi, U. Kawabe, and A. Tonomura, Nature **360**, 51 (1992).

[137] L. N. Vu and D. J. Van Harlingen, IEEE Trans. Appl. Supercond. **AS-3**, 1918 (1993).

[138] S.L. Shapiro, R.F. Stark, S.J. Teukolsky, Am. Sci. **73**, 248-257 (1985).

[139] J.C. Price, R.C. Taber, Science **237**, 150-157 (1987).

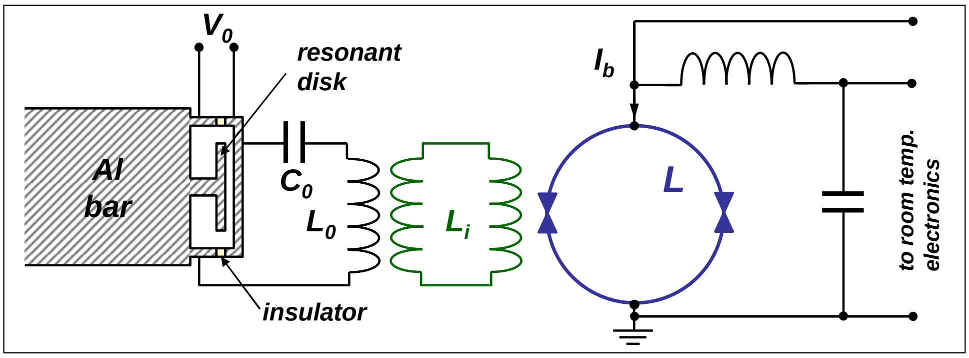

Figure 4.34: Typical setup for the detection of gravity waves. An Al-bar of several tons has a resonant transducer connected to the end of the bar. The small displacement of the disk is detected by a SQUID sensor via a capacitive coupling of the disk-to-flux transformer circuit.

resonant mass transducer and the displacement induces a current in a flux-transformer which is coupled to the input coil of a SQUID sensor. The antenna has to be cooled down to the mK-regime to reduce the mechanical noise and it further needs a very high quality factor. The resolution is then determined only by the bar's zero point motion. Since the typical resonance frequencies range in the 1 kHz regime one has to cool down below $\hbar\omega_{\rm ant}/k_B \simeq 50\,$nK. However, one can make the effective noise temperature of the antenna much higher by increasing the bar's resonant quality factor Q. If a gravitational signal in the form of a pulse of length τ interacts with the antenna that has a decay time $Q/\omega_{\rm ant}$, the effective noise temperature is given by $T_{\rm eff} = T\frac{\tau}{Q/\omega_{\rm ant}}$, that is by the antenna temperature multiplied by the ratio of the signal pulse length and the antenna decay time. To achieve the quantum limit, where the bar energy $\hbar\omega_{\rm ant}$ is larger than the effective thermal energy $k_B T_{\rm eff}$, one has to cool down below $T = Q\hbar/k_B\tau$. For $Q = 2\times 10^6$ and $\tau = 1$ ms this is roughly 20 mK what is achievable with standard dilution refrigerators. Of course, a quantum limited sensor is required for the detection of the motion of the quantum-limited antenna. That is, the sensitivity of the SQUID has to approach the quantum limit. At present, a number of gravity wave antennas with $\Delta\ell/\ell$ sensitivities in the 10^{-18} regime have been fabricated and are in use since a few years. However, until now no detection of gravity waves has been reported. There are plans to build spherical detectors with a diameter of 3 m and an sensitivity of about 10^{-21}.

Gravity gradiometers are in principle also displacement sensors.[140,141] A typical configuration is shown in Fig. 4.35. The gradiometer consists of two superconducting test masses, which are fixed by springs so that they can move along their common axis. A single layer wire-wound spiral coil is attached to the surface of one of the masses so that the surface of the wire is very close to the opposing surface of the other mass. The induction of the coil depends on the separation of the two test masses, which in turn depends on the gravity gradient. The coil is connected to a second coil which is coupled to the input coil of a SQUID sensor via a superconducting flux transformer. The gravity gradient is a tensor and is expressed in Eötvös (1 Eötvös = 10^{-9}s^{-2}). Until today sensitivities of a few Eötvös have been achieved. Gravity gradiometers can be used for mapping the earth's gravity gradient and have the potential for testing the inverse square law. A further application is inertial navigation. Several space-born instruments with sensitivities of a few to 0.001 Eötvös down to the mHz-regime have been proposed.

[140]H.J. Paik, in *SQUID Applications to Geophysics*, H. Weinstock and W.C. Overton (eds.), Soc. of Exploration Geophysicists, Tulsa, Oklahoma (1981), pp. 3-12.
[141]E.A. Mapoles, in *SQUID Applications to Geophysics*, H. Weinstock and W.C. Overton (eds.), Soc. of Exploration Geophysicists, Tulsa, Oklahoma (1981), pp. 153-157.

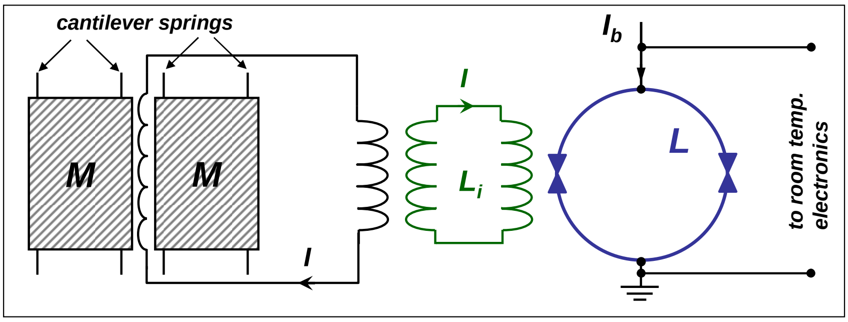

Figure 4.35: Gravity gradiometer consisting of two test masses M on either side of a planar spiral coil.

4.5.5 Geophysics

SQUID systems play an important role in determining the magnetic properties of the earth. This concerns both the characterization of specific earth samples (rock magnetometry) and the mapping of the earth magnetic field as well as its electromagnetic impedance. Particularly, high-T_c SQUID magnetometers are promising for geophysical surveying such as for example, magnetotellurics, controlled-source electromagnetics, and cross-borehole sounding.[142] In magnetotellurics, the fluctuating horizontal components of the electric and magnetic fields at the earth's surface are measured simultaneously. These fluctuating fields originate in the magnetosphere and ionosphere. From these frequency-dependent fields the impedance tensor of the ground can be calculated allowing to estimate the spatial variation of the resistivity of the ground. The interesting frequency range is about 10^{-3} to 10^2Hz corresponding to a skin depth between about 50 km and 150 m (assuming a resistivity of 10 Ωm). An important problem is the elimination of local noise sources. This can be achieved by cross-correlating the fluctuating fields with those measured by a remote (several km away) reference magnetometer. Applications of magnetotellurics include surveying for oil and gas, mineral and geothermal sources, and locating subsurface fault lines.

Currently, magnetic measurements in geophysics are mostly made with induction coils. However, the availability of high-T_c based liquid nitrogen-cooled magnetometers has renewed interest in the use of SQUID sensors. Below about 1 Hz, the spectral density of the noise in coils increases as $1/f^3$, whereas that of SQUIDs increases only as 1/f, giving the latter magnetometer a substantial advantage at low frequencies. Furthermore, coils for use below 1 Hz can be as long as 1.5 m, and the deployment of three such coils orthogonally, buried in the ground for stability, is a tedious undertaking. Obviously, a three-axis high-T_c magnetometer in a compact dewar with a long hold time becomes competitive.[143,144] The sensitivity required for magnetotellurics is about 20-30 fT/$\sqrt{\text{Hz}}$ in the white noise regime and a 1/f knee of 1 Hz.

[142] J. Clarke, T. D. Gamble, W. M. Goubau, R. H. Koch, and R. F. Miracky, Geophys. Pros. **31**, 149 (1983).
[143] D. Drung, T. Radic, H. Matz, H. Koch, S. Knappe, S. Menkel, and H. Burkhardt, IEEE Trans. Appl. Supercond. **AS-7**, 3283 (1997).
[144] E. Dantsker, D. Kölle, A. H. Miklich, D. T. Nemeth, F. Ludwig, J. Clarke, J. T. Longo, and V. Vinetskiy, Rev. Sci. Instrum. **65**, 3809 (1994).

Summary

dc-SQUID:

- A dc-SQUID is formed by a superconducting loop of inductance L intersected by two Josephson junctions with critical currents I_c.
- For negligible screening parameter $\beta_L = 2LI_c/\Phi_0 \ll 1$, the magnetic flux $\Phi = \Phi_{\rm ext} + LI_{\rm cir}$ threading the SQUID loop is about equal to the external flux, $\Phi \simeq \Phi_{\rm ext}$, and the maximum supercurrent of the SQUID varies as

$$I_s^m = 2I_c \left| \cos\left(\pi \frac{\Phi_{\rm ext}}{\Phi_0}\right) \right| .$$

- For large screening parameter $\beta_L = 2LI_c/\Phi_0 \gg 1$, the magnetic flux $\Phi = \Phi_{\rm ext} + LI_{\rm cir}$ threading the SQUID loop is about equal to $\Phi \simeq n\Phi_0$, and the maximum supercurrent of the SQUID varies as

$$I_s^m = 2I_c - \frac{2\Phi_{\rm ext}}{L} = 2I_c \left(1 - \frac{2\Phi_{\rm ext}}{\Phi_0}\frac{1}{\beta_L}\right) .$$

- For intermediate screening the $I_s^m(\Phi_{\rm ext})$ dependence has to be determined self-consistently from the $\Phi(\Phi_{\rm ext})$ and $I_s^m(\Phi)$ dependences.
- For negligible screening ($\beta_L \ll 1$) and strong damping ($\beta_C \ll 1$), the IVC of the dc-SQUID is given by

$$\langle V(t) \rangle = I_c R_N \sqrt{\left(\frac{I}{2I_c}\right)^2 - \left[\cos\left(\pi \frac{\Phi_{\rm ext}}{\Phi_0}\right)\right]^2} .$$

- The mechanical analogue of the dc-SQUID are two pendula attached to a twistable rubber bar. For $\beta_L \ll 1$, the rubber bar is rigid, for $\beta_L \gg 1$ the rubber bar is soft. The relative angle of the pendula is determined by the applied magnetic flux: $\varphi_1 - \varphi_2 = 2\pi\Phi_{\rm ext}/\Phi_0$.
- The performance of the dc-SQUID is determined by the flux-to-voltage transfer function

$$H \equiv \left| \left(\frac{\partial V}{\partial \Phi_{\rm ext}}\right)_{I=const} \right|$$

  and the equivalent flux noise or noise energy

$$S_\Phi(f) = \frac{S_V(f)}{H^2} \qquad \varepsilon(f) = \frac{S_\Phi(f)}{2L} = \frac{S_V(f)}{2LH^2} .$$

  The noise energy sets the energy resolution of the dc-SQUID, which should be as small as possible for practical applications.
- For optimum operation parameters ($\beta_L \simeq 1$, $\beta_C \simeq 1$) the noise energy of the dc-SQUID is given by

$$\varepsilon(f) \simeq 16 k_B T \sqrt{\frac{LC}{\beta_C}} \simeq \frac{16\sqrt{\pi} k_B T}{\omega_p} .$$

  Best dc-SQUIDs have a noise energy of only a few $\hbar$.
- Since the $V(\Phi_{\rm ext})$ dependence of dc-SQUIDs is nonlinear and periodic, the SQUID usually is operated in a flux-locked-loop, acting as a null detector.

RF-SQUID:

- A rf-SQUID is formed by a superconducting loop of inductance L intersected by a single Josephson junction with critical current I_c.
- The variation of the flux Φ threading the SQUID loop as a function of the applied flux $\Phi_{\rm ext}$ is given by

$$\frac{\Phi}{\Phi_0} = \frac{\Phi_{\rm ext}}{\Phi_0} - \frac{\beta_{L,\rm rf}}{2\pi}\sin\left(2\pi\frac{\Phi}{\Phi_0}\right) .$$

- The rf-SQUID is operated by inductively coupling it to a resonant tank circuit and measuring the voltage V_T of the tank circuit (with inductance L_T, resonance frequency $\omega_{\rm rf}$, quality factor Q) as a function of the external flux $\Phi_{\rm ext}$.
- The performance of the rf-SQUID is determined by the flux-to-voltage transfer function

$$H \equiv \left|\left(\frac{\partial V_T}{\partial \Phi_{\rm ext}}\right)_{I_{\rm rf}=const}\right| \simeq \frac{\omega_{\rm rf} L_T}{M}$$

and the equivalent flux noise or noise energy

$$\begin{aligned} S_\Phi &\approx \frac{(LI_c)^2}{\omega_{\rm rf}}\left(\frac{2\pi k_B T}{I_c\Phi_0}\right)^{4/3} \\ \varepsilon &\approx \left(\frac{\pi\eta^2\Phi_0^2}{2L} + 2\pi\eta k_B T_{\rm amp}^{\rm eff}\right)\frac{1}{\omega_{\rm rf}} . \end{aligned}$$

In order to make the noise energy small one has to increase the tank frequency $\omega_{\rm rf}$. Best rf-SQUIDs have a noise energy of the order of $100\hbar$.

- Since the $V_T(\Phi_{\rm ext})$ dependence of rf-SQUIDs is nonlinear and periodic, the SQUID is usually operated in a flux-locked-loop, acting as a null detector.

SQUID Based Instruments:

- SQUID based instruments usually consist of an antenna transferring an input signal into a magnetic flux threading the SQUID loop, the autonomous SQUID acting as a flux-to-voltage converter, and the read out electronics.
- Depending on the antenna, SQUIDs can be used as magnetometers, gradiometers of different order, susceptometers, voltmeters, ammeters, or rf-amplifiers.
- The magnetic field resolution of best SQUID magnetometers are of the order of a few fT/$\sqrt{\rm Hz}$ at a frequency of 1 Hz.
- First and higher order gradiometers are used for suppression of perturbing magnetic field fluctuations caused by the environment.

Applications of SQUIDs:

- In medical technology important applications of SQUIDs are magnetocardiography and magnetoencephalography. Multichannel SQUID systems are used to measure the magnetic field distribution due to currents flowing inside the body.
- SQUID sensors can be used for nondestructive evaluation of materials, in particular for the detection of structural or material flaws deep inside of a specimen.
- SQUID microscopy allows the imaging of the distribution of weak magnetic fields in various materials and devices such as superconducting and magnetic films and electronic circuits with a spatial resolution of a few μm.
- Further fields of application of SQUID systems are gravity wave detection and geophysics.